

AEDC-TR-80-26

c.5



Diagnostic Methods for Particle Property Measurements in Solid Rocket Motor Plumes

W. M. Farmer, K.E. Harwell, and R.H. Kohl
The University of Tennessee Space Institute
Tullahoma, Tennessee 37388

May 1981

Final Report for Period September 1978 – June 1979

Approved for public release; distribution unlimited.

Property of U. S. Air Force
AEDC LIBRARY
F40600-81-C-0004

**ARNOLD ENGINEERING DEVELOPMENT CENTER
ARNOLD AIR FORCE STATION, TENNESSEE
AIR FORCE SYSTEMS COMMAND
UNITED STATES AIR FORCE**

NOTICES

When U. S. Government drawings, specifications, or other data are used for any purpose other than a definitely related Government procurement operation, the Government thereby incurs no responsibility nor any obligation whatsoever, and the fact that the Government may have formulated, furnished, or in any way supplied the said drawings, specifications, or other data, is not to be regarded by implication or otherwise, or in any manner licensing the holder or any other person or corporation, or conveying any rights or permission to manufacture, use, or sell any patented invention that may in any way be related thereto.

Qualified users may obtain copies of this report from the Defense Technical Information Center.

References to named commercial products in this report are not to be considered in any sense as an endorsement of the product by the United States Air Force or the Government.

This final report was submitted by The University of Tennessee Space Institute under contract F40600-78-C-004, with the Arnold Engineering Development Center, Air Force Systems Command, Arnold Air Force Station, Tennessee. Dr. Herman E. Scott, DOT, was the Air Force Project Manager.

This report has been reviewed by the Office of Public Affairs (PA) and is releasable to the National Technical Information Service (NTIS). At NTIS, it will be available to the general public, including foreign nations.

APPROVAL STATEMENT

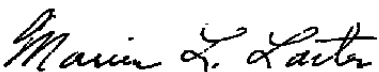
This report has been reviewed and approved.



HERMAN E. SCOTT
Project Manager
Directorate of Technology

Approved for publication:

FOR THE COMMANDER



MARION L. LASTER
Director of Technology
Deputy for Operations

UNCLASSIFIED

UNCLASSIFIED

UNCLASSIFIED

20. ABSTRACT (Continued)

Schlieren correlation, and the radiating particle velocimeter were examined and recommended for measurement of particle size, mass density, and particle temperature. An ultraviolet forward Mie scattering computer code was used to examine ultraviolet scattering patterns from particles.

UNCLASSIFIED

PREFACE

The work reported herein was conducted by The University of Tennessee Space Institute for the U.S. Air Force, Arnold Engineering Development Center, Arnold Air Force Station, Tennessee 37389 under contract F40600-78-C-0004. Dr. Herman E. Scott, DOT, was the technical representative for this project. The reproducibles used in the reproduction of this report were supplied by the authors.

CONTENTS

<u>Section</u>	<u>Page</u>
PART I ANALYSIS OF OPTICAL INSTRUMENTATION FOR PARTICLE PROPERTY MEASUREMENTS IN SOLID ROCKET MOTOR PLUMES	
1.0 INTRODUCTION.....	1
2.0 EXECUTIVE SUMMARY.....	3
2.1 CONCLUSION SUMMARY.....	4
2.1.1 Fringe Type Laser Velocimeter.....	4
2.1.2 Transit Time Laser Velocimeters.....	7
2.1.3 Local Oscillator Velocimeters.....	8
2.1.4 Spatial Distribution of Particle Number Density.....	9
2.1.5 Measurement of Number Density With A Fringe Type Velocimeter.....	10
2.1.6 Optical Instrumentation Review.....	11
2.2 ASSUMPTION SUMMARY.....	13
2.3 RECOMMENDATIONS.....	14
3.0 ANALYSIS OF LV SYSTEM PERFORMANCE IN SRM PLUMES.....	15
3.1 PARTICLE SIZES DETECTABLE IN SRM PLUMES.....	15
3.1.1 Scatter Cross-Section Required for Single Particle Measurements.....	16
3.1.2 Minimum Scatter Cross-Section for Fringe LV's.....	25
3.1.3 Minimum Scatter Cross-Section for Transit LV's and Focused Beam Particle Size Analyzers.....	27
3.1.4 Comparison of Transit and Fringe LV System Performance in SRM Plumes.....	28

<u>Section</u>	<u>Page</u>
3.1.5 Minimum Scatter Cross-Section for PSI System.....	29
3.1.6 Scatter Cross-Sections for Local Oscillator LV Systems.....	31
3.2 NUMBER DENSITY DETECTION IN SRM PLUMES.....	34
3.2.1 Spatial Distribution of Particle Number Density in an SRM Plume.....	34
3.2.1.1 Case I: Velocity Proportional to \bar{r}_i^{-1}	37
3.2.1.2 Case II: Velocity Proportional to $e^{-(r_i/r_o)^2}$	38
3.2.1.3 Case III: Particles Crossing a Shock Wave.....	39
3.2.2 Number Density Estimation With A Fringe Type LV System.....	42
3.2.2.1 Probability of Two Particles Simultaneously in the Sample Space.	45
3.2.2.2 The Acceptance Ratio.....	52
3.2.2.3 LV System Performance.....	55
3.2.2.4 Measurement of Number Density.....	58
4.0 REVIEW OF POTENTIAL OPTICAL SYSTEM FOR SRM PLUME PARTICLE MEASUREMENTS.....	62
4.1 STATE-OF-THE-ART PSA SYSTEMS.....	62
4.1.1 Optical Particle Size Analyzer Characteristics.....	65
4.1.2 Particle Characteristics Affecting PSA Performance.....	68
4.2 PSA CALIBRATION TECHNIQUES AND STANDARDS.....	71
4.2.1 Quantitative PSA Tests.....	75
4.2.1.1 Size Accuracy and Resolution.....	75

<u>Section</u>	<u>Page</u>
4.2.1.2 Number Density and Accuracy.....	76
4.2.1.3 Operational Uncertainty Specifi- cation.....	76
4.3 PROPOSED SYSTEMS FOR DEVELOPMENT.....	77
4.3.1 Particle Diffusion Spectroscopy.....	77
4.3.2 Schlieren Correlation.....	79
4.3.3 Radiating Particle Velocimeter.....	80
4.4 SUMMARY OF CURRENTLY KNOWN INSTRUMENTATION FOR PARTICLE PARAMETER MEASUREMENTS.....	81
TABLES.....	82
LIST OF FIGURES.....	91
REFERENCES.....	93

PART II ULTRAVIOLET FORWARD MIE SCATTERING

1.0 INTRODUCTION.....	121
1.1 INTRODUCTION TO THE FIGURES.....	123
2.0 DESCRIPTION OF FIGURES.....	126
3.0 DISCUSSION.....	132
REFERENCES.....	134

PART I

ANALYSIS OF OPTICAL INSTRUMENTATION FOR PARTICLE
PROPERTY MEASUREMENTS IN SOLID ROCKET MOTOR PLUMES

1.0 INTRODUCTION

Recent research has been directed toward the characterization of the two-phase (gases and particles) flow associated with solid rocket motor (SRM) plumes.¹⁻⁴ It has been generally concluded that, when possible, noninvasive techniques should be used to characterize these flows. The most advanced of the array of noninvasive instruments which can be used for these kinds of measurements are, in nearly all cases, some type of active or passive optical system. Optical instruments currently are capable of measuring concentrations, temperatures, densities, identifying gas species, measuring particle size and velocity distributions and number density and in some cases even particle index-of-refraction. The primary difficulties in applying these techniques to SRM plume measurements reside in the facts that SRM plumes are: 1) optically active with both particles and gases radiating across a broad portion of the electromagnetic spectrum, 2) extremely high values of particle temperature, size, number density and velocity (very small sizes with temperatures greater than 1000°K, large number densities, and high velocities), and 3) extreme operational environments (e.g. high acoustic levels and temperatures) requiring instrument hardening.

When extreme estimated values of pertinent SRM plume parameters are used in rough estimates of instrument performance, it is often found that many optical measurements are not feasible or can be expected to be exceptionally difficult to achieve. Such estimates suffer from at least two major drawbacks. First, so little experimental information actually exists about requisite plume parameters, that even if simple calculations were justified, they might be in error by a factor of ten or more. Second, an extreme value calculation often neglects the possibility that there may be regions in the plume which are measurable and that such measurements can yield considerable insight into the nature of the entire plume. Nowhere are these factors more apparent than in the analysis of the particle content of SRM plumes. The purpose of this investigation is to examine the applicability of optical instrumentation to the study of SRM plume particle parameters. Specifically, we attempted to define instrument operational limits in terms of plume flow regions where the instrument could be expected to function. We examined optical instruments which yield measurements of 1) particle size, 2) velocity, 3) number density, and 4) spatial distribution. From this analysis we defined the limitations of current instrumentation which can be applied to these problems.

2.0 EXECUTIVE SUMMARY

This investigation considers the limitations of applying optical instrumentation to the measurement of particle properties in SRM plumes. Most of the analysis has been directed toward the use of laser velocimeters and particle sizing instrumentation with the understanding that much of what is concluded can be applied to other kinds of instruments which view localized regions of the SRM plume. We have shown that in addition to particle velocity and size, particle number density can also be estimated using these devices.

A large portion of the analysis is relatively simplistic in approach. In reviewing experimental facts pertinent to particles in SRM plumes we find a great deal of hypothesis ideas and very few experimental facts with which to verify theory or to justify large code development or extensive predictive models. A listing of the major assumptions required for our simple models will clearly show that such large uncertainties exist in known data and models that further refinement should await additional research. Nevertheless, the results found in this study are believed to be sufficiently credible as to at least offer guidance in the direction and application of laser oriented instruments which can measure particle size, velocity and number density. Conclusions pertinent in this regard as deduced from our study follow.

2.1 CONCLUSION SUMMARY

The operational limitations of dual scatter or real fringe, transit time, and local oscillator laser velocimeter systems were examined in this study. For each kind of system two sets of parameters were used in the equations to evaluate system performance in an SRM plume. The first set was used to characterize systems that are usually used in many LV applications. This set of parameters was called the "nominal system." The second set of parameters was chosen to optimize a particular system's performance with components which are within state-of-the-art capabilities. These systems are referred to as "optimum systems." In addition to laser velocimeter systems, two particle sizing interferometer systems were examined. Optimum system performance was assumed for each one. Performance of the systems was found to be comparable. One system was slightly better than the other because of higher frequency response in the particular signal processor used in the system. Direct comparisons and conclusions pertinent to the respective systems follow.

2.1.1 Fringe Type Laser Velocimeter

The measure of LV system sensitivity was taken to be the minimum detectable scattering cross-section for a given signal-to-noise power ratio (10 was assumed). Figure 2 plots the minimum scatter cross-section as a function of mean velocity and turbulence intensity for a background light filter with

a pass band of 10A° . The figure shows that the required scatter cross-section increases $7 \cdot 10^{-14}\text{m}^2$ to $4 \cdot 10^{-12}\text{m}^2$ for a mean particle speed of 500 m/sec. as the turbulence intensity increases from 0.1 to 2. This strong velocity dependence of the minimum scatter cross-section is due to the requirement for optimum spatial resolution. In turn, optimum resolution requires a minimum fringe period and a maximum incident irradiance in the probe volume. The above statements assume fixed signal processor bandwidth (which depends on the turbulence intensity), frequency response, and signal-to-noise ratio. As particle velocity increases, probe volume irradiance must decrease to accommodate fringe period increase which accommodates limited signal processor frequency response. The figure clearly shows how the LV measurements can easily be biased toward the larger scattering cross-sections in a strongly fluctuating flow. As later sections will show, this effect can be significant when particle drag corrections are required for the data. A somewhat surprising feature of the calculations for the nominal system is the fact that the minimum scatter cross-sections are virtually independent of background radiance or equivalently flow or particle temperature. Apparently this effect results from the fact that the scatter cross-sections required to satisfy velocity requirements for the nominal system parameters are so large that they over-shadow scatter cross-section increases required to compensate for background radiance.

While minimum detectable scattering cross-section yields

general results that can be applied to virtually any LV geometry, it leaves no information as to the actual size of the particles which can be detected. This can only be achieved if particular optical system geometries are assumed and if particle shape and index-of-refraction are assumed. Neither particle shape nor index-of-refraction is known for particles in many SRM plumes. To give the reader a ball-park estimate of the particle sizes which the calculations in Figs. 2-11 indicate assume an index-of-refraction of 4/3 (water) and that the particles are spherical in shape. Standard Mie scatter programs will then show that for forward scatter detection, a mean velocity of 500 m/sec and turbulence intensity of 0.1, the minimum detectable particle diameter with an Ar⁺ laser operating at 488 nm and 1 watt of power is 0.3 micrometers. A change in turbulence intensity to 2 requires a particle diameter of about 0.5 micrometers. If the LV optical system is required to operate in a backscatter mode the diameters must increase to 0.8 micrometers for a turbulence intensity of 0.1 and to 1.9 micrometers for a turbulence intensity of 2.

For the optimum LV system the signal processor frequency response was doubled, laser power increased by a factor of 5, the background light filter bandwidth reduced by a factor of 30 and the number of signal cycles required by the signal processor reduced. As Fig. 3 shows, the net result is to reduce the minimum detectable scatter cross-section by a factor

of particle number density for selected values of turbulence intensity. The results show that the local oscillator system is not as sensitive to turbulence as the single particle velocimeters. The system, however, does require surprisingly high number densities and large scattering cross-sections. For example, forward scattering dielectric particles (index-of-refraction of 4/3) in a plume with a turbulence intensity of 0.5 would require particle diameters of the order of 0.5 micrometers for a number density of $10^6/\text{cc}$. In view of the apparent performance of the single particle LV systems, the local oscillator system does not appear to offer any significant advantages over the fringe or transit time LV systems.

2.1.4 Spatial Distribution of Particle Number Density

Three plume velocity conditions were investigated to examine how particle number density would be distributed in the plume. The cases investigated were 1) axial velocity component varying inversely with plume radius, 2) axial velocity component having a Gaussian distribution in plume radius, and 3) the distribution of particles before and after they cross a normal shock wave for AAH double base solid propellant.²⁰

In the first case we found that the particles were uniformly distributed for an axisymmetric plume. Specific values cannot be quoted for number density because it is linearly proportional to particle mass flow rate. In the second case we find the number density least where the flow speed is e^{-1} of its centerline value and increasing toward the edge. This

is because a constant mass combustion rate is assumed across the exit plane. We find also that the number density, if the size distribution is log-normal, strongly depends on the geometric standard deviation, increasing as the deviation increases.

In examining case 3 we find particle number density increasing after the particles have crossed a normal shock front. Both aluminum and aluminum oxide particles were considered for flow Mach numbers ranging between 11 and 3. In the case of a Mach 3 shock we find the particle number density nearly doubling over what it was prior to crossing the shock for a particle diameter of 1 micrometer. The analysis predicts that spatial distributions and changes in number density after crossing the shock will be independent of plume temperature. This follows from the fact that absolute gas viscosity increases roughly as the square root of temperature while the gas velocity, after passing through the shock front is also proportional to the square root of the flow temperature.

2.1.5 Measurement of Number Density With a Fringe Type Velocimeter

A new method for determining particle number density and number density limitations of a fringe type LV has been developed. From the analysis we define a parameter called the "acceptance ratio" which is the number of signals which are acceptably measured divided by those detected. We have found the following to be true:

1. The acceptance ratio is primarily a function of the probe volume cross-section geometry and is independent of the length of the probe volume.
2. As number density increases, acceptance ratio decreases. It follows that data rate for an LV cannot be increased indefinitely by increasing particle number density. For a given optical system geometry there exists an optimum acceptance ratio beyond which the LV data rate will decrease.
3. For constant number density, the acceptance ratio increases as the probe volume cross-section is reduced.
4. Where the probe volume cross-section is such that it is twice as long in the direction of the interference fringes as it is parallel to the fringes, the data rate but not acceptance ratio will increase as the cross-sectional area is further reduced and the number density increased.
5. Comparison of number density estimates using the acceptance ratio method with other experimental techniques shows that the acceptance ratio yields reasonable results.
6. The acceptance ratio method requires only minor modification to existing burst signal processors in order to estimate number density.

2.1.6 Optical Instrumentation Review

A brief review has been given to optical instrumentation which could measure particle properties in SRM plumes.

Examination of state-of-the-art optical instrumentation indicates that the most reliable measurements which can be obtained are those of particle velocity. The optical systems have been proven in hostile environments and the signal processing electronics is exceptionally advanced and sophisticated.

Particle size measurements in SRM plumes are significantly more difficult to achieve than velocity measurements and are

not nearly as reliable. A large portion of this uncertainty arises from the requirement that a particle shape be assumed, particle index-of-refraction be known or assumed, and if a large number of particles are measured simultaneously the size distribution must be known or assumed. Fluctuations in either mean particle size or number density are not easily distinguished by these instruments. The most reliable particle size measurements are those obtained with single particle counter systems. These devices are subject to large errors in SRM plume applications due to the uncertainty in particle shape or index-of-refraction uncertainty and errors introduced by sampling the flow of the single particle counters. PSI systems appear to be the most applicable to SRM plume measurements since they are capable of direct measurement in the plume without a sampling tube to control the particle number density.

A new technique to measure submicron particle sizes called particle diffusion spectroscopy holds some promise. Experimentally its application is reasonably straightforward. Its major weakness appears in the interpretation of the frequency spectrum of the scattered light. Such an interpretation depends, for example, on a knowledge of the viscosity of the gas in which the particles are immersed. Such knowledge is very limited for large regions of the SRM plume where gas temperatures may exceed 2000°K. However, additional research with well controlled experiments certainly appears justified.

2.2 ASSUMPTION SUMMARY

A number of major assumptions have been explicitly or implicitly made in this report. A summary of these assumptions will serve to indicate the limits of the analysis and point out directions for additional research. These assumptions are as follows:

1. Optical perturbations due to flow turbulence have been neglected. Their effects are not negligible. However, their effective analysis will require detailed experimental measurements which are yet to be made and theoretical computations which are beyond the scope of the present research.
2. The primary source of background radiation was assumed to exist at focus of the scattered light receiver. Additional light will enter the receiver from sources near the axis of the optical receiver with the result that more background light will be present than has been estimated here. It is not estimated to be more than an order of magnitude more than assumed and should not significantly affect the results. This effect, however, should be studied in much greater detail since the results could significantly affect corrections and estimates for the performance of nearly all optical instruments applied to SRM plumes.
3. The shot-noise-limited signal-to-noise power ratio has been assumed to be the limiting factor in instrument operation.
4. We have assumed particles in SRM plumes satisfy Stokesian dynamics. This is an area of large uncertainty particularly since particle mass density and shape must be assumed.
5. We have assumed that particles will be in thermal equilibrium with the flow and act as blackbody radiators.
6. In applying the acceptance ratio method to the measurement of number density or prediction of LV performance it was assumed that no errors were made in rejecting multiple particle signals. Experimentally this is rarely the case. Additional analysis should attempt to refine the model in this regard.

2.3 RECOMMENDATIONS

Based on this research the following recommendations are made.

1. Laser velocimeter measurements of SRM plumes should be made with fringe type and transit time instruments to determine optical limitations imposed by plume turbulence.
2. Beam degradation by plume turbulence should be experimentally quantified and incorporated into models predicting instrument performance.
3. The optical characteristics of plume particles at elevated temperatures should be experimentally quantified. Questions which should be answered are:
 - a) What is the particle scattering cross-section at different optical wavelengths as a function of temperature?
 - b) What is the particle index-of-refraction as a function of size and temperature?
 - c) Do submicron particles act as blackbody radiators?
4. The dynamics of "cold" and "hot" particles in flows at elevated temperatures should be experimentally investigated. With adequate results from these studies correlation of LV velocity measurements with plume gas velocity should be possible.
5. Potential particle sizing systems should be experimentally evaluated in controlled experiments where particles at elevated temperatures and known size distributions are used.
6. Scans of SRM plumes with a fringe type LV system to obtain number density spatial distribution estimates should be made. These results when correlated with velocity measurements should lead to a better understanding of the flow field spatial distribution and the SRM combustion characteristics at the exit plane.

3.0 ANALYSIS OF LV SYSTEM PERFORMANCE IN SRM PLUMES

This chapter will examine the effects of SRM exhaust plume parameters which affect the performance of different types of LV systems. LV systems were chosen for a detailed analysis of optical system performance because:

- 1) such systems can provide badly needed information for SRM evaluation and
- 2) their optical performance is such that it will serve to highlight the expected performance of nearly any other optical system applied to SRM measurement.

The primary emphasis in this chapter will be on computing minimum detectable particle scattering cross-sections and instrument number density response as a function of the required system signal-to-noise power ratio.

3.1 PARTICLE SIZES DETECTABLE IN SRM PLUMES

In this section we develop equations to predict the minimum detectable scattering cross-section for particles in a SRM plume. Minimum scattering cross-section will be taken as a primary indicator of instrument performance, since if the particle cannot be detected it obviously cannot be measured. The equations are developed with an eye toward the limitations imposed by plume parameters and the kind of optical system used to generate the scatter. As with nearly all parameters examined in this report there are no sharp

cutoffs in system performance. The limits of the instrument parameters studied have been chosen on the basis of acceptable results in previous experimental work. Thus, there may and in all probability will exist regions of applicability where these systems can perform significantly better than predicted here.

3.1.1 Scatter Cross-Section Required for Single Particle Measurements

The particle size requirements for instruments which measure individual particles are estimated in this section. These instruments include the particle sizing interferometer, fringe type laser velocimeters, the so-called multiple spot or transit time velocimeters, and focused illumination beam particle size analyzers.

In all these instruments (except for the focused system) two or more beams of light are transmitted and focused in the flow of interest. Light scattered from the focus region is collected and analyzed for the parameter of interest. For these kinds of instruments, using photomultiplier tubes (PMT) as photodetectors, the single cycle average shot-noise-limited signal to noise power ratio at the output of the PMT may be written approximately as⁵

$$\frac{S}{N} = \frac{e\lambda}{hc\Delta f} \left[\frac{P_s^2}{P_s + P_B} \right] V^\epsilon \quad (1)$$

where

- ϵ = Photocathode Quantum Efficiency
- λ = Optical Wavelength of Interest
- h = Planck's Constant
- c = Speed of Light
- f = Bandwidth of Signal Processing Electronics
- P_S = Power in Scattered Light Signal
- P_B = Power in background light resulting from all possible radiation sources.
- V = Signal visibility ($0 \leq V \leq 1$ applies to fringe type LV systems and depends on ratio of particle size to fringe period).

Let $P_S/P_B = X$, then equation 1 can be arranged in the form

$$\frac{(S/N) h c \alpha f}{\epsilon \lambda P_B V^2} = \frac{X^2}{X + 1} \quad (2)$$

Before proceeding with a solution of Equation 2 for X, it will be convenient to express Δf and P_B more explicitly. P_B can be written as

$$P_B = N_\lambda \Omega \Delta \lambda \sigma \quad (3)$$

where

N_λ = Spectral radiance ($\text{Wm}^{-2}\text{sr}^{-1} \text{ m}^{-1}$) of the background light resulting from all sources in the plume at the measurement focus.

Ω = Solid collection angle of the scattered light collection optics.

$\Delta\lambda$ = Optical bandwidth of the scattered light collection system.

a = Cross-sectional area of the region from which scattered light is detected.

For optical receivers with F numbers (greater than about 4), defined from the transmitter focus to the scattered light collecting aperture,

$$\Omega = \pi/4F^2 \quad (4)$$

The velocity of the particles passing the focused beam can be written as

$$v = \bar{v} \pm \Delta v \quad (5)$$

where \bar{v} is the mean velocity and $\bar{v} + \Delta v$ and $\bar{v} - \Delta v$ are the upper and lower velocity limits. When particle velocity can be related to the signal frequency f_s and some optical system constant δ (for fringe LV's and PSI systems it is the fringe period, while for transit time velocimeters it is the spot separation) through

$$v = f_s \delta \quad (6)$$

then the signal frequencies will be

$$f_s = \bar{f}_s + f_{s\Delta V} \quad (7)$$

where \bar{f}_s is the frequency corresponding to \bar{v} and $f_{s\Delta V}$ that corresponding to ΔV . The required range for Δf centered at \bar{f}_s is then

$$\Delta f = 2 f_{s\Delta V} \quad (a) \quad (8)$$

$$\Delta f = \frac{2\Delta V}{\delta} \quad (b)$$

The best choice for δ is that value which yields the best spatial resolution for the frequency response of the signal processor. If v_p is the maximum frequency response of the signal processor, it follows

$$v_p^{-1}(\bar{v} + \Delta V) = \delta \quad (9)$$

where v is the smallest possible optical system constant (and hence best resolution element obtainable) for the limiting values of maximum velocity and signal processor frequency response required for a particular measurement. If the turbulence

intensity μ is defined as $\Delta V/V$ then Equation 8b and 9,
 Δf can be expressed as

$$\Delta f = 2 \nu_p \left[\frac{N}{1 + \mu} \right] \quad (10)$$

Using Equations 3, 4, 8b and 10 in the solution of Equation 2
for X , P_s can be written as

$$P_s = \frac{(S/N) \chi \nu / (1 + \mu) h c \gamma_e}{\epsilon \lambda} \left[1 + \left[1 + \frac{\pi / c e \lambda \nu^2 \Delta \lambda N_{\text{eff}}}{(S/N) F^2 h c \gamma_p \mu / (1 + \mu)} \right]^{\frac{1}{2}} \right]^{1/2} \quad (11)$$

We can put P_s in a form more usable for direct system evaluation by defining P_s in terms of the number of photons, n , scattered per measurement cycle. The energy scattered in the measurement cycle is given by Plancks Equation

$$E = n h c / \lambda \quad (12)$$

For the time interval over which the average is being computed, τ , the average scattered power is given by

$$\bar{P}_s = E / \tau \quad (13)$$

For a fringe type LV or PSI system

$$\tau = \delta/v \quad (14)$$

where δ is the fringe period. On the other hand when τ is the separation between two or more focused spots for a transit type LV

$$\tau = \delta/k_o v \quad (15)$$

where k_o is the ratio of spot diameter to spot separation. Comparing Equations 14 and 15 we see that when $k_o = 1$, δ should be understood as the fringe period and when $k_o < 1$, δ should be understood as the focused spot diameter. Hence, Equation 15 is a more general version of Equation 14 and can apply to either a fringe type LV, PSI, or transit time velocimeter. Using Equations 9, 12 and 15 in Equation 13 results in

$$P_s = \frac{n h c \delta / k_o v}{\lambda (\bar{v} + \Delta v)} \quad (16)$$

The maximum value required for P_s in a fluctuating flow would occur for $v = \bar{v} + \Delta v$. Choosing this value for v and equating 16 and 11 we find

$$n = \frac{(S/N)(\mu/(1+\mu))}{\epsilon K_0} \left\{ 1 + \left\{ 1 + \frac{\pi/e \epsilon \lambda V^2 \Delta \lambda N_s \sigma}{(S/N) h c z_p F^2(\mu/(1+\mu))} \right\}^{1/2} \right\} \quad (17)$$

is the minimum number of photons which must be detected in order to produce a signal with a specified S/N. n can now be used to compute the magnitude of the required scattering cross-section.

The average scattered signal power per fringe \bar{P}_s in a fringe type LV system can also be written as

$$\bar{P}_s = P_s / N \quad (18)$$

where N is the number of fringes in the sample space and P_s is the average power scattered from the transmitter focus. \bar{P}_s can be written in terms of the optical system parameters as

$$\bar{P}_s = 2 P_o \sigma \Omega T_r T_k / \pi b_o^2 N \quad (19)$$

where

P_o = Laser power output

b_o = Beam radius at focus

σ = Particle scattering cross-section

T_T = System transmittance to probe volume

T_R = System transmittance from probe volume to receiver
($T_T = T_R$ only when transmission and reception paths through the plume are equal and the optical system efficiencies are identical).

b_0 can be written in terms of N and δ as

$$2 b_0 = N \delta \quad (20)$$

Hence, \bar{P}_S can be expressed as

$$\bar{P}_S = 2 P_o \sigma T_r T_s / N^3 \delta^2 F^2 \quad (21)$$

on equating Equations 21 and 16

$$n h c k_b v / \lambda \delta = 2 P_o \sigma T_r T_s / N^3 \delta^2 F^2 \quad (22)$$

Using Equation 17 and solving Equation 22 for σ we find after arranging terms

$$\sigma = \frac{2 h c}{\lambda P_o G} \left[\frac{N^3 F^2 \delta}{(h \nu) T_r T_s} \right] (S/N) \left[1 + \left[1 + \frac{\pi^2/8}{h c} \left[\frac{1}{S/N} \right] \left[\frac{\lambda \epsilon}{F^2} \right] \left[\frac{\nu+1}{\mu \nu_p} \right] \nu^2 N_\lambda \Delta \lambda \sigma \right]^{1/2} \right] \quad (23)$$

The terms outside the curly brackets have been grouped such that the various terms contributing to the size of the required scattering cross-section are bracketed according to whether they depend on the optical system, the flow being measured or the signal processor requirements. In order to examine how the respective components of the measuring instrument and SRM plume fit together, define the following functions.

$$\Psi \equiv \frac{N^3 F^2 \delta \sigma \Delta \lambda}{\lambda \epsilon P_0} \quad (24)$$

$$\phi \equiv \frac{\gamma \mu N_\lambda}{(1+\mu) T_r T_k} \quad (25)$$

$$\eta^* \equiv \nu_p / (S/N) \quad (26)$$

Equations 24-26 each group parameters associated with the optical system (Equation 24) the flow (Equation 25) and the signal processor (Equation 26). Using these definitions in Equation 23 we find

$$\sigma = 2hc \frac{\Psi \phi}{\eta^*} \left[\frac{\nu_p}{N_\lambda \Delta \lambda \sigma \bar{v}^2} \right] \left[1 + \left[1 + \frac{\pi^2/8}{hc} \left[\frac{N^3 N_\lambda^2 \delta \gamma \Delta \lambda^2 \sigma^2}{P_0 \nu_p^2 T_r T_k} \right] \left[\frac{\eta^*}{\Psi \phi} \right] \right]^{\eta^*} \right] \quad (27)$$

Equation 27 shows that if the functions Ψ and ϕ are minimized

and η^* maximized the required scattering cross-section will be a minimum. By comparing ϕ and η^* for different kinds of instruments for a ϕ determined by a specified flow, an estimate of the optimum system for a given flow can be obtained.

ϕ shows how the character of the flow limits the minimum acceptable scattering cross-section. It may be surprising to find that the minimum acceptable cross-section depends on the particle velocity and turbulence intensity. These factors arise from the fact that the frequency response and bandwidth of the signal processing electronics depend on the velocity and turbulence intensity of the flow. Equation 27 is a generalized analysis which can be applied to either transit or fringe type LV systems. We now consider its application to a number of areas of interest in SRM plume measurements.

3.1.2 Minimum Scatter Cross-Section for Fringe LV's

Table I lists a set of values for two possible LV systems. The nominal system values are chosen as those that could be expected from laboratories that are currently using these types of LV systems. For reference, Fig. 1 shows a typical fringe LV optical geometry. The optimum system values listed in Table I have been chosen as those which could be assembled from off-the-shelf components or are probable limiting values of lasers or signal processors. K values in Table I represent limiting aperture values of "a" for the probe volume cross-section. "a" is written as

$$\sigma = K \frac{\pi}{4} N^2 \delta^2 \quad (28)$$

Using either Equation 27 or 23 we find that the minimum detectable cross-section for the parameters listed in Table I are given by

NOMINAL SYSTEM

$$\sigma = 1.38 \cdot 10^{-12} \bar{V}_{KM}^2 \frac{\mu(1+\mu)}{T_r T_h} \left[1 + \left[1 + 1.8 \cdot 10^{-12} \bar{V}_{KM}^2 \frac{(1+\mu)^3 N_A}{\mu} \right]^{\frac{1}{k_2}} \right] \quad (29)$$

OPTIMUM SYSTEM

$$\sigma = 2.44 \cdot 10^{-16} \bar{V}_{KM}^2 \frac{\mu(1+\mu)}{T_r T_h} \left[1 + \left[1 + 7.415 \cdot 10^{-13} \bar{V}_{KM}^2 \frac{(1+\mu)^3 N_A}{\mu} \right]^{\frac{1}{k_1}} \right] \quad (30)$$

where \bar{V}_{KM} is the particle speed in KM/sec. Figures 2 and 3 plot σ as functions of \bar{V}_{KM} , μ , and temperature. The temperature dependence is derived from N_A assuming that the primary source of background radiation is that resulting from an equivalent blackbody radiance for plume gases and particles. Such an estimate is considered to be one of the major weaknesses of this model. The ability of particles comparable to a wavelength to act as blackbody radiators has been questioned recently.¹ Furthermore, for the bandwidths of the optical filters used in the calculations, it is not clear that

the plume gases can be treated as blackbody radiators. It is quite probable however, that such an assumption places an upper bound on the background radiance which might be encountered in SRM plumes.

3.1.3 Minimum Scatter Cross-Section for Transit LV's and Focused Beam Particle Size Analyzers

Table II lists a set of nominal and optimum values for a transit time LV system. Figure 4 shows the optical layout for a typical system. The frequency response is taken to be the time resolution of correlators which are typically used with these type systems. The system is also assumed to use a single optical frequency and hence, the reduction in optimum optical system power over the fringe system. S/N values have been scaled by a factor of 10 which indicates the transit system's increased sensitivity over the fringe type system. Using the values listed in Table II we find for the scattering cross-sections

NOMINAL SYSTEM

$$\sigma = 2.6 \cdot 10^{-16} V_{NM}^2 \frac{\mu(1+\mu)}{T_r T_a} \left[1 + \left[1 + 4.6 \cdot 10^{-4} V_{NM}^2 \frac{(1+\mu)^3 N_a}{\mu} \right]^{\frac{1}{2}} \right] \quad (31)$$

OPTIMUM SYSTEM

$$\sigma = 2.3 \cdot 10^{-19} V_{NM}^2 \frac{\mu(1+\mu)}{T_r T_a} \left[1 + \left[1 + 1.03 \cdot 10^{-12} V_{NM}^2 \frac{(1+\mu)^3 N_a}{\mu} \right]^{\frac{1}{2}} \right] \quad (32)$$

Figures 5 and 6 plot σ as functions of \bar{V}_{KM} and temperature as was plotted for the fringe type system. These figures, when compared with those for the fringe system, show that the transit system is clearly more sensitive than fringe type LV systems. The true magnitude of system superiority in SRM plume measurements, however, is yet to be established.

3.1.4 Comparison of Transit and Fringe LV System Performance in SRM Plumes

A direct comparison of the two systems' performance in an SRM plume is difficult because of the potential tradeoffs in specific applications. A number of observations are pertinent here, however.

1. Transit LV systems are generally understood to not work well in highly turbulent flows. This is because instrument sampling efficiency is significantly decreased due to particles not passing through both spots. It is therefore necessary to rotate the two spots in the flow until the mean flow direction is found. For SRM burns which last 1-2 seconds, transit systems developed to date would probably have to be modified in order to achieve sufficient rotation and sample rate capacity. Furthermore, the ability of the transit time LV to take large time resolved samples is yet to be demonstrated.
2. Because of their optical design, transit LV systems are sensitive to much smaller scattering cross-sections than a fringe type LV. However, a comparison on this basis may be deceptive since the factors affecting sampling capacity are particle size and size distribution.
3. Scatter cross-section functional dependence on velocity and turbulence intensity is virtually the same for both fringe and transit LV systems.

Observations 1 and 3 are somewhat obvious and require

no further explanation. A simple example will illustrate the significance for observation 2. The backscatter cross-section for small perfectly reflecting spheres can be written as

$$\sigma = \frac{9\pi^5 D^6}{4\lambda} \quad (33)$$

where D is the particle diameter. If λ is assumed to be the same as that given in Tables I and II, then equating the nominal values in Equations 29 and 31 and assuming $\bar{V}_{KM} = 1$, $\mu = 1$, $N = 0$, and T_{TR} = 1, we find the minimum detectable particle diameters for the LV system to be

$$D \text{ (Fringe)} = 0.277 \text{ micrometers} \quad (a) \quad (34)$$

$$D \text{ (Transit)} = 0.066 \text{ micrometers} \quad (b)$$

In this case the transit time LV can detect a particle size a factor of 4.2 smaller than that of fringe system. For the optimum cases this value falls to approximately 2.5. Thus, even though the cross-section detected by the transit system is much smaller than that of the fringe system, the difference in particle size response is not nearly as great or significant.

3.1.5 Minimum Scatter Cross-Section for PSI Systems

The minimum scattering cross-section detectable with a PSI system follows directly from the same equations used to compute that for a fringe type LV system. Some parameters in Table I must be changed to accommodate the limiting frequency response of current known PSI systems. Table III lists these

parameters for two types of PSI systems. System I uses a Bragg cell beam splitter (the interference fringes move) while system II uses a beam splitter which produces stationary fringes. The parameters chosen for each system are those which would yield optimum system performance. Applying the parameters in Table III to equation 23 we obtain σ

SYSTEM I

$$\sigma = 3 \cdot 10^{-14} \bar{V}_{KM}^2 \frac{\mu(1+\mu)}{T_r T_n} \left[1 + \left[1 + 2 \cdot 10^{-8} \bar{V}_{KM}^2 \frac{(1+\mu)^3}{\mu} N_\lambda \right]^{\frac{1}{2}} \right] \quad (35)$$

SYSTEM II

$$\sigma = 2.4 \cdot 10^{-15} \bar{V}_{KM}^2 \frac{\mu(1+\mu)}{T_r T_n} \left[1 + \left[1 + 3.7 \cdot 10^{-8} \bar{V}_{KM}^2 \frac{(1+\mu)^3}{\mu} N_\lambda \right]^{\frac{1}{2}} \right] \quad (36)$$

as a function of \bar{V}_{KM} and values of μ and the temperature for each system are plotted in Figs. 7 and 8. The results show that system performance is practically the same, with system I probably able to detect a slightly smaller particle size than system II. Comparison of Figs. 7 and 8 with 3 shows that, as might be expected, the higher frequency response of velocity signal processor can measure a much broader spectrum of parameters in the plume than can be covered with the PSI.

3.1.6 Scatter Cross-Sections for Local Oscillator LV Systems

In this section we consider the performance of the local oscillator or reference beam LV system in an SRM plume. The analysis is along lines similar to those given for the fringe and transit LV systems. We solve the expression for the signal-to-noise power ratio to obtain an estimate of the minimum scatter cross-section for this instrument. There are additional factors which must also be considered for this system such as frequency broadening of the signal which will be discussed in a later section.

The signal-to-noise power ratio for a local oscillator LV system is given by:

$$\frac{S}{N} = \frac{\epsilon \lambda}{hc \Delta f} \frac{P_s P_{lo}}{P_s + P_{lo} + P_b} \quad (37)$$

where P_{lo} is the power in the local oscillator beam and P_s and P_b are defined as before. Advantage is taken of one of the primary strengths of the local oscillator LV system by requiring that $P_{lo} \gg P_s + P_b$, i.e., the background light from the plume is made insignificant by the local oscillator beam. With this approximation S/N becomes

$$\frac{S}{N} = \frac{\epsilon \lambda P_s}{hc \Delta f} \quad (38)$$

We will assume an optical geometry identical to the fringe

type LV system except that the PMT photodetector is placed in the local oscillator beam. The scattered signal power is given by

$$P_S = n_p \bar{P}_S \quad (39)$$

where \bar{P}_S is the average single particle scattered light power and n_p is the number density contributing to the signal averaged over a single cycle of information. \bar{P}_S is given by Equation 19. In using Equation 19 it should be noted that the maximum solid angle over which a signal can be obtained with a local oscillator is that defined by the illumination beam. In this case it can be shown that⁶

$$\Omega = \lambda^2 / \pi b_o^2 \quad (40)$$

We assume also that for the LV optical system geometry that

$$n_p = \rho_n V_{pv} \quad (41)$$

where V_{pv} is the probe volume. If V_{pv} is assumed to be the e^{-2} intensity contour probe volume (i.e., V_{pv} is independent of particle size and signal amplifier constraints) n_p can be written as⁷

$$n_p = \frac{8\pi}{3} \rho_N b_o^3 / \alpha \quad (42)$$

where α is the angle between the local oscillator and illuminating beam. Using Equations 39, 40, and 42 $\bar{\sigma}$ (the average scatter cross-section) can be written as

$$\bar{\sigma} = \frac{3\pi^2}{16} hc \left(\frac{N^2}{\epsilon \lambda^2 P_o} \right) \frac{2\nu_p N (S/N)}{\rho_N (1+\mu) T_r T_k} \quad (43)$$

where as in previous cases it has been assumed that $2b_o = N\delta$. Table IV lists nominal and optimum system values for the terms in Equation 43. Figure 9 shows the optical geometry for which these parameters apply. We note that in contrast to the other LV systems examined that $\bar{\sigma}$ is independent of particle velocity and depends on $\epsilon \lambda^2$ instead of $\epsilon \lambda$. Using values given in Table IV the minimum mean scatter cross-section required for the local oscillator can be expressed as

NOMINAL SYSTEM

$$\bar{\sigma} = \frac{7.7 \cdot 10^{-7} \mu}{\rho_N (1+\mu) T_r T_k} \quad (44)$$

OPTIMUM SYSTEM

$$\bar{\sigma} = \frac{6.7 \cdot 10^{-9} \mu}{\rho_N (1+\mu) T_r T_k} \quad (45)$$

where ρ_N is expressed in cc^{-1} . Figures 10 and 11 plot the results from Equations 44 and 45 for $\bar{\sigma}$ as a function of ρ_N for various μ values. When the results are compared with those for the instruments which obtain data from single particle scattering measurements, we find the somewhat surprising result that even when the particle number density is so high that the single scatter instruments are sampling in a very inefficient manner, the minimum detectable cross-section for the local oscillator LV system is not much smaller than can be detected with the single scatter instruments.

3.2 NUMBER DENSITY DETECTION IN SRM PLUMES

3.2.1 Spatial Distribution of Particle Number Density in an SRM Plume

Previous sections have developed predictive models that indicated the limitations for velocity and particle sizing instrumentation when applied to SRM plumes. It was shown that one of the principal limiting factors in instrument performance was particle number density. In this section we develop a simple model to predict the spatial distribution of particle number density in an SRM plume. From such a model the trend toward limiting measurement regions in the plume can be established. It should be emphasized that much more sophisticated models are required for accurate predictions. Such factors as particle drag, nozzle geometry and turbulence must ultimately enter into an accurate model of the spatial

distribution. We believe, however, that the model presented here should serve as a reasonable approximation.

Consider Fig. 12. We assume an axisymmetric flow which is divided into a set of concentric cylinders. The radius of each cylinder is r_i and the height is $\bar{v}_i \Delta t$ where \bar{v}_i is the mean particle speed in the coannular cylinder between the radii r_i , r_{i+1} and Δt is the measurement sample time. The volume of the coannular cylinder ΔV_c is then given by

$$\Delta V_c = \pi v_i \Delta t (r_{i+1}^2 - r_i^2) \quad (46)$$

Define the mean radius of the cylinder as

$$\bar{r}_i = \frac{r_{i+1} + r_i}{2} \quad (47)$$

and the width of the cylinder as Z_p

$$Z_p = r_{i+1} - r_i \quad (48)$$

Let Z_p be defined as the probe volume length, then the volume of the annular cylinder can be expressed as

$$\Delta V_c = 2\pi v_i \Delta t \bar{r}_i Z_p \quad (49)$$

The total number of particles N_{pi} contributed to some volume

during a time Δt by the combustion of a given mass $\dot{M}'_i(r_i, t)$ is given by

$$N_{p_i} = \frac{\dot{M}'_i(r_i, t) \Delta t}{\rho_p \frac{\pi}{6} D_3^3} \quad (50)$$

where $\dot{M}'_i = dM/dt$, ρ_p is the particle mass density and D_3 is the third moment of the particle size distribution. It should be borne in mind that for an SRM, the D_3 can be a function of time, velocity, and radial and longitudinal position in the plume.

Particle number density ρ_N in one of the concentric cylinders can be expressed with Equations 49 and 50 as

$$\rho_{N_i} = N_{p_i} / \Delta V_c \quad (51)$$

$$\rho_{N_i} = \frac{\dot{M}'_i(r_i, t)}{\frac{\pi}{3} \rho_p D_3^3 V_i \bar{r}_i Z_p} \quad (52)$$

Equation 52 shows that for M' constant, the observed number density decreases inversely with velocity (for a constant particle supply and fixed Δt the volume increases linearly with velocity, hence, the number density must decrease). A more comprehensive model or code would consider the spatial distribution for M' as a function of time and the functional

dependences of D_3 and v_i . Such a study is beyond the scope of this paper. We will consider some simple cases for v_i and D_3 which might well exist in an SRM plume.

3.2.1.1 Case I. Velocity Proportional to \bar{r}_i^{-1}

We assume in this case that the particle size distribution is a simple log-normal distribution independent of spatial position and that M is constant. In this case D_3 can be written as

$$D_3 = \bar{D}^3 e^{4.5 \sigma_g^2} \quad (53)$$

where \bar{D} is the numeric median diameter and σ_g is the logarithmic geometric standard deviation. This size distribution will also be assumed for all the other cases to be considered. We assume that v_i can be expressed as

$$\begin{aligned} v_i &= V_o (r_o / \bar{r}_i) \\ r_i &\gg r_o \\ V_o, r_o &\text{ CONSTANT} \\ \bar{r}_i &\gg Z_p \end{aligned} \quad (54)$$

This dependence can be assumed to apply in certain regions near the edge of the plume. Using Equations 53 and 54 in Equation 52 we obtain

$$\rho_{N_p} = \frac{\dot{M}' e^{-4.5 \sigma_g^2}}{\frac{\pi}{3} \rho_p \bar{D}^3 V_o r_o Z_p} \quad (55)$$

Equation 55 shows that the observed number density will be constant with position. We can estimate the maximum observable number density $\rho_{N_p:_{max}}$ by using equations developed in previous sections. Z_p for a fringe type or local oscillator LV system or a PSI system can be written as

$$Z_p = 4 b / \alpha \quad (56)$$

Using equations 9 and 20 Z_p can be expressed as

$$Z_p = \frac{2 N \bar{V}^2 (1+\mu)^2}{\lambda Z_p^2} \quad (57)$$

With Equation 57, Equation 55 can be expressed as

$$\left(\rho_{N_p:_{max}} \right) = \frac{\dot{M}' \lambda Z_p^2 e^{-4.5 \sigma_g^2}}{\frac{2}{3} \pi^3 \rho_p \bar{D}^3 V_0 f_0 \bar{V}^2 (1+\mu)^2} \quad (58)$$

Figure 13 plots $\left(\rho_{N_p:_{max}} \right) / \dot{M}'$ as a function of \bar{D} and σ_g . For the set of values given in Table V. System parameters listed have been chosen so that either the local oscillator or fringe type LV system would apply.

3.2.1.2 Case II. Velocity Proportional to $e^{-(r_i/r_o)^2}$

For Case II the same assumptions are made for Case I

except that the spatial velocity distribution is given by

$$v_1 = v_o e^{-(\bar{r}_i/r_o)^2} \quad (59)$$

Using Eqn. 59 in Eqn. 52 with the assumptions made for Case I yields

$$\rho_{Np_i})_{max} = \frac{\dot{M}' \lambda \nu_p c^{-4.5 \sigma_3^2} (\bar{r}_i/r_o)^2}{\frac{2}{3} \pi^3 \rho_p D^3 V_o \bar{V}^2 (1+\mu)^2 \bar{r}_i} \quad (60)$$

Equation 60 shows the interesting result that the particle number density is least near the center of the plume and increases significantly near the edges for this case.

Figure 14 plots $\rho_{Np_i})_{max}/\dot{M}'$ as a function \bar{D} when $r_i = r_o$ and the same parameters given in Table V. Figure 15 plots $\rho_{Np_i})_{max}/\dot{M}'$ as a function of r_i for $\bar{D} = 10^{-6}$ m and $\sigma_3 = 0.5$. to illustrate the relative numeric variation of $\rho_{Np_i})_{max}$ with r_i .

3.2.1.3 Case III. Particles Crossing a Shock Wave

In this case we will model the particle number density after crossing a shock wave. The shock wave will be modeled as an instantaneous step change in gas velocity. We will also assume that Stokesian particle dynamics apply (i.e. spherical

particles affected only by drag and apparent mass). For these assumptions the equations of motion for the particle can be solved to yield

$$\frac{V_p - V_1}{V_0 - V_1} = e^{-\gamma' t} \quad (61)$$

where V_p is the particle velocity, V_0 is the gas velocity before the step change and V_1 is the gas velocity after the step change. γ' is a constant defined by

$$\gamma' = \frac{12\nu}{D^2} \frac{3\rho}{2\rho_p + \rho} \quad (62)$$

$$\gamma' = \eta/D^2$$

where ν is the gas viscosity, ρ the density and ρ_p the particle density. "t" is time after the particle crosses the step change in velocity. It will be convenient to specify time in terms of distance, z , away from the step change and V_1 the velocity after the step change,

$$t = z/V_1 \quad (63)$$

We also simplify the calculation by assuming that the particle size distribution is monodisperse ($m_D \ll 1$). Using Eq. 63-65

in 52 and making previous assumptions with respect to the other applicable parameters we obtain

$$\rho_{Np_i} = \frac{\dot{m}' \lambda \nu_p^2}{\frac{2}{3} \pi^3 \rho_p \bar{D}^3 \bar{V}^2 (1+\mu) \bar{r}_i [V_e (1 - \exp(-\eta z / \bar{D}^2 V_e)) + \sqrt{V_e \exp(-\eta z / \bar{D}^2 V_e)}]} \quad (64)$$

Our interest is to note the change in apparent number density before and after the particles cross the shock. In the region before the shock, the particle number density is constant and given by

$$\rho_{Np_i} = \frac{\dot{m}' \lambda \nu_p^2}{\frac{2}{3} \pi^3 \rho_p \bar{D}^3 \bar{V}^2 (1+\mu) \bar{r}_i V_o} \quad (65)$$

defining $\Delta \rho$ as the ratio of number density before the shock to number density after the shock, we can use Eq. 64 and 65 to write

$$\Delta \rho = \frac{V_e}{V_o} (1 - \exp(-\eta z / \bar{D}^2 V_e)) + \exp(-\eta z / \bar{D}^2 V_e) \quad (66)$$

It is convenient to write Z as

$$Z = \xi (\bar{D}^2 V_1 / \eta) \quad (67)$$

where ξ is a constant. $\Delta \rho$ is plotted in Fig. 16 as a function of ξ for values of V_1/V_0 corresponding to V_0 , Mach numbers of 1.1, 1.5, 2.0, 2.5, and 3.0 across a selected shock which could exist in an SRM plume. Figures 17a and b plot Z/ξ as a function \bar{D} for the same values of V_1/V_0 used in Fig. 16. AAH propellant is assumed and the particles are assumed to be either Al, or Al_2O_3 and initial flow temperatures of 10^3 and 2×10^3 °K are used to compute η . The absolute viscosity of the flow was computed using Equation 2r-12a, p. 2-237 in the third edition of the American Institute of Physics Handbook for temperatures computed on the V_1 side of the shock.

3.2.2 Number Density Estimation with a Fringe Type LV System

The estimation of particulate number density in a fluid is a particularly difficult experimental problem subject to numerous sources of error. For example, mechanical sampling systems such as cascade impactors must sample iso-kinetically and measurements only yield number density estimates from computations involving weight measurements for each stage of the impactor corresponding to 'equivalent' aerodynamic particle diameters.^{8,9} The resulting estimate is thus not a direct numeric count but rather an 'equivalent' number

density. Because mechanical samples often introduce unacceptable perturbations in the flows being measured, optical and other more exotic techniques have been developed, each having its own peculiarities and limitations.¹ These methods have ranged from multiple wavelength transmissometer schemes to sophisticated multiple scatter angle techniques involving highly sophisticated inversion schemes and considerable computational effort. Single particle optical counters which determine a particle size from a scattered light measurement and maintain an accurate particle count rate for a fixed sample flow rate are among the most accurate devices for estimating numeric number densities. They are, however, cumbersome to use except in the most benign environments because of the need to draw a fluid sample through their optically sensitive region.

In hostile environments such as encountered in SRM plumes or in flows with particles that may be affected by its sampling system, the optical counter cannot be used. The purpose of this section is to show how data obtained with a dual scatter or fringe type laser velocimeter (LV) may be used to estimate particle number density. The method utilizes data which is readily available from fringe LV systems and should therefore be straightforward to implement on a wide variety of experiments where these devices are in use and

number density data are of interest.

In addition to providing a number density estimate from LV data, the method may also be used to address a problem often encountered in the application of the LV. This problem is often stated in the question, "given the constraints of the optical system, can a velocity measurement be obtained when the particle number density is high?" The answer to such a question has a fundamental bearing on the capability of an LV to obtain measurements in an SRM plume. The general conclusion reached by several workers in this regard is that fringe type LV systems 'work well' when particle number density is 'low' and poorly when it is 'high.'^{10,11} Low values of particle number density are taken to mean that on the average only one particle or less exists in the probe volume during the particle transit time. Such a requirement is difficult to quantify and is highly limiting in specifying the allowable number density that can be utilized for fringe type LV measurements. For example, previous research has shown that the probe volume or sample space of an LV is dependent on the scattering cross-section of the particle.¹² Thus, even for a very high overall number densities, the LV may be applied successfully since it can only respond to those particles with scattering cross-sections larger than some threshold value. Furthermore, because particles in a flow are not isotropically distributed, regions will exist as

shown, for example, in Section 3.2.1 where the particle number density may be small enough to easily obtain a particle measurement while in other regions it may be much too high. The approach taken in this work in attempting to answer the question of LV performance has been to compute the probability that two particles exist within some distance of each other for each of the three orthogonal coordinates in the probe volume or sample space. It is assumed that the logic circuits of the LV signal processor are sufficiently accurate to reject all signals resulting from two or more particles. The resulting probability distribution for particle separation in three dimensions and this assumption lead to the definition of a signal acceptance ratio, A. 'A' specifies the ratio of number of particles measured to those detected. 'A' is then taken as the sampling efficiency of the LV and is a quantitative measure of how well the LV performs as a function of number density. Conversely, if the LV optical system parameters and signal processor characteristics are carefully specified, then a measurement of 'A' can be used to estimate particle number density.

3.2.2.1 Probability of Two Particles Simultaneously in the Sample Space

The development of the probability density distribution for two particles simultaneously in the sample space is based on the well-known random walk analysis commonly found in text books on statistics. The steps leading to the result

are briefly sketched in order that the reader fully understand the implications and limitations of the analysis.

The following assumptions are made:

1. Particle size is small compared to all sample space dimensions.
2. All particle positions are randomly distributed in space.

Assumption 2 leads to the assumption that the probability $P(X, Y, Z)$ of a particle existing at some X, Y, Z position in a rectangular coordinate system may be written as

$$P(x, y, z) = P(x) P(y) P(z) \quad (68)$$

Where $P(X)$, etc. is the probability that the particle position is at the coordinate X. Consider Fig. 18, a dimension in the X, Y, Z coordinate system is divided into a set of cells of dimension ϵ' . A particle may occupy the cell or not, hence, the probability of a cell being occupied is $\frac{1}{2}$. Let some arbitrary cell be chosen as the origin and count cells to the left until a cell is found which is occupied. Let this number of cells be p. Next let q be the number of cells counted from the origin before the next successive occupied cell is found. Define the total number of cells involved by n_0 while the number of cells between the particle is m, then

$$p + q = n_0 \quad (69)$$

$$p - q = m \quad (70)$$

The probability that a sequence n_0 leads to a value of m P_{n_0} is given by

$$P_{n_0, m} = \frac{n_0!}{p! q!} \left(\frac{1}{e}\right)^{n_0} \quad (71)$$

Applying Stirling's formula for $n_0!$ and manipulating variables there results⁷

$$P_{n_0, m} \approx \left(\frac{e}{\pi n_0}\right)^{\frac{n_0}{2}} e^{-m^2/2n_0} \quad (72)$$

$$|m| \ll n_0$$

It is convenient to make the following identities

$$x = m \epsilon' \quad (73)$$

$$X = n \epsilon'/2 \quad (74)$$

where x is the spatial displacement between particles and X is the arithmetic average of the distance between the particles. Substituting Eqn. 73 and 74 into Eqn. 72 results in

$$P_{n,m} \approx \left(\frac{\epsilon'}{\pi X}\right)^{1/2} \exp\left(-\frac{x^2}{4\epsilon'X}\right) \quad (75)$$

Let $P(x,X)dx$ be the probability of a distance x to $x+dx$ existing between particles when the average distance is X .

For small dx , $P_{n_0,m}$ is approximately constant. Then $P(x,X)dx$ is $P_{n_0,m}$ multiplied by the number of values of m occurring in dx for fixed n ,

$$P(x,X)dx = P_{n,m} \frac{dx}{\epsilon} \left(\frac{1}{2}\right) \quad (76)$$

A factor of $\frac{1}{2}$ enters since for fixed values of n , values of m are either all odd or all even. Equation 75 can now be expressed using Eqn. 76 as

$$P(x,X)dx = \frac{1}{(4\pi\epsilon'X)^{1/2}} \exp\left(-\frac{x^2}{4\epsilon'X}\right) dx \quad (77)$$

The arithmetic average distance between particles along a specified direction for a given number density ρ_N is given by

$$X = \rho_N^{-1/3} \quad (78)$$

The cell length a' is chosen to be the fringe period of the LV system. With these identifications

$$P(x, X) dx = \left(\frac{\rho_N^{1/3}}{4\pi\delta} \right)^{1/2} \exp\left(-\frac{\rho_N^{1/3} x^2}{4\delta}\right) dx \quad (79)$$

It is convenient to define σ_0 as

$$\sigma_0 \equiv \rho_N^{1/3}/4\delta \quad (80)$$

With these results and definitions the probability of finding two or more particles in some increment of space $\Delta x \Delta y \Delta z$ when the particles are separated by some average distance X is given by

$$P(\Delta x \Delta y \Delta z) = \int_0^{\Delta x} \int_0^{\Delta y} \int_0^{\Delta z} P(\Delta x, X) P(\Delta y, X) P(\Delta z, X) dx dy dz \quad (81)$$

Because the integrals are separable and identical in form, differing only in the limits of interest, only one is explicitly evaluated. Using Equations 79 and 80 for this evaluation gives

$$\int_0^{\Delta X} P(\Delta x, X) dx = \sqrt{\frac{a_0}{\pi}} \int_0^{\Delta X} \exp(-a_0 x^2) dx \quad (82)$$

which readily yields

$$\int_0^{\Delta X} P(\Delta x, X) dx = \frac{1}{2} \operatorname{erf}(\sqrt{a_0} \Delta X) \quad (83)$$

An accurate approximation for a closed form solution to Eq. 83 may be obtained by using an approximation due to Menzel:¹³

$$\operatorname{erf}(b) \approx [1 - \exp(-4b^2/\pi)]^{1/2} \quad (84)$$

Therefore, the solution to the integral is

$$\int_0^{\Delta X} P(\Delta x, X) dx = \frac{1}{2} [1 - \exp\left(-\frac{4a_0 \Delta X^2}{\pi}\right)]^{1/2} \quad (85)$$

In the limit as $\Delta X \rightarrow \infty$ the integral has a value of $\frac{1}{2}$. Since in the limit it is required that the particles be somewhere in the box $\Delta x \Delta y \Delta z$ the probability of finding the particles

separated by some distance is normalized to the value for infinite separation.

$$P(\Delta x) = \frac{\int_0^{\Delta x} P(x, X) dx}{\int_0^{\infty} P(x, X) dx} \quad (a)$$

$$P(\Delta x) = 2 \int_0^{\Delta x} P(x, X) dx \quad (b) \quad (86)$$

$$P(\Delta x \Delta y \Delta z) = B P(\Delta x \Delta y \Delta z) \quad (c)$$

Using Equations 85 and 86 in Equation 81 and manipulating variables the desired functional relationship for $P(\Delta x \Delta y \Delta z)$ is obtained

$$P(\Delta x \Delta y \Delta z) = B^{\frac{1}{2}} \exp\left(-\frac{\rho_N^{\frac{1}{3}} (\Delta x^2 + \Delta y^2 + \Delta z^2)}{4\pi\delta}\right) \times \\ \left[\sinh\left(\frac{\rho_N^{\frac{1}{3}} \Delta x}{2\pi\delta}\right) \sinh\left(\frac{\rho_N^{\frac{1}{3}} \Delta y}{2\pi\delta}\right) \sinh\left(\frac{\rho_N^{\frac{1}{3}} \Delta z}{2\pi\delta}\right)\right]^{\frac{1}{2}} \quad (87)$$

$P(\Delta x \Delta y \Delta z)$ represents the probability that two or more particles will be found in a volume $\Delta x \Delta y \Delta z$. By using values of Δx , Δy and Δz appropriate to the LV probe volume or sample space, an estimate can be made of how often two or more particles may be expected in the probe volume.

3.2.2.2 The Acceptance Ratio

The results from the previous section can now be used to define an experimental parameter called the acceptance ratio, A. A is defined as

$$A = \frac{\text{Number of Signals Accepted for Measurement}}{\text{Number of Signals Detected}} \quad (88)$$

If it is assumed that the logic circuits in a burst type LV signal processor are totally effective in rejecting all multiple particle signals, then if N is the total number of signals detected, the number of signals rejected is $N_p (\Delta x \Delta y \Delta z)$ where $\Delta x, \Delta y, \Delta z$ are appropriate probe volume or sample space dimensions. With these assumptions and definitions, Equation 87 can be used to express A as

$$A = 1 - p(\Delta x \Delta y \Delta z) \quad (89)$$

In order to explicitly express A in terms of LV system parameters it is convenient to make the following identifications. Assume an LV system capable of measuring one velocity component, then let Δy be the dimension parallel to the velocity component measured. Express Δy as

$$\Delta y = N_L \delta \quad (90)$$

where N_L is taken to be the average number of observable

cycles generated in the LV signal. Let Δx be the dimension perpendicular to Δy and the bisector between the beams (i.e. in the fringe model of the LV it is parallel to the fringe planes). Write Δx as

$$\Delta x = K N_s \delta \quad (91)$$

where K is a constant which specifies the relative size of Δx and Δy . In practice $\Delta x < \Delta y$. This may result, for example, from logic constraints in the signal processor or slit apertures placed in the receiver optics to limit the size of the probe volume. Δz is assumed parallel to the bisector between the beams and may be expressed in terms of Δx and Δy . For most LV systems currently in use $\Delta z \gg \Delta y$. For example, if Δz were made to correspond to the length of the transmitted probe volume corresponding to the average e^{-2} intensity contour, then

$$\Delta z = 4N_s \delta / \alpha \quad (92)$$

where α is the angle between the beams. A typical value of α is 0.1, making $\Delta z = 40\Delta y$. When $Q_{\sqrt{\Delta z^2}}^{1/2} / 2\pi\delta$ is computed for the range of values commonly encountered in most LV systems and applications it is found that

$$\sinh\left(\frac{\rho_N^{1/3} \Delta z^2}{2\pi\delta}\right) \approx \exp\left(\frac{\rho_N^{1/3} \Delta z^2}{2\pi\delta}\right)/2 \quad (93)$$

for

$$\frac{\rho_N^{1/3} \Delta z^2}{2\pi\delta} \gtrsim 2 \quad (94)$$

It follows that for most purposes A will be independent of Δz . With these definitions and approximation 'A' can be explicitly expressed as

$$A = 1 - 2 \exp\left(-\frac{\gamma}{2}(1+k^2)\right) [\sinh(\gamma) \sinh(k^2\gamma)]^{1/2} \quad (95)$$

$$\gamma = \frac{\rho_N^{1/3} N_L \delta}{2\pi} \quad (96)$$

Equations 95 and 96 show that if N_L , δ , and K (all experimental constants for a given LV system) are known, then a determination of A can be used to compute ρ_N . Conversely specification of ρ_N with a required K, N_L and δ provides an estimation of the acceptance ratio. If A is taken as a measure of system performance, then examination of the response of A for variation in system parameters will show how to optimize the system for expected operational conditions.

3.2.2.3 LV System Performance

Figure 19 plots A as a function of γ for selected values of K between 1.0 and 0.2. As the figure shows, for fixed N_L and δ , significant increases in acceptable P_N for given values of A can be achieved by reduction of the probe volume cross-section through apertures (a fact well-known to anyone who has used an LV). Figure 20 graphically illustrates this dependence by plotting γ as a function of K for selected values of A . The figure shows for example that if $A = 0.1$, then reducing K from 1 to 0.2 when N_L and δ are held constant results in an effective increase of acceptable P_N by a factor of nearly 8000.

In applying an LV to a turbulent flow measurement, it may be necessary to add particles to the flow to satisfy sampling rate requirements. (This will not be very likely for most SRM measurements). However, Fig. 19 shows that as the particle number density increases, the acceptance ratio decreases. Eventually, the number density will reach a level where the data rate actually decreases with increasing number density because the acceptance ratio has become so small. As the number density increases, a point will be reached where numerous particles always exist in the sample space and either it becomes expedient to switch to a local oscillator optical system or to use signal processors which optimally function with continuous type signals. The question to be

answered in this section is 'for fringe type LV systems with fixed constraints, how large can the number density be made and still increase the data rate?' To answer this question, note that the data rate \dot{i}_d can be written as:

$$\dot{i}_d = \dot{N}_p A \quad (97)$$

where \dot{N}_p is the rate at which particles pass through the sample volume. Assume that the time scales involved are such that A can be assumed constant and that the flow velocity, V , is constrained to the dimension normal to the cross-sectional area σ_{pv} of the sample space, then \dot{N}_p can be written as

$$\dot{N}_p = \rho_N V \sigma_{pv} \quad (98)$$

Combining Equations 97 and 98, taking the derivative with respect to ρ_N , and making use of Equation 96 there results

$$\frac{\partial \dot{i}_d}{\partial \rho_N} = V \sigma_{pv} \left[A + \frac{V}{3} \frac{\partial A}{\partial V} \right] \quad (99)$$

\dot{i}_d is a maximum when the bracketed term in Equation 99 is zero. Using Equation 95 and performing the indicated algebra in Equation 99, it is found that $\frac{\partial \dot{i}_d}{\partial \rho_N}$ is zero when

$$A = \frac{\gamma}{6} \frac{[(1 - \coth(\gamma)) + K^2(1 - \coth(K^2\gamma))]}{[\gamma[(1 - \coth(\gamma)) + K^2(1 - \coth(K^2\gamma))] - 1]} \quad (100)$$

Figure 21 plots A as a function γ for various values of K. The figure shows the interesting result that after K reaches about 0.5, A becomes nearly constant. This means that the acceptance ratio or equivalently the LV sampling efficiency cannot be improved by, for example, further reduction of the sample space cross-section via apertures. However, further reduction of K will provide an increase in the data rate for increasing number density.

For the case where A is chosen to yield a maximum value for \dot{n}_s as a function of ρ_N , γ is assumed constant. Solving Equation 96 for ρ_N with γ constant yields

$$\rho_N = (2\pi\gamma)^3 / N_s^6 S^3 \quad (101)$$

Equation 101 shows this extreme value of ρ_N is much more drastically affected by the number of signal cycles generated by a scattering particle than by the absolute magnitude of the LV fringe period. Hence, in seeking to optimize data rates for a particular LV geometry it is most expedient to reduce the number of cycles in the signal rather than to change the fringe period.

3.2.2.4 Measurement of Number Density

In this section the measurement of number density with a fringe type LV optical system using a burst type signal processor is described. As has been shown, the acceptance ratio may be interpreted as a measure of the sampling efficiency of the LV. Sampling efficiency is understood to mean how often the instrument can acquire a measurement for a randomly occurring (in time) signal input with a rather broad spectrum of potential features. For example, although signal shapes will generally be the same, signal frequency, amplitude, noise signal periodicity, and number of cycles in the signal can be widely variable between signals. LV signal burst processors are designed to accommodate a broad spectrum of signal variation and still measure the signal time period or frequency. Additionally these processors contain logic systems which are designed to accept only signals of a certain amplitude, signals which have a certain number of cycles, signals which are periodic within some acceptable error limit, or signals which have a minimum signal-to-noise ratio. The model from which the acceptance ratio was derived assumed that all signals resulting from a single particle would be measured while all signals resulting from two or more particles would be rejected. The logic circuit designed to test the periodicity of the signal rejects signals resulting from particles accelerating across the sample space and from those signals which result from two

or more particles. The signal from two or more particles is expected to be detectably aperiodic over some portion of the signal because of the random phases generated by random particle arrival times. It is highly improbable that an accelerating particle in most flows would be observed and rejected with current burst processors. For example, a variation in signal frequency (or equivalently particle velocity) of 1% would pass a typical burst processor test. A particle crossing a probe volume 100 micrometers in diameter with a mean speed of 10m/sec would have to experience an acceleration greater than 10g in order to be rejected. Therefore it will be assumed that all signals rejected on the basis of being aperiodic will result from two or more particles. With this assumption it is then only necessary to count the number of signals which are accepted by the logic circuit testing signal periodicity and divide by the total number of signals detected by the circuit to obtain the acceptance ratio. This approach has been employed in the LV signal processor developed and applied at UTSI. In addition to measuring particle speed, the logic circuits in the UTSI signal processor are also used to control a signal processor used to measure signal visibility from which particle size is deduced. In this operational mode the system is called a particle sizing interferometer (PSI).

A set of experiments performed with the PSI will illustrate the application of the acceptance ratio to the determination

of number density. In these experiments the objective was to measure the particle size distribution and number density of condensate formed by samples of solid rocket propellant fired into a large (9m^3) chamber at atmospheric pressure and preset temperature and humidity conditions. The PSI optical system used for these measurements is illustrated in Fig. 22. The transmitter utilized a 30 milliwatt HeNe laser and generated a 4.64 micrometer fringe period projected about 30 cm inside the box. The receiver utilized an F/6, 15 cm diameter diffraction limited aspheric telescope. An EMI 9781R photomultiplier tube apertured by a variable slit was used as the photodetector. The slit was calibrated in laboratory tests and set for a K value of 0.4 when the image of the probe volume fringe set was projected through the receiver. During initial experimental operation it was found that the average signal N_L was 14. N_L was determined by observing the pulse output from the zero crossing detector circuit in the LV signal processor. Data acquired by the system was entered in a small computer memory and printed in hard copy for analysis. Part of the data record was the number of measurements accepted as valid and the number rejected on the basis of the signal frequency varying more than 5% during the particle transit time. From these data acceptance ratios were computed and number density estimates made. In addition to the PSI measurements, particle size and number density measurements were also made using a commercially available optical particle counter.

(Climet), a cascade impactor, and a multiple wavelength transmissometer. The transmissometer measurements yielded a mean size and number density for an assumed log-normal distribution. Table VI summarizes the results from 3 of these tests (details of the tests can be found in Ref. 14). Considering the wide variation in the kinds of methods used to obtain the data, the results are not surprising, and in test 493 are in remarkably good agreement. The transmissometer measurements should be interpreted to reflect an average of the parameters along the transmission path. The cascade impactor reflects an equivalent aerodynamic diameter which depends strongly on the mass distribution of the particles. The PSI and commercial optical counter are both designed to measure single particles. However, the PSI performed an *in situ* measurement over a smaller volume of gas containing particles while the commercial counter measured continuously with a drawn sample from the chamber. It should also be borne in mind that each system has a different limit in particle size sensitivity. It was found, for example, that a factor of two change in photomultiplier tube gain could change the measured number density by an order of magnitude. Estimates of the corresponding change in particle size sensitivity were found to be consistent with the directly measured size distributions.

4.0 REVIEW OF POTENTIAL OPTICAL SYSTEM FOR SRM PLUME PARTICLE MEASUREMENTS

In this chapter we present a brief review of different types of optical systems which could be applied to the measurement of particles in SRM plumes. Chapter 3 presented models which could be used to predict the performance of these instruments when given specific instrumentation operating characteristics. These models were developed around velocity measuring instruments which were discussed in detail. Relatively little was discussed in terms of specific particle sizing or temperature measuring instrumentation. In order that the reader understand the options available in state-of-the-art instrumentation for measuring particle size we first discuss particle size analyzer (PSA) systems in general including mechanical sampling systems. We then briefly consider other techniques for the measurement of particle temperature and mass.

4.1 STATE-OF-THE-ART PSA SYSTEMS

Tables VII and VIII provide a comprehensive summary of the most commonly used optical and mechanical PSA systems and techniques. Generally speaking, an optical PSA system provides an estimate of particle size from some optical scattering characteristic of the particle. On the other hand, mechanical PSA systems provide estimates of equivalent aerodynamic particle size by obtaining some measure of particle

drag in a well defined flow. Optical PSA measurements are usually sensitive functions of particle index-of-refraction, ratio of diameter to illuminating wavelength, particle shape and viewing direction of the scattered light. Mechanical PSA measurements are usually functions of particle size, shape, density, and the density of the fluid in which the particles are immersed.

Often in a mechanical PSA, for example, a cascade impactor, mass fractions of an aerosol are divided according to the product of the square of the particle diameter and density in much the same manner as a shock wave fractionates particles sizes with distance as discussed in Section 3.2.1.3. After a sample is obtained, the individual mass fractions are carefully weighed. From these measurements, a knowledge of the particulate specific gravity, and the supposed size separation cut points in the separate mass fractions, a volumetric mean diameter and number density can be estimated. It is easy to see that data acquisition with these kinds of PSA systems is slow, tedious, cannot be easily used with liquid or chemically active or high temperature particles and is subject to numerous potential experimental errors. Nevertheless, there is the comfort of having a sample to work with at one's leisure in a laboratory, sample weighing is as direct a mass measurement as possible, and a broad particle

size range can be covered.

Optical PSA systems can potentially size particles at rates easily above 10^3 /sec and minimize manpower required to obtain a size distribution through computer automation and control. Because the particles need not be handled, these PSA measurements can be made nearly perturbationless with respect to the aerosol being observed. These systems are usually designed to minimize the effects of particle index-of-refraction or viewing direction on the scattered light signal. Most optical PSA's determine particle size either through a measurement of the scattered signal magnitude or the ratio of scattered light magnitudes in two directions. Because scatter magnitude varies as the volume of the particle when the particle size is comparable to a wavelength and as the particle cross-sectional area as the size increases above 2-3 wavelengths, the linear amplitude response of state-of-the-art electronic amplifiers limit these instruments to about a 10:1 size range for any one electronic arrangement or optical geometry. Of course, practically any instrument can move the center of this 10:1 size range up and down the scale of particle sizes. Thus, the "Range of Measured Parameters" in Table VII lists the extremes over which the optical PSA 10:1 size range can be adjusted.

When choosing a PSA for use in a particular experiment, preference is usually given to one using an optical system.

This is because optical PSA's can be made perturbationless, they minimize labor, have very rapid response times, and they can be used with liquid and chemically active particles in extremely hostile environments. Thus, because our interest is in measurements obtained in SRM plumes, most of the discussion will be slanted toward optical PSA's. However, it should be borne in mind that mechanical PSA systems must be considered as potential competitors and systems for experimental control when optical PSA measurements become intolerably uncertain.

Past experience has shown that each PSA type illustrated in Table VII has its own peculiar characteristics. These characteristics can cause major uncertainties in particle size measurements should they be used to measure particles with which they are not calibrated, since in field and laboratory tests of SRM plumes, non-calibration type particles are the exception rather than the rule. A careful study of PSA sizing capabilities should seek to clarify PSA response to a broad range of particle characteristics. Section 4.1.1 discusses some of the more important characteristics of PSA systems that should be considered in this context.

4.1.1 Optical Particle Size Analyzer Characteristics

PSA systems which attempt to correlate particle size with scattered signal magnitude (systems 3,4,5 and 7

in Table VII) reference the scatter magnitude to some equivalent scattered magnitude from a calibration particle of known shape, size and index-of-refraction. Favorite choices for this kind of calibration are monodisperse latex or polystrene spheres which have been sampled and sized for calibration using an electron microscope. They are placed in a dilute methanol solution and dispersed through the PSA for a calibration of size-to-signal magnitude. By taking account of the PSA optical geometry, Mie-Lorenz scattering theory can be used to compute the relative functional dependence of the scatter magnitude with particle size. The calibration particle scatter magnitude provides an absolute reference point for the function correlating size and signal magnitude. If the optical system of the PSA collects most of the scattered light magnitude in the forward scattering direction [see, for example, the Climet PSA (instrument 3) in Table VII] then the scattered magnitude is nearly independent of index-of-refraction when the particle does not absorb light. Figure 23a shows such a curve for the Climet instrument. Figure 23b shows that for particles with imaginary indices of refraction (i.e., they are strongly absorbing) the calibration curve is a strong function of index-of-refraction and is not monotonic with respect to particle diameter. Hence, particle size data from PSA systems of this type must be interpreted in terms of the

equivalent calibration particle diameter.

PSA systems which compare the ratio of scattered intensities in two or more observation directions or attempt to determine size from the shape of the scattered radiation pattern depend for their accuracy on theoretical predictions of scatter magnitude as a function (systems 6 and 9 in Table VI are examples of these PSA's) of observation angle. These systems are usually designed with an eye toward minimizing the ratio dependence on index-of-refraction. A primary difficulty with these devices is that the response functions for the scattered light ratio are often not monotonic. Additional measurement ratios at other angles are then required for unique specification of particle size. If the physical characteristics of the particles measured with this technique do not satisfy the assumptions used to compute the scattered intensity ratio then serious errors can be made using such PSA's.

The particle sizing interferometer (PSI) PSA eliminates many of the problems associated with the above systems, but has its own peculiar limitations. As with the other PSA systems, the PSI must assume a particle shape in order to achieve an estimate of the particle size. If the particle shape is irregular then the PSI measurement must be interpreted as being proportional to the Fourier transform of the particle's cross-sectional area. Because this PSA does not draw the aerosol down a tube before it passes through

the illuminating beam, PSI size distribution data must be analyzed using weighting factors which normalize the particle size increments measured with the device to a common volume and thereby account for the possibility of larger particles scattering from a larger volume than small particles.

Practically any optical system used in an SRM plume will need to make similar data adjustments.

We now consider particle characteristics which can affect the operation of optical PSA systems.

4.1.2 Particle Characteristics Affecting PSA Performance

Lorenz-Mie scattering theory has been found to be a rigorously correct solution to the problem of light scattered by homogeneous spherical particles of any size relative to the wavelength incident on the particle. PSA systems which obtain a measurement that must be correlated with this theory must be used under the assumption that the particles being measured satisfy these theoretical assumptions. In certain special cases when the particles are not spherical or homogeneous, the theory can still be used to predict the scatter properties of the particles, and the PSA can be used to obtain a size estimate. This size estimate must itself be defined since an irregularly shaped particle does not have a unique dimension. It has some average dimension that exists either by analytical definition or PSA response to that particle shape. Hence, two particle characteristics which can cause

uncertainty in the size measurement are 1) shape and 2) composition. A further difficulty arises in SRM plume application where the index-of-refraction of the gases surrounding the particle may be highly variable. Even when the particles can be assumed to be spherical, electrostatic attraction can make the particles agglomerate if they are solids or grow to unexpected sizes if they are liquids. Also, the probability may be large that the particles have non-uniform composition due to the chemistry involved in their formation.

The magnitude of the particle sizes observed with a PSA represents a potential source of numerous PSA measurement uncertainties. In the case of particles less than about 2- μm in diameter, small changes in particle size can correspond to large changes in scatter magnitude. As the results in Chapter 3 show, S/N will be strongly size dependent. This places stringent requirements on photodetector linearity and electronic amplifier response in the signal processing electronics and in the design of optical systems used to illuminate the particle and collect the scattered light. Care must be given, for example, in systems 3-9 listed in Table VII to design the PSA so the system can distinguish between large particles passing near the edge of the illuminating beam where the incident intensity is low and small ones passing near the center where the intensity is high. In the case of systems 3,4,5,7, and 9 in Table VII,

this is accomplished by sampling the aerosol with a tube that sucks the particles into a small air stream blown across the illumination beam. Systems 6 and 8 optically aperture the illuminating beam, while system 10 requires that the scattered light signal possess certain preset logic constraints before it is accepted for measurement. Sampling biases related to particle characteristics may occur in a PSA because a sampling tube is used to withdraw the obscurant from its environment. These biases result from 1) the flow in the sampling tube separating particles by aerodynamic size (in much the same way as a cascade impactor) such that the large sizes are driven to the tube walls and rarely reach the illuminating beam, 2) breaking up agglomerate particles and liquid drops, and 3) increasing the evaporation rate of liquid particles or causing the particles to cool at rates over what might otherwise be encountered in the SRM plume. There is also the more mundane problem of chemically active particles reacting with the sampling line and generating either a different source and kind of particle or corroding the sampling tube.

The alternative to sampling tube is optical aperturing and signal processor logic. With these design constraints, weighting factors are developed around scattering theory models which may be questionable when either particle number density is high or non-spherical particle shapes are measured.

Particle number density can seriously affect PSA performance. When number densities are too high those PSA systems which depend on optical aperturing to define the sampling region become very inefficient in sample acquisition and as Section 3.2 showed the probability of simultaneously measuring two or more particles as a single particle can become significant. Those PSA's which utilize sampling tubes (and thus would be difficult or impossible to use except at the edge of the plumes) usually have mechanical devices which dilute the sample input to a manageable value. However, when number densities reach values of the order of $10^6/\text{cc}$, the dilution mechanism usually saturates and the same number density is always measured.

Of fundamental importance to all PSA systems if accurate measurements are to be obtained are accurate and reliable calibration standards. These are considered in Section 4.2.

4.2 PSA CALIBRATION TECHNIQUES AND STANDARDS

Because there is no universally accepted particle sizing standard against which to calibrate PSA systems, a number of different techniques and standards have been proposed and used. We briefly consider some of the better known of these.

One of the most commonly used calibration standards is latex or polystyrene spheres. These spheres are usually batch sampled and measured with electron microscope. When they are purchased, a specified mean particle diameter and

standard deviation are provided. These spheres are remarkably uniform in size. However, they are provided in a water solution. A small drop containing millions of these particles must be diluted in methanol. The methanol solution is then atomized and evaporates, presumably leaving a single particle. Care must be used to neutralize any static charge on the spheres, thereby preventing agglomeration. Furthermore, the particles must travel a sufficient distance from the atomizer to be certain that all the methanol evaporates and does not contribute particles for PSA measurement.

Another popular source of calibration particles is the vibrating orifice monodisperse particle generator. This device vibrates an orifice at a precise frequency to break a liquid stream up into droplets. In typical operation this device can cover a size range from about 1 micrometer to slightly greater than 1 millimeter with an uncertainty in particle size of about 1% when vibration frequency and orifice size are accurately known. Chemical salts can be mixed with the fluid forced through the orifice. After droplet formation the fluid is allowed to evaporate leaving a crystalline solid near the size of the original droplet. The primary uncertainty associated with this device results from evaporation after the droplets are formed.

The alternative to using calibrated particles in PSA calibration is to use some standard instrument to measure the same particle set measured with the PSA. One common

approach is to use some type of microscope. The uncertainty using this method results from the fact that the particles must somehow be mechanically captured and preserved for examination. Furthermore, measurement of particle size via microscope techniques may be uncertain by as much as 5-10% due to image edge definition and uncertainty in magnification values. Unless some electronic means (and these exist) is used to measure the particle images, relatively few particles (compared to the PSA) can be measured for any one sample because of the time involved.

An alternative to samples mechanically obtained and examined microscopically is either holography or a laser shadowgraph method. Holographic methods use laser technology to obtain a three dimensional image of a relatively large volume of particles. Typical holographic exposure times are of the order of 10^{-8} seconds. Hence, the particle holograms are essentially instantaneous volumetric records. Should the particles change with time, numerous holograms are required to provide sufficient measurements for good time averages.

Electronic means of analyzing the holographic image is even more necessary than examining mechanical samples with a microscope because many additional particles must be measured. Typically, holographic images can be measured over depths-of-field about 100 times greater than could be achieved photographically or with a microscope and with about the same

resolution.

Laser shadowgraph methods obtain particle size measurements by using a pulsed laser to illuminate the particles and a microscope optical system fitted with an image videocountube to obtain image information. The particle shadows may be recorded on video tape and either examined on line or analyzed at leisure as with holography. This device has about the same depth-of-field limitations as a regular microscope which requires that a particle stream be blown in a very narrow stream through the field of view if most of the particle shadows are to be accurate representations of the particle cross-sections. This device also requires electronic imagery analysis if large numbers of particles are to be measured.

A calibration instrument particularly appealing for calibration of PSI systems uses a sinusoidally driven acoustic source to generate a well defined periodic flow field. Particle velocity can then be related to particle cross-sectional area and density through Stokes law. Since the PSI very accurately measures particle velocity it could be calibrated in this fashion. The difficulty with this method is that an equivalent "aerodynamic" particle diameter (derived from the particle cross-sectional area and density) is determined from a velocity measurement and is not a true physical dimension.

4.2.1 Quantitative PSA Tests

After calibration techniques and standards are defined or developed for PSA calibration, then quantitative measures of performance can be applied. A number of stated and implied measures of this kind exist in the literature. Here we list some which appear to have significant merit in specifying PSA performance.

4.2.1.1 Size Accuracy and Resolution

A fundamental question which is always asked concerning a PSA is "how accurately can it measure particle size?" The answer is not simple and has at least two parts. First, it is probably not safe to assume that size uncertainty is constant across the full size range of the PSA. The instrument will most likely measure particles with much greater accuracy for the large particles of its size range than for the small particle and thus a calibration must determine not only how accurately the PSA measures a given size but also the spread (or precision) in values at that size. The second portion of the answer depends on the size range of the instrument. If the size range is significantly greater than that of the PSA, then the mean size measured by the PSA will be in error. Hence, measurement of polydispersions must always be accomplished with sufficient instrument range if accurate answers are to be achieved.

4.2.1.2 Number Density and Accuracy

A companion measurement with particle size is number density. Number density always appears as one of the variables in the determination of turbidity which with dosage concentration is used to determine the extinction coefficient. It can be expected that the accuracy and precision with which number density can be estimated will be a function of number density, sampling techniques, size range of the particles being measured, and the kinds of particles being measured. Therefore, PSA specification of number density may require calibrations which reflect a reference to all these parameters.

4.2.1.3 Operational Uncertainty Specification

Even with specification of a PSA's accuracy and precision over the full size and number density range of the particles of interest, the question of effectively using PSA data in SRM plume modeling and characterization still remains. To establish operational boundaries for PSA systems, two additional tests might be applied which should aid in further validating previous calibration. First, the PSA would be required to measure a known polydispersion consisting of a number of well known mode sizes with a specific or relative number density associated with each mode size. The accuracy with which the PSA could identify the mode sizes and number densities would then give some measure of confidence with which it could be applied to unknown polydispersions. In

the second test, the particles would be uniformly dispersed in a controlled environment through which transmissometer measurements were made. The PSA would be required to measure particle size distribution and number density. These data along with the scattering gain for the particles would then be used to predict the transmission obtained during the test. Comparison of the experimentally determined transmission and PSA computed transmission should lend a quantitative estimate of the uncertainty in the extinction coefficient as estimated from laboratory and field measurements.

4.3 PROPOSED SYSTEMS FOR DEVELOPMENT

This study has concentrated on the optical measurement of particle velocity and size. In this section we point out some techniques and methods which have been proposed for measuring particle temperatures, submicron sizes, and mass.

4.3.1 Particle Diffusion Spectroscopy

Particle diffusion spectroscopy was described for a laser homodyne signal as early as 1967.¹⁵ Additional work since then has suggested that the method might be applied to flames and perhaps, ultimately, to such hostile environments as SRM plumes.¹⁶⁻¹⁸ Basically these studies show that the homodyne power spectrum scattered of light which is Lorentizian in halfwidth is proportion to the diffusion coefficient D_c for particles undergoing Brownian motion.

D_c is given by

$$D_c = \zeta T / \mu' d_p$$

where T is the fluid temperature, μ' the viscosity, and d_p particle diameter and ζ a proportionality constant. Hence, if temperature and viscosity of the surrounding gas are known, the half-width of the homodyne spectrum will be proportional to mean particle size. Dunning found in his studies that the half-width was essentially independent of the shape of the size distribution. Hence, the "mean" particle size remains to be clearly defined since the shape of the size distribution is not detected.

Penner has estimated that the minimum residence time for particles in the beam used to illuminate them should be of the order of 10 microseconds. For particles traveling at 500m/sec this would require a 0.5 cm diameter incident beam. In this case temperature and density fluctuations along the beam path may make the methods unusable except near the edges of the plume. Dunning, in his studies concerning liquids, concluded that entropy fluctuations could contribute to the half-width of the power spectrum which needs to be included in models if used in SRM plumes.

Finally we point out that a computation of the diffusion coefficient requires a knowledge of the viscosity of the medium surrounding the particles. Virtually no such data exist for SRM type flows, or for gases at temperatures greater than

about 10^3 °K. Thus, this uncertainty must be taken as a current fundamental limitation in the application of this technique to SRM plumes.

4.3.2 Schlieren Correlation

In 1974 Rudd described a correlation technique which could be used in SRM plume velocity measurements. Rudd showed that a fluid containing turbulence will produce shadows in a collimated beam passing through the turbulence and incident on a detector some distance away. By placing a transmission grating in the beam at the detector, as shown in Fig. 24, a signal can be generated with a correlogram showing a frequency v_c given by

$$v_c = 2\pi/v_0$$

where v_0 is the spatial period of the grating. The resulting velocity is the convection speed of the turbulence and in an SRM plume can be expected to represent the mean gas velocity in the plume. The power of this technique resides in the fact that the optical system is simple and a parameter proportional to gas velocity, not particle velocity, is measured.

A primary drawback to using this type of system is the poor spatial resolution. A modified version of the Rudd system whereby a correlation between two crossed beams could be effective in increasing the spatial resolution is shown in Fig. 25. In this scheme correlation is performed only on

simultaneous outputs from the two photodetectors for each beam thereby localizing the measurement. The significance of this system relative to particles in an SRM plume follows from the fact that if an independent measurement of gas velocity can be obtained, then particle size can be estimated from the difference in gas and particle velocity (see Section 3.2.1.3).

4.3.3 Radiating Particle Velocimeter

The velocimeter systems discussed thus far utilize a laser to illuminate the particles being measured. A system developed at AEDC for the measurement of large particles ($D \sim 100 \mu\text{m}$) in high enthalpy flows makes use of the fact that such particles are self luminous. By properly aperturing a scattered light detection system, the speed of such particles can be measured. The apertures consist of two photodetectors placed a fixed distance apart in the image plane of the light collection lens. Correlation of the pulse separation times from the photodetectors in much the same manner as for the transit time LV yields the mean time-of-flight for the particles. By calibrating the photodetectors with a blackbody reference, particle temperature can be extracted from a signal magnitude. Particles of interest in SRM plumes are considerably smaller than those examined in the AEDC work. However, the potential application of this method to SRM plumes is not precluded by any known major limitation.

4.4 SUMMARY OF CURRENTLY KNOWN INSTRUMENTATION FOR PARTICLE PARAMETER MEASUREMENTS

Table IX presents a summary of the optical instrumentation which has been considered either in this report or in recently published work. In none of the applications listed can it be said that the measurement is a routine one when the application is an SRM plume. Certain systems listed are in their initial stages of development and cannot be expected to produce data in the near future. These systems have either been applied to SRM plumes or are sufficiently well understood in that their application is possible in the near term. Those devices listed but not discussed in this report are described in detail in the listed references.

TABLE I

POSSIBLE SYSTEM VALUES FOR
A FRINGE TYPE LV SYSTEM

PARAMETER	NOMINAL SYSTEM VALUE	OPTIMUM SYSTEM VALUE
N	11	6
F	8	4
v_p	$5 \cdot 10^7 \text{ Hz}$	10^8 Hz
κ	0.5	0.2
λc	$0.488 \cdot 10^{-6} \cdot 0.10 \text{ m}$	$0.488 \cdot 10^{-6} \cdot 0.23 \text{ m}$
P_o	1	5
$\Delta \lambda$	10^{-9} m	$3 \cdot 10^{-11} \text{ m}$
S/N	100	10
hc	$1.98 \cdot 10^{-25} \text{ joule-m}$	$1.98 \cdot 10^{-25} \text{ joule-m}$
v	1	1

TABLE II

POSSIBLE SYSTEM VALUES
FOR A TRANSIT TYPE LV SYSTEM

PARAMETER	NOMINAL SYSTEM VALUE	OPTIMUM SYSTEM VALUE
N	1	1
F	8	4
v_p	$2 \cdot 10^7 \text{ Hz}$	10^8 Hz
κ	1	1
$\lambda\epsilon$	$0.488 \cdot 10^{-6} \cdot 0.10 \text{ m}$	$0.488 \cdot 10^{-6} \cdot 0.23 \text{ m}$
P_o	1	2.5
$\Delta\lambda$	10^{-9} m	$3 \cdot 10^{-11} \text{ m}$
S/N	10	1
v	1	1

TABLE III

OPTIMUM PSI PARAMETERS
FOR MEASUREMENTS IN SRM PLUMES

PARAMETER	SYSTEM I	SYSTEM II
N	11	6
F	4	4
v_p	$5 \cdot 10^6 \text{ Hz}$	10^7 Hz
κ	0.2	0.2
$\lambda\epsilon$	$0.488 \cdot 10^{-6} \cdot 0.23 \text{ m}$	$0.488 \cdot 10^{-6} \cdot 0.23 \text{ m}$
P _o	5	5
$\Delta\lambda$	$3 \cdot 10^{-11} \text{ m}$	$3 \cdot 10^{-11} \text{ m}$
S/N	10	10

TABLE IV

PARAMETRIC VALUES FOR LOCAL OSCILLATOR
LV SYSTEM APPLICATION TO SRM PLUMES

PARAMETER	NOMINAL SYSTEM VALUE	OPTIMUM SYSTEM VALUE
N	$10^{(1)}$	$10^{(1)}$
ν_p	$5 \cdot 10^7^{(1)}$	$5 \cdot 10^7^{(2)}$
λ	$0.488 \cdot 10^{-6}$	$0.488 \cdot 10^{-6}$
ϵ	0.1	0.23
P_o	1	5
S/N	$10^{(2)}$	$1^{(2)}$

NOTE: (1) It can be shown that a local oscillator LV has an uncertainty in the frequency spectrum it measures which is proportional to $1/N$. Hence, while N could be chosen smaller, the uncertainty in the measured frequency would increase.

(2) It is assumed that a frequency tracker is used as a signal processor. Studies have shown that wide bandwidth tracker such as are commercially available can function with an inherently smaller S/N than typical burst processors.

TABLE V

PARAMETER	LV SYSTEM OR SRM PLUME VALUE
λ	$0.488 \cdot 10^{-6}$ m
ω_p	$5 \cdot 10^7$ Hz
$v_o(1)$	600 m/sec
r_o	0.2 m
μ	0.5
ρ_p (Al_2O_3)	3.96 gm/cc
N	11

NOTE: It is assumed for Figs. 13-15 that $\bar{v} = v_o$.

TABLE VI

COMPARISON OF PARTICLE SIZE AND NUMBER DENSITY
DATA FROM OPTICAL COUNTER, IMPACTOR, TRANSMISSION AND PSI

TEST NUMBER	MEASURED DIAMETER (Micrometers)	ρ_N ($\text{N/cm}^3 \cdot 10^{-4}$)	σ_g (Geometric Standard Deviation)
492	1) 0.46 2) 0.74 3) 0.76 4) 2.438	4.6 18 8.1 1.66	1.67 2.97 1.33
.463	1) 0.19 2) 3) 1.09 4) 2.035	1.3 2.1 0.26	2.1 1.26
493	1) 0.51 2) 0.74 3) 0.77 4) 0.75	4.3 19.0 10.7 15.6	1.68 2.45 2.15
471	1) 0.66 2) 0.35 3) 1.02 4) 0.515	4.6 140 2.8 514	1.57 1.58 2.29

Legend: 1) Optical Counter
 2) Cascade Impactor
 3) Extinction Measurement
 4) PSI (Geometric Mean Diameter)

TABLE VII

 PARTICLE SIZING INSTRUMENTS AND TECHNIQUES
 OPTICAL SYSTEMS

INSTRUMENT	PRINCIPLE OF OPERATION	MANUFACTURER OR REFERENCE	MEASURED PARAMETER	RANGE OF MEASURED PARAMETERS
1. MICROSCOPIC METHODS (INCLUDING PHOTOGRAPHY AND HОLOGRAPHY)	MEASUREMENT OF IMAGE CROSS SECTION WITH A CALIBRATED RETICLE	NUMEROUS, e.g. BAUSCH & LOMB, AMERICAN OPTICAL, DRI, IDMA & APOLLO LASERS	IMAGE SIZE AND SHAPE	SIZE $\geq 0.5 \mu\text{m}$
2. TRANSMISSOMETER	MEASUREMENT OF RELATIVE BEAM ATTENUATION FOR SINGLE OR MULTIPLE WAVE- LENGTHS	KERNER	TURBIDITY (NUMBER DENSITY X EXTINCTION CROSS SECTION)	0.1 - 4.6 ATTENUATION LENGTHS FOR 1% INTENSITY UNCERTAINTY
3. OPTICAL PARTICLE COUNTER	MEASUREMENT OF SIGNAL PULSE HEIGHT FROM ILLUMINATED PARTICLES	CLIMET (MODEL CI-201) ROTCO (MODEL 245) BAUSCH & LOMB (MODEL 40-1)	FORWARD SCATTER CROSS SECTION	NUMBER DENSITY 0 - 400/cc "PARTICLE SIZE" RANGE $0.3 - 100 \mu\text{m}$
4. OPTICAL PARTICLE COUNTER	MEASUREMENT OF SIGNAL PULSE HEIGHT FROM ILLUMINATED PARTICLES	ROXCO (MODEL 220)	90° SCATTER CROSS SECTION	NUMBER DENSITY 0 - 20/cc "PARTICLE SIZE" RANGE $0.5 - 6.5 \mu\text{m}$
5. OPTICAL PARTICLE COUNTER	MEASUREMENT OF SIGNAL PULSE HEIGHT FROM ILLUMINATED PARTICLE	PMS (MODEL ASAS)	INFRACAVITY LASER EXTINCTION COEFFICIENT	NUMBER DENSITY (NOT GIVES); PROB 10 ⁻² /cc "PARTICLE SIZE" RANGE TO 0.05 μm
6. OPTICAL PARTICLE COUNTER	MEASUREMENT OF RATIO SIGNAL MAGNITUDE AT TWO FORWARD ANGLES	EEG (MODEL, PILLS IV) (SINGLE PARTICLES) LEEDS & NORTHUP (MULTIPLE PARTICLES)	RATIO OF FORWARD SCATTER CROSS SECTIONS AT TWO DIFFERENT ANGLES	NUMBER DENSITY 10 ³ - 10 ⁶ /cc "PARTICLE SIZE" RANGE 0.3 - 3 μm NUMBER DENSITY 10 - 10 ³ /cc "PARTICLE SIZE" RANGE $\geq 1 \mu\text{m}$
7. INTEGRATING SEPHELONOMETER	MEASUREMENT OF LIGHT SCATTERED FROM A VOLUME OVER NEARLY 4 π STERADIANS	MRI	VOLUME SCATTERING COEFFICIENT, b, AS A FUNCTION OF TIME	$b = 10^{-5} - 10^{-2} \text{ cm}^{-1} \text{ sec}^{-1}$ EQUIVALENT MASS LEADING 0.3 - 10 ⁻³
8. PARTICLE SHADOW SPECTROMETER	MEASURE PARTICLE SHADOW SIZE WITH A LINEAR PHOTO- DETECTOR ARRAY	PMS	PARTICLE SHADOW DIMENSION	"PARTICLE SIZE" $\geq 5 \mu\text{m}$ WITH CALIBRATION; NUMBER DENSITY: $\leq 10^{-3}/\text{cc}$
9. PARTICLE GRANULOMETER	MEASUREMENT OF ENERGY IN AN ANNULAR SECTION OF A DIFFRACTION PATTERN	CORNELL ALIANT	MEAN DIFFRACTION PATTERN SIZE	"PARTICLE SIZE" $\geq 5 - 100 \mu\text{m}$
10. PARTICLE SIZING INTERFEROMETER	MEASUREMENT OF SIGNAL SHAPE FROM LIGHT SCATTERED FROM INTERFERENCE PATTERNS	UNSI, SOL, AND	SIGNAL VISIBILITY	NUMBER DENSITY TO 10 ⁶ /cc "PARTICLE SIZE" $\geq 0.3 \mu\text{m}$

TABLE VIII

PARTICLE SIZING INSTRUMENTS AND TECHNIQUES
INERTIAL METHODS

INSTRUMENT	PRINCIPLE OF OPERATION	MANUFACTURER OR REFERENCE	MEASURED PARAMETER	RANGE OF MEASURED PARAMETERS
1. CASCADE IMPACTOR (BUWIS, ANDERSEN, ETC.)	MEASUREMENT OF AERODYNAMIC INERTIA	MONSANTO, 2001 INC. BCL. ENVIRONMENTAL RES. CORP., CLAESCO GCA CORP.	INERTIAL MASS FOR GIVEN AIR FLOW	.02 - 10 gm/sec 0.3 - 20 gm/sec (0.1 - 10) 10 ⁻⁶ gm/cm ³ 1 MIN. TIME RESOLUTION
	METHODS OF MASS DETECTION <ul style="list-style-type: none"> • FACIAL WEIGHT • BETA RAY ATTENUATION • CHANGE IN FREQUENCY OF PIEZOELECTRIC CRYSTAL • ROTATING DRUM WITH 4 STAGES 			
2. SERIES CYCLONE	3 CYCLONES IN SERIES WITH DIFFERENT CUT POINT FOR AERODYNAMIC INERTIA	SOUTHERN RES. INST.	SEPARATED MASS	0.1 - 25 gm/m ³
3. COPILOCATOR	PARTICLE IMPACTS ON CONTINUOUS COLLECTOR OR COVERED SLIDES	HRI, ET AL.	SIZE OF PARTICLE IMPACT CRATOR	PARTICLE SIZE: 10-300 μ m (GEL REPLICATION) 20-1000 μ m (FORMVAR REPLICATION)

VERY SMALL PARTICLE METHODS

1. CONDENSATION NUCLEI COUNTER	TRANSMISSION THROUGH A CLOUD CHAMBER AS A FUNCTION OF TEMPERATURE AND HUMIDITY	GE, ET AL.	RELATIVE TRANSMISSIVITY	"PARTICLE SIZE" RANGE: > 10 ^{-3.1} μ m
2. ELECTRIC MOBILITY ANALYZER	ELECTRICAL CHARGING AND MOBILITY ANALYSIS	WHITNEY & TSI	ELECTRICAL MOBILITY	"PARTICLE SIZE" RANGE: 0.007-1 μ m NUMBER DENSITY: > 10 ⁶ /cc

TABLE IX

INSTRUMENTATION FOR THE MEASUREMENT
OF PARTICLE PROPERTIES IN SRM PLUMES

PARTICLE SIZE	PARTICLE NUMBER DENSITY	PARTICLE MASS DENSITY	PARTICLE VELOCITY	PARTICLE TEMPERATURE
PSI	PSI/LV	*X-Ray Spectroscopy	LV	*Diffusion Correlation
MIE SCATTER	Mie Scatter	LV/Schlieren Corre- lation	• Dual Scatter	Spectroscopy
• Forward Scatter Ratio	Holography		• Transit	
• Radiation Shape			• Local	*Radiating Particle
• Scatter Magnitude	Transmissometer		Oscillator	Velocimeter
			Holography	
*Diffusion Correlation Spectroscopy				

*UNDER DEVELOPMENT

LIST OF FIGURES

1. Fringe LV Optical Geometry
2. Minimum Scatter Cross-Section for a Fringe Type LV System With Nominal System Parameters
3. Minimum Scatter Cross-Section for a Fringe LV System With Optimum System Parameters
4. Transit Time LV Optical Geometry
5. Minimum Scatter Cross-Section for a Transit Time LV System With Nominal System Parameters
6. Minimum Scatter Cross-Section for a Transit Time LV System With Optimum System Parameters
7. Minimum Scatter Cross-Section for PSI System I
8. Minimum Scatter Cross-Section for PSI System II
9. Local Oscillator LV System Optical Geometry
10. Minimum Scatter Cross-Section for a Local Oscillator LV System With Nominal System Parameters
11. Minimum Scatter Cross-Section for a Local Oscillator LV System With Optimum System Parameters
12. Geometry for Calculation of Spatial Distribution of Number Density
13. Number Density as a Function of \bar{D} and σ When Velocity is Inversely Proportional to Plume Radius R_p
14. Number Density as a Function of \bar{D} for a Radial Gaussian Velocity Distribution Across the Plume
15. Number Density as a Function of Radius for Constant Particle Size and a Radial Gaussian Velocity Distribution
16. $\Delta\phi$ as a Function of ϵ for an SRM Plume Shock
17. Z/ϵ as a Function of \bar{D} for Values of V_1 and η Used in Figure 16 (M = Mach No.)
18. Visualization of p , q and ϵ
19. A as a Function of γ With K as a Parameter

20. γ as a Function of K with A as a Parameter
21. Optimum A for Maximum Data Rate
22. PSI System Used for Data in Table I
- 23a. Index-of-Refraction vs. Amplitude for Dielectrics
- 23b. Index-of-Refraction vs. Amplitude for Metals
24. Schlieren Correlation System
25. Crossed Beam Schlieren Correlation System

REFERENCES AND FOOTNOTES

1. McGregor, W., "Some Problems With Gas/Particle Diagnostics in Solid Propellant Combustion," AIAA Paper 79-0084, presented at the 17th Aerospace Sciences Meeting, New Orleans, Louisiana, Jan. 15-17, 1979.
2. Gal, G. and Kirch, H., "Particulate Optical Properties in Rocket Plumes," AFRPL-TR-73-99.
3. Mann, D. M., McCay, T. D., Steinbrenner, E., and Danne, W. A., "Initial In-Situ Plume Property Measurements in a SRM Plume," presented at the 11th JANNAF Exhaust Plume Technology Meeting, Huntsville, AL, May 1979.
4. Farmer, W. M., Harwell, K. E., Hornkohl, J. O., and Schwartz, F. A., "Laser Particle Sizing Interferometer in Solid Propellant Exhaust Plumes," presented at the 11th JANNAF Exhaust Plume Technology Meeting, Huntsville, AL, May 1979.
5. Farmer, W. M., "Measurement of Particle Size, Number Density, and Velocity Using a Laser Interferometer," *Appl. Opt.* 11, p. 2603 (1972).
6. Siegman, A. E., "The Antenna Properties of Optical Heterodyne Receivers," *Proc. IEEE*, 54, 1350 (1966).
7. Farmer, W. M., "Analysis of Atmospheric Laser Doppler Velocimeters," *Appl. Opt.* 10, 2319 (1971).
8. Fuchs, N. A., The Mechanics of Aerosols, Pergamon Press, New York, (1964).
9. Liu, B. Y. H. (Editor), Fine Particles, Academic Press, New York (1976).
10. Brayton, D. B., and Goethert, W. H., "A New Dual Scatter Laser Doppler Shift Velocity Measuring Technique," *ISA Trans.* 10, 40 (1971).
11. Drain, L. E., "Coherent and Non-Coherent Methods in Doppler Optical Heat Velocity Measurement," *J. Phy. D.*, 5, 481 (1972).
12. Farmer, W. M., "Sample Space for Particle Size and Velocity Measuring Interferometers," *Appl. Opt.* 15, 1984 (1976).

13. Menzel, R., "Approximate Closed Form Solution to the Error Function," Am. J. Phys. 43 (1975).
14. Thorn, L. B., et.al., presented at the March 1979 JANNAF Propulsion Meeting in Anaheim, Ca.
15. Dunning, J. W., and Angus, J. C., "Application of Laser Homodyne Spectrometer to Particle Size Measurements," Chem. Eng. Science Div. Res. Rept. No. 10-04-67, Chem. Eng. Science Div., School of Engr. Case Western Reserve University, Cleveland, Oh.
16. Hinds, W., and Reist, R. C., "Aerosol Measurements by Laser Doppler Spectroscopy," Aerosol Science, 3, 501 (1972).
17. Penner, S. S., Bernard, J. M., and Jerskey, T., "Laser Scattering From Moving Polydisperse Particles in Flames, II, Preliminary Experiments," Acta Astronautica, 3, 93 (1976).
18. Driscoll, J. F., and Mann, D. M., "Submicron Particle Size Measurements in an Acetylene/Oxygen Flame," appearing in Laser Velocimetry and Particle Sizing, H. D. Thompson, and W. H. Stevenson, Editors, Hemisphere Publishing Corp., Washington, D. C. (1979).
19. Rudd, M. J., "Non-Doppler Methods of Laser Velocimetry," appearing in Proceedings of the 2nd International Work Shop on Laser Velocimetry, Purdue University, March 27-29, 1974, H. D. Thompson and W. H. Stevenson, Editors.
20. CPIA Solid Propellant Manual # 1025, August, 1964.

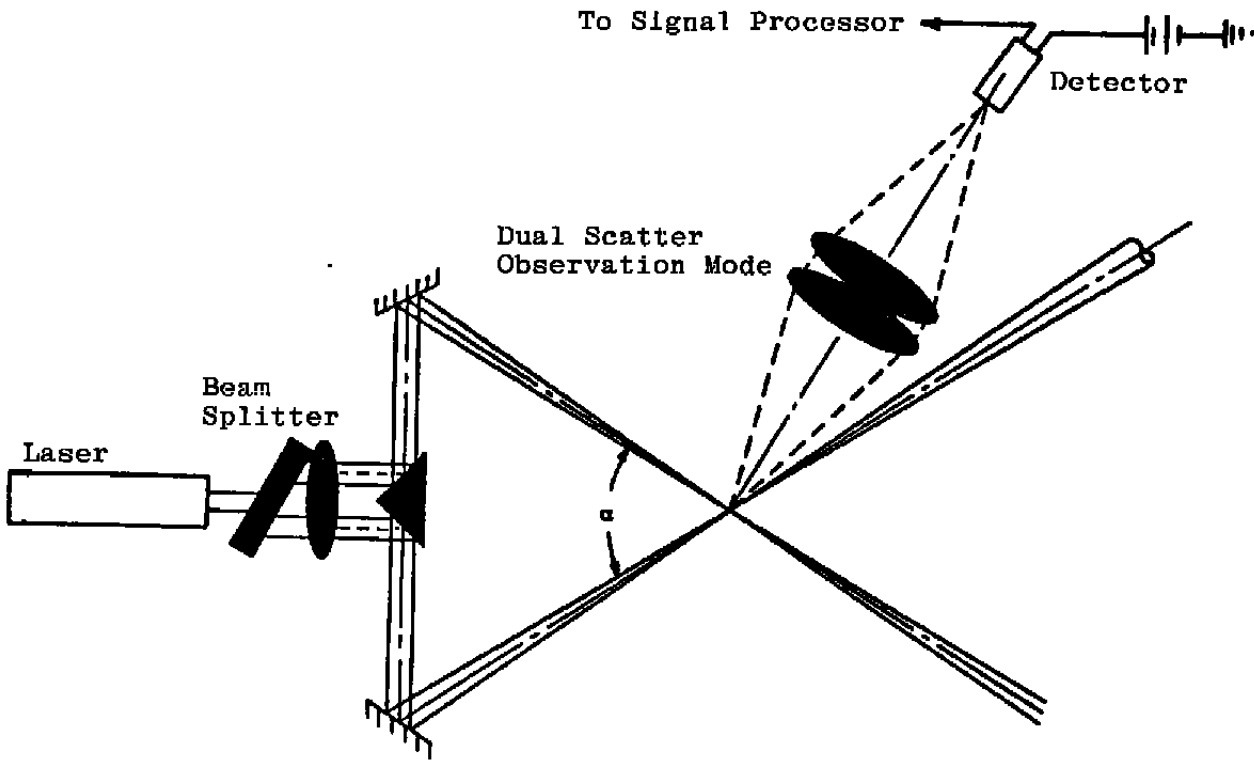


Figure 1. Fringe LV Optical Geometry.

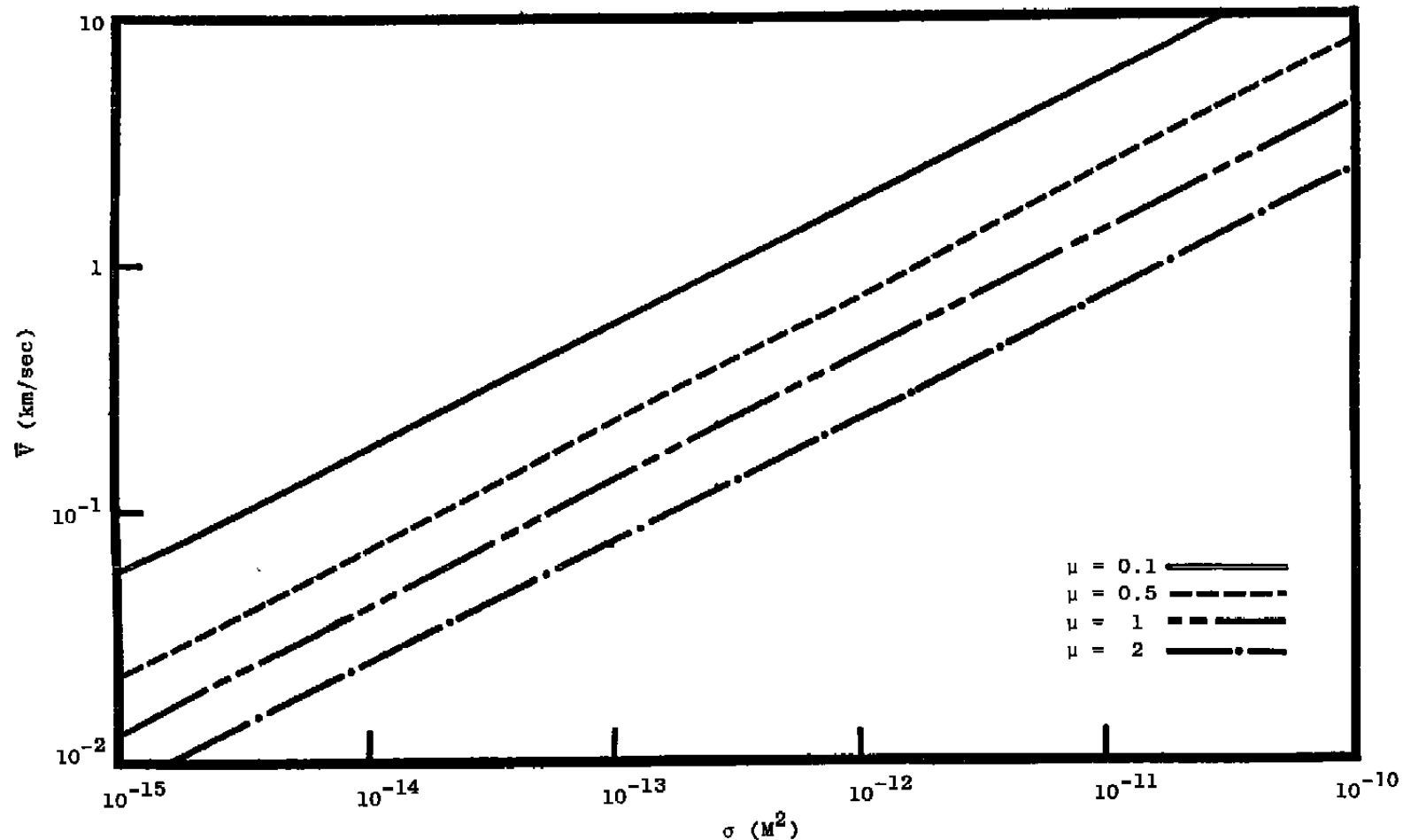


Figure 2. Minimum Scatter Cross-Section for a Fringe Type LV System with Nominal System Parameters.

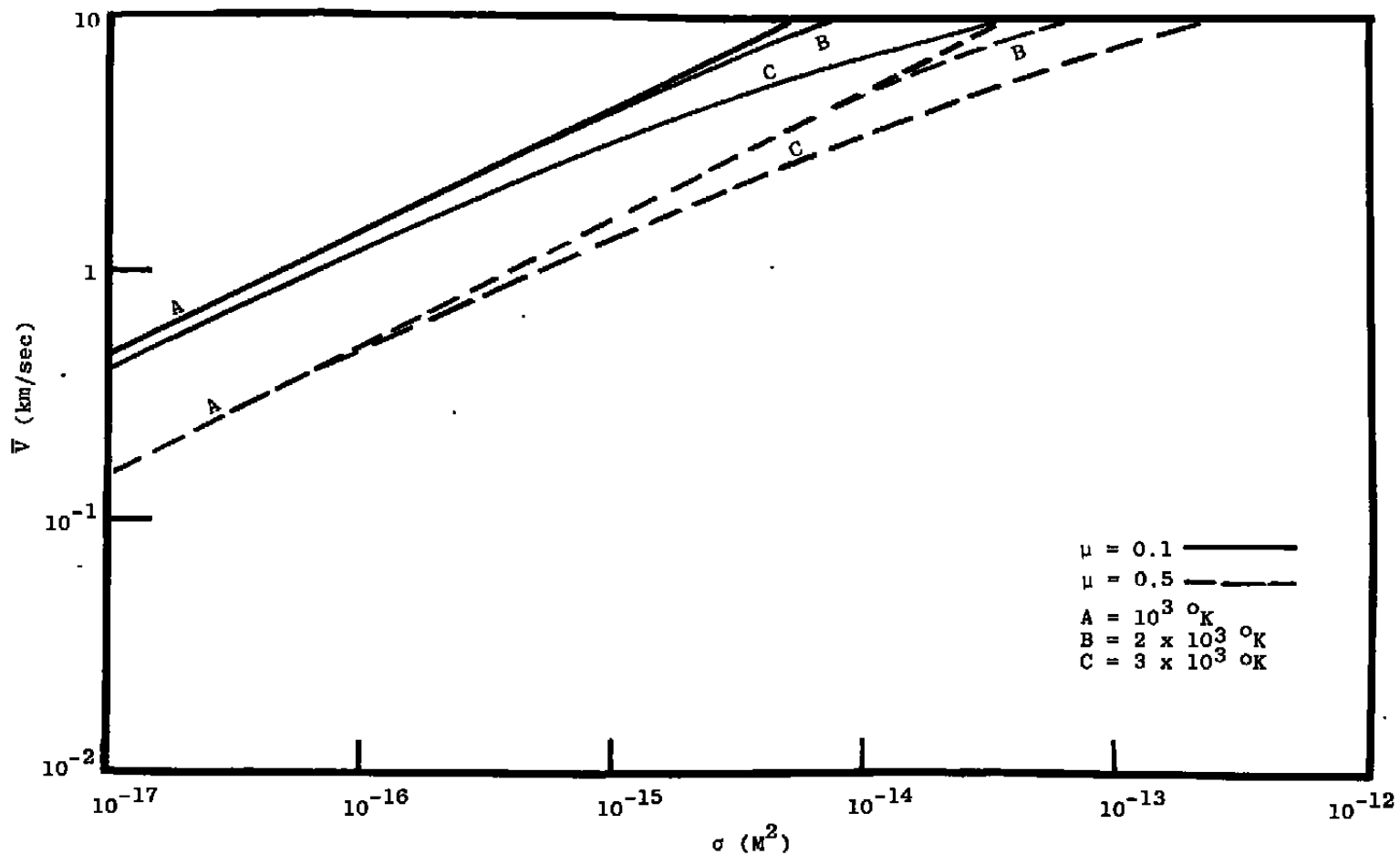


Figure 3. Minimum Scatter Cross-Section for a Fringe LV System with Optimum System Parameters.

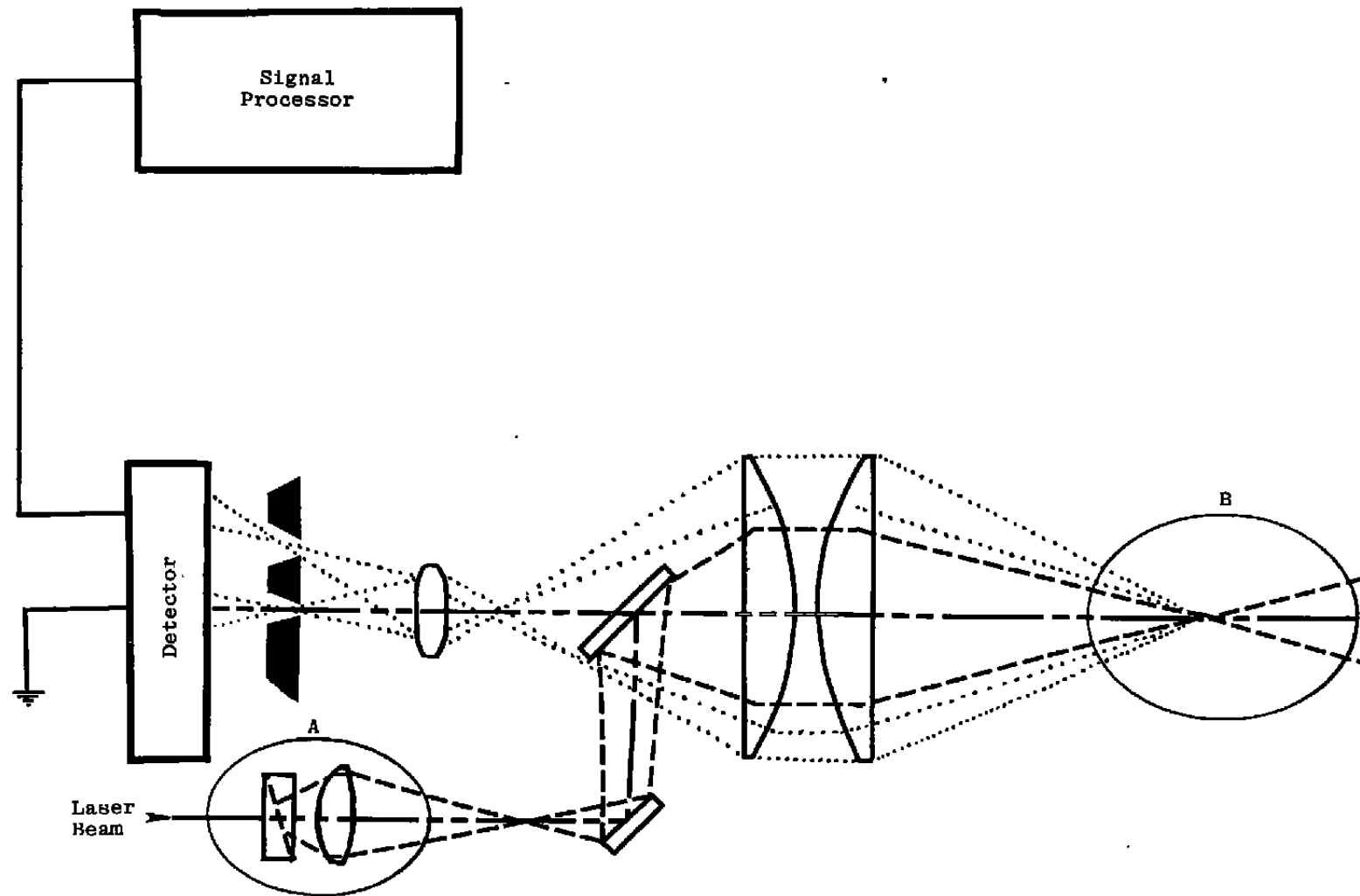


Figure 4. Transit Time LV Optical Geometry.

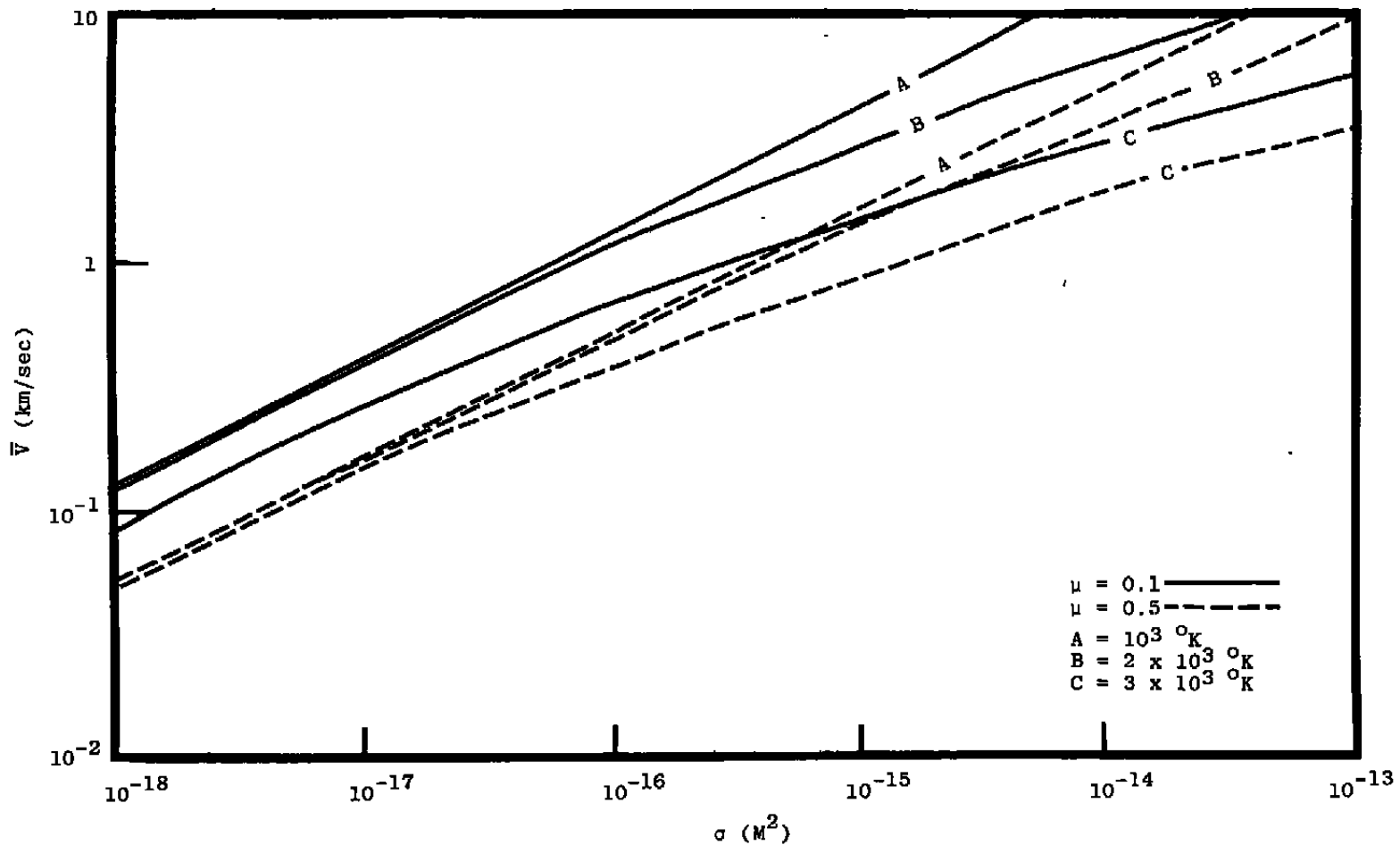


Figure 5. Minimum Scatter Cross-Section for a Transit Time LV System with Nominal System Parameters.

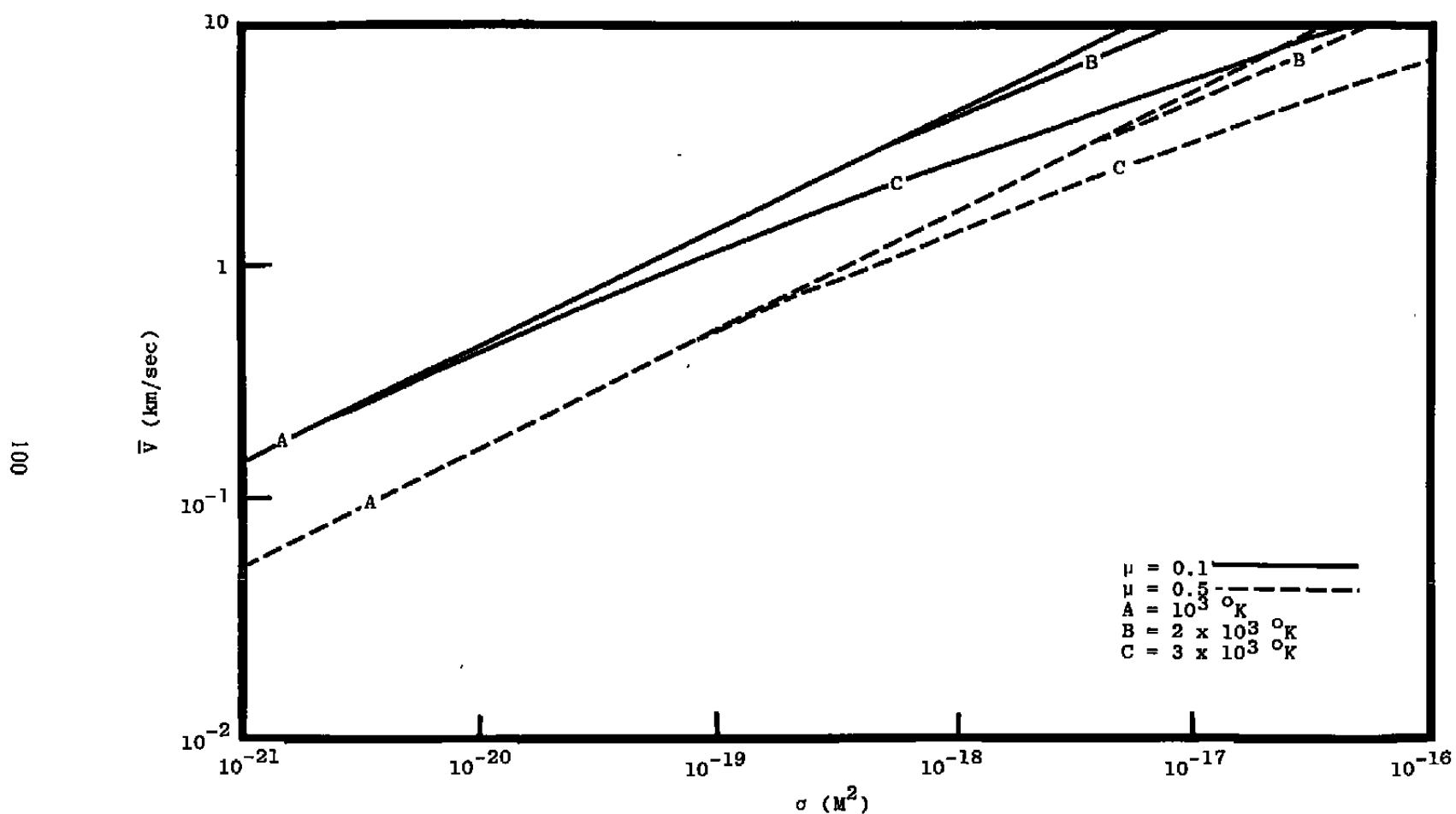


Figure 6. Minimum Scatter Cross-Section for a Transit Time LV System with Optimum System Parameters.

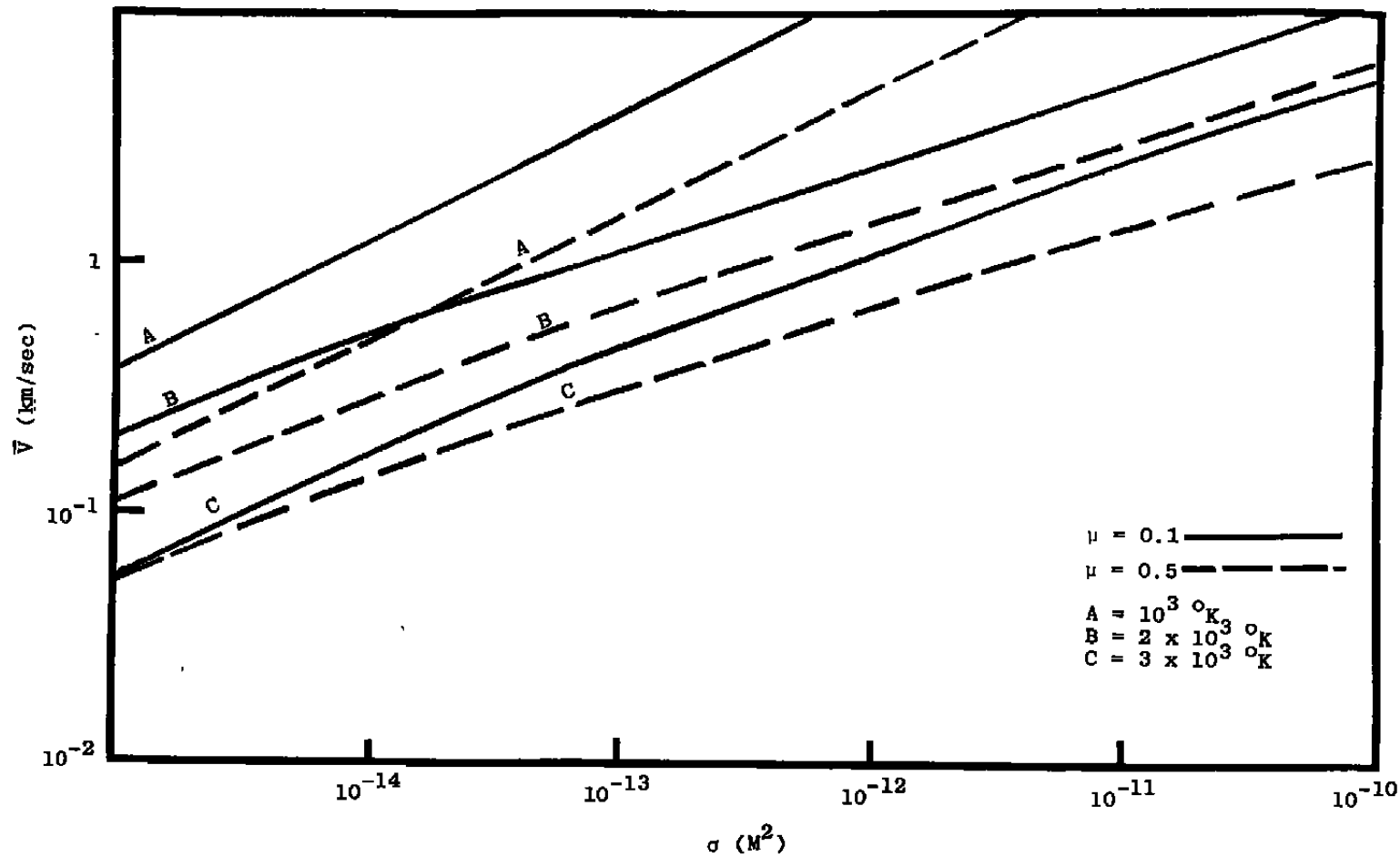


Figure 7. Minimum Scatter Cross-Section for PSI System I.

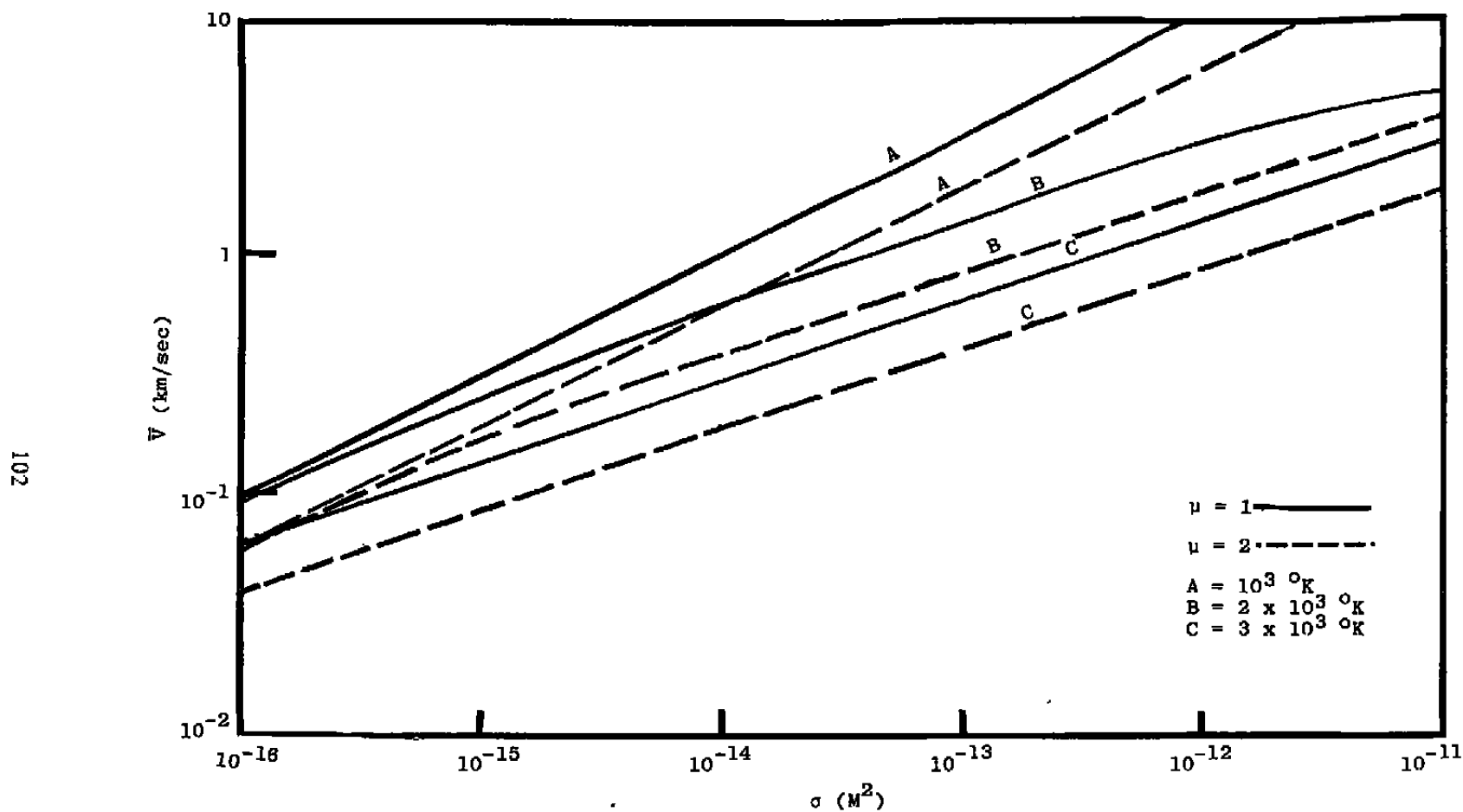


Figure 8. Minimum Scatter Cross-Section for PSI System II.

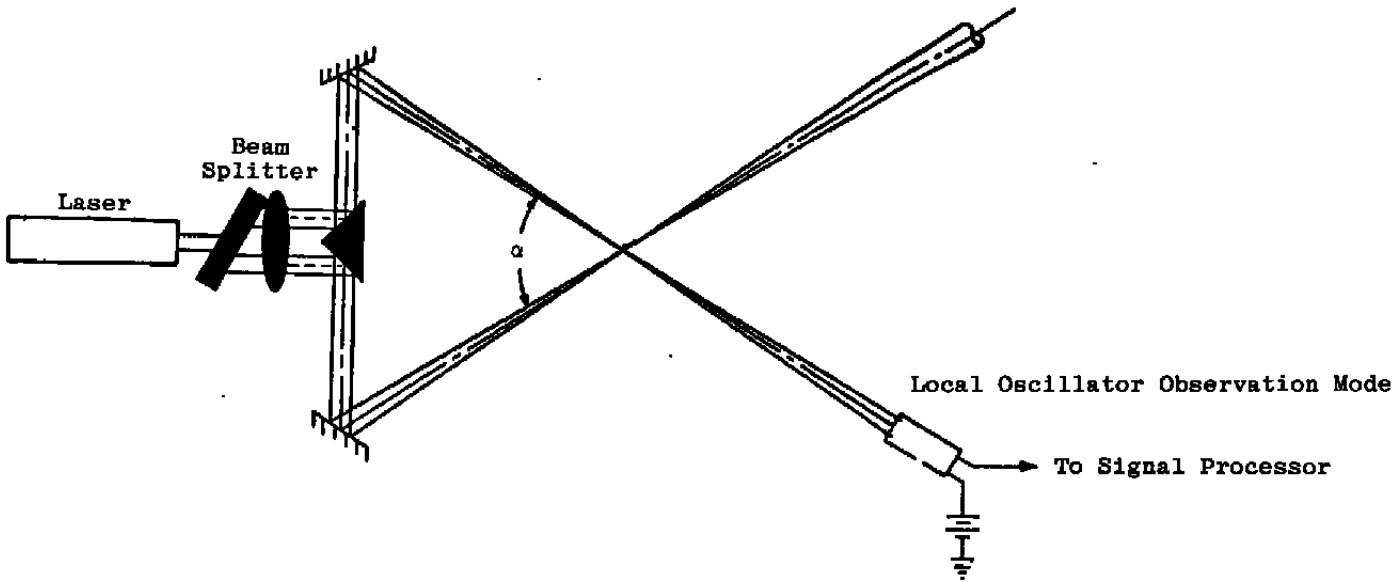


Figure 9. Local Oscillator LV System Optical Geometry.

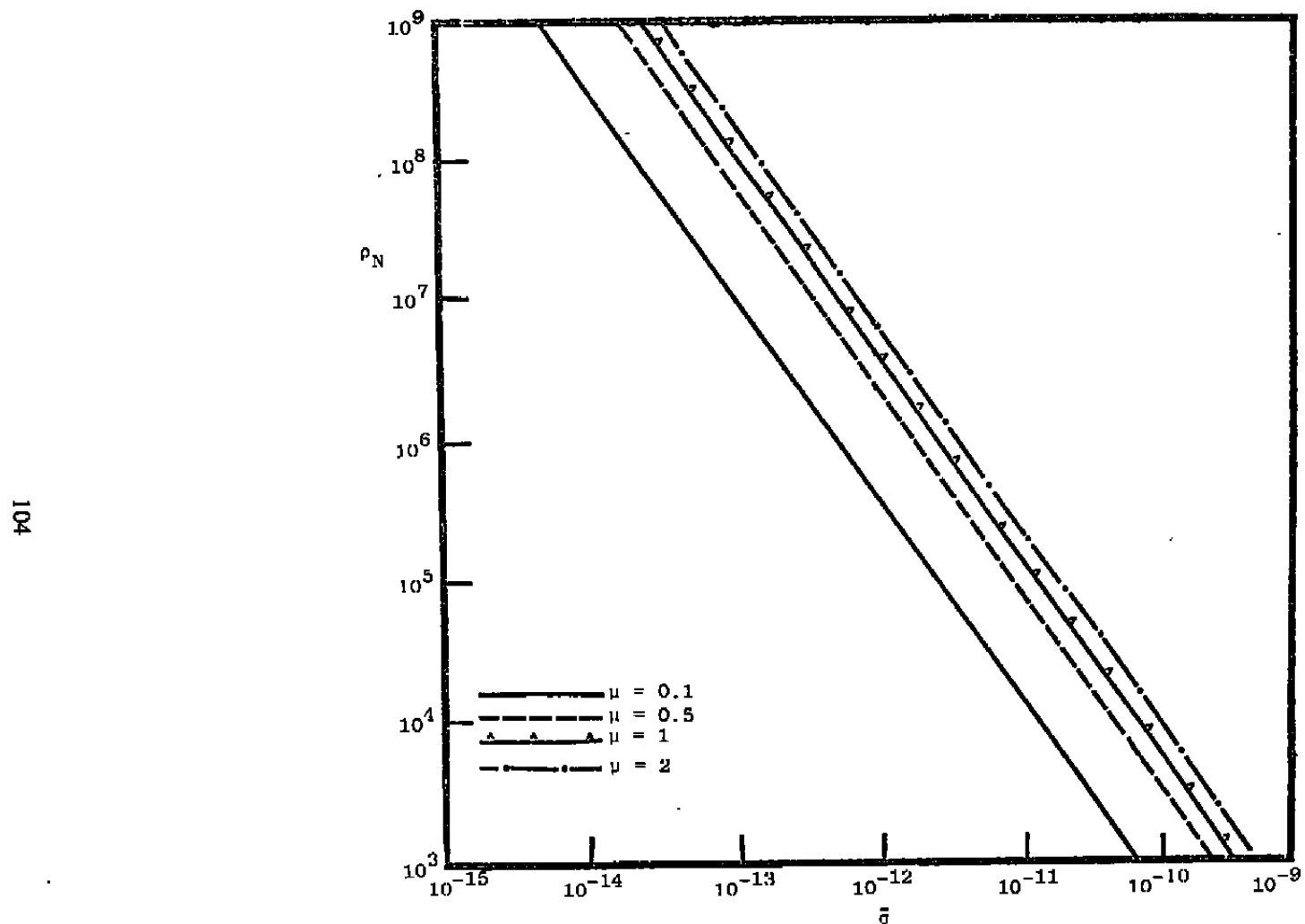


Figure 10. Minimum Scatter Cross-Section for a Local Oscillator LV System With Nominal System Parameters.

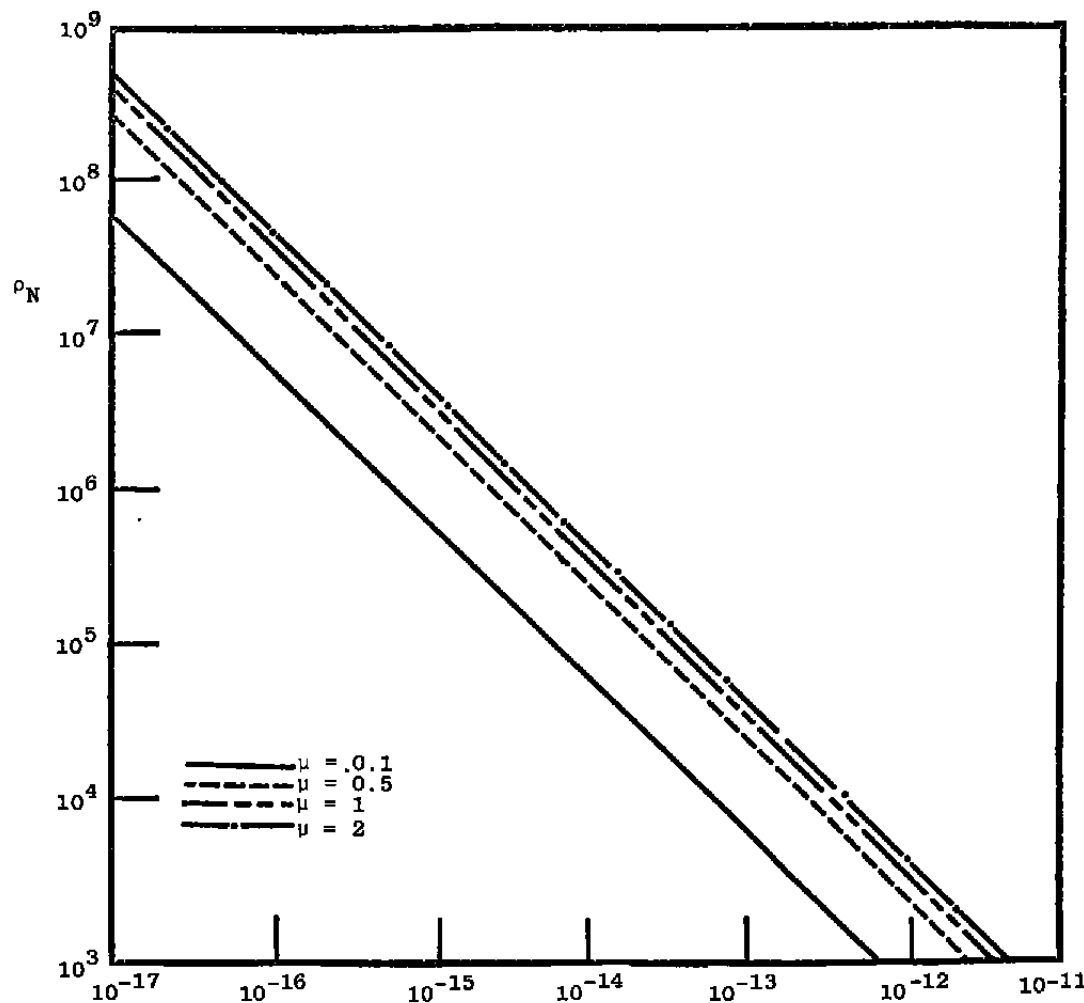


Figure 11. Minimum Scatter Cross-Section for a Local Oscillator LV System With Optimum System Parameters.

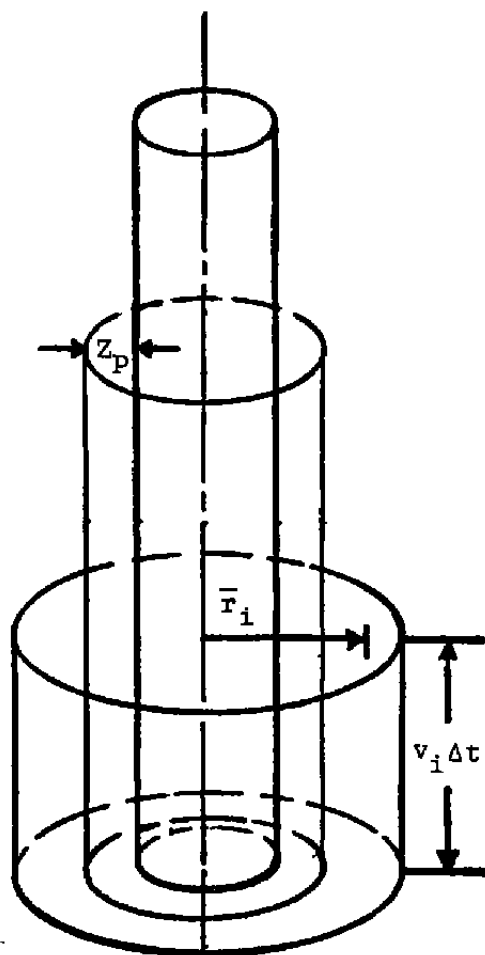


Figure 12. Geometry for Calculation of Spatial Distribution of Number Density.

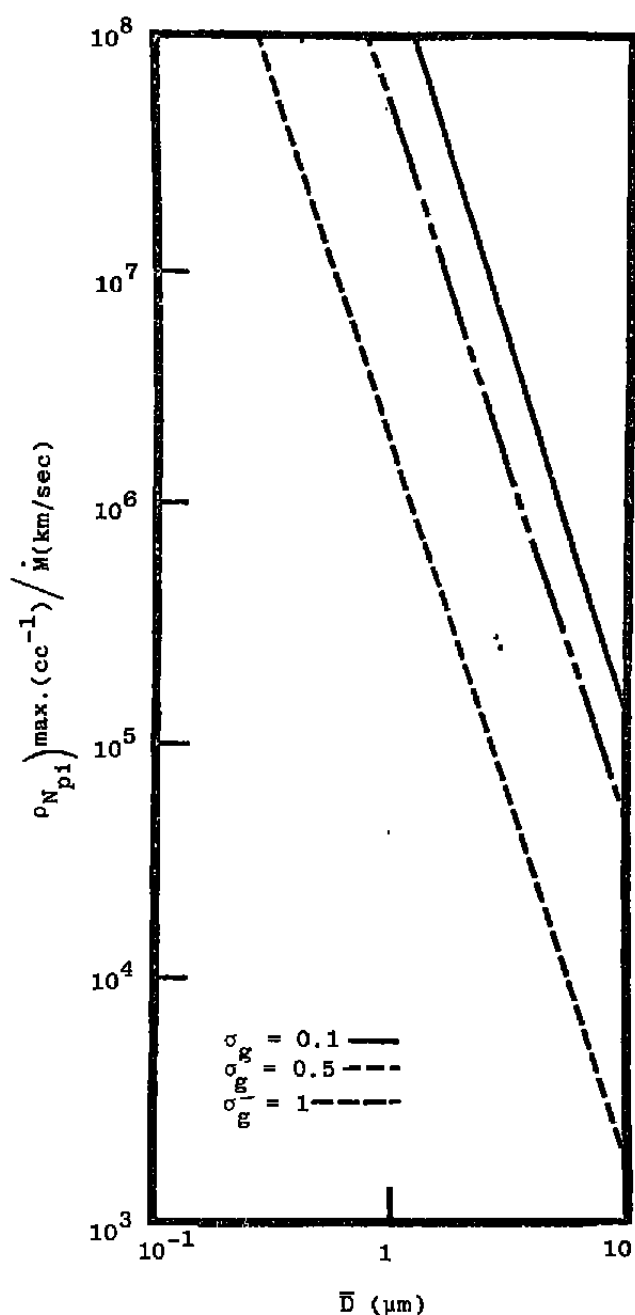


Figure 13. Number Density as a Function \bar{D} and σ When Velocity is Inversely Proportional to Plume Radius.

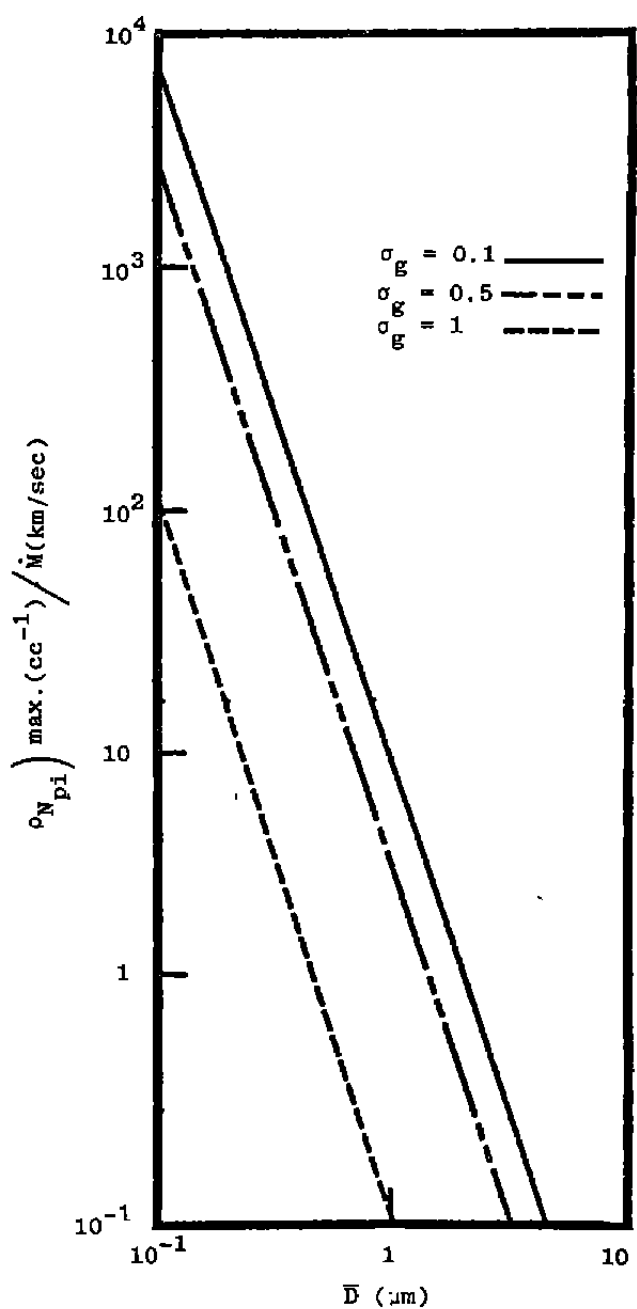


Figure 14. Number Density as a Function \bar{D} for a Radial Gaussian Velocity Distribution Across the Plume.

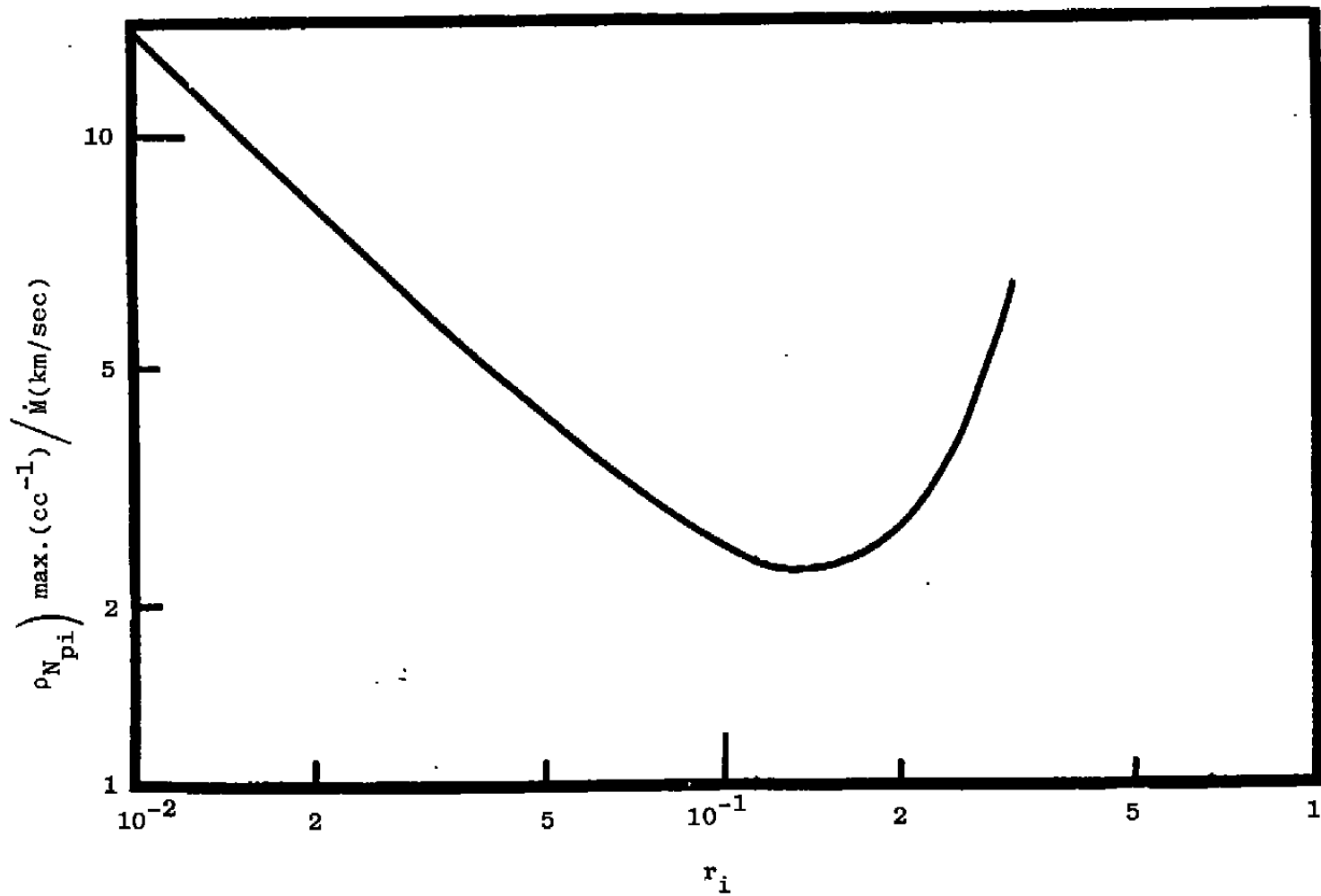


Figure 15. Number Density as a Function of Radius for Constant Particle Size and a Radial Gaussian Velocity Distribution.

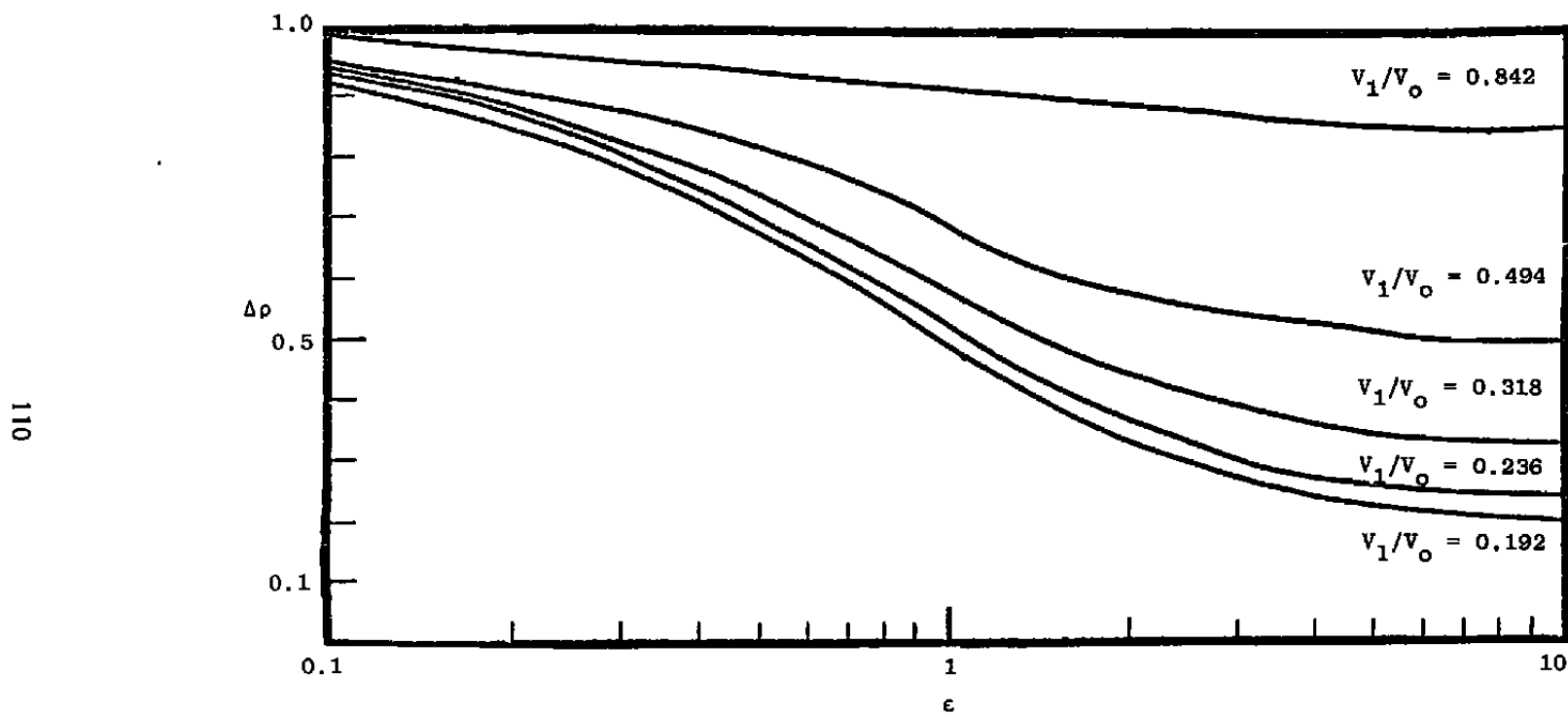


Figure 16. $\Delta\rho$ as a Function ϵ for an SRM Plume Shock.

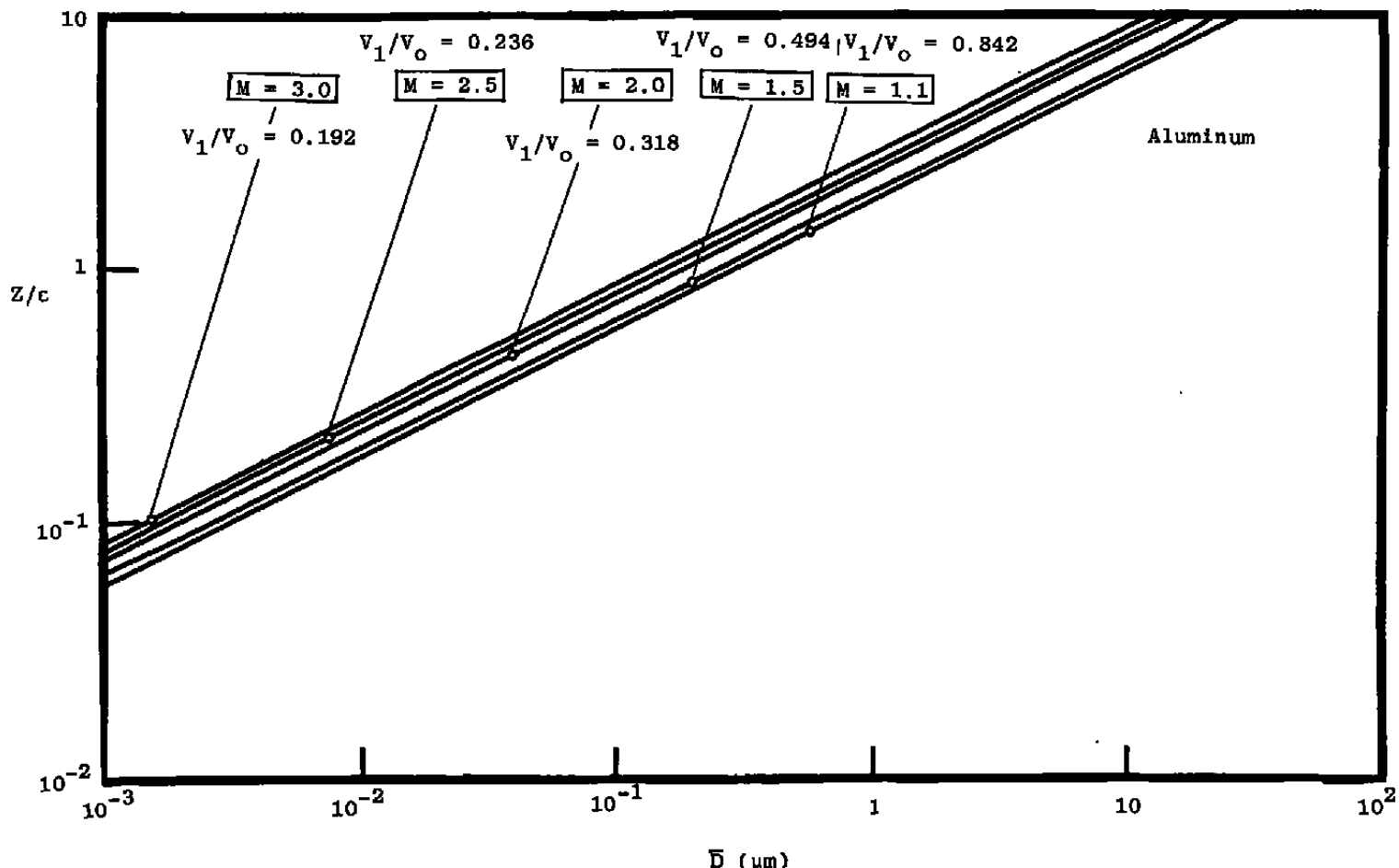


Figure 17a. Z/ϵ as a Function of \bar{D} for Values of V_1 and n Used in Fig. 16. (M = Mach No.)

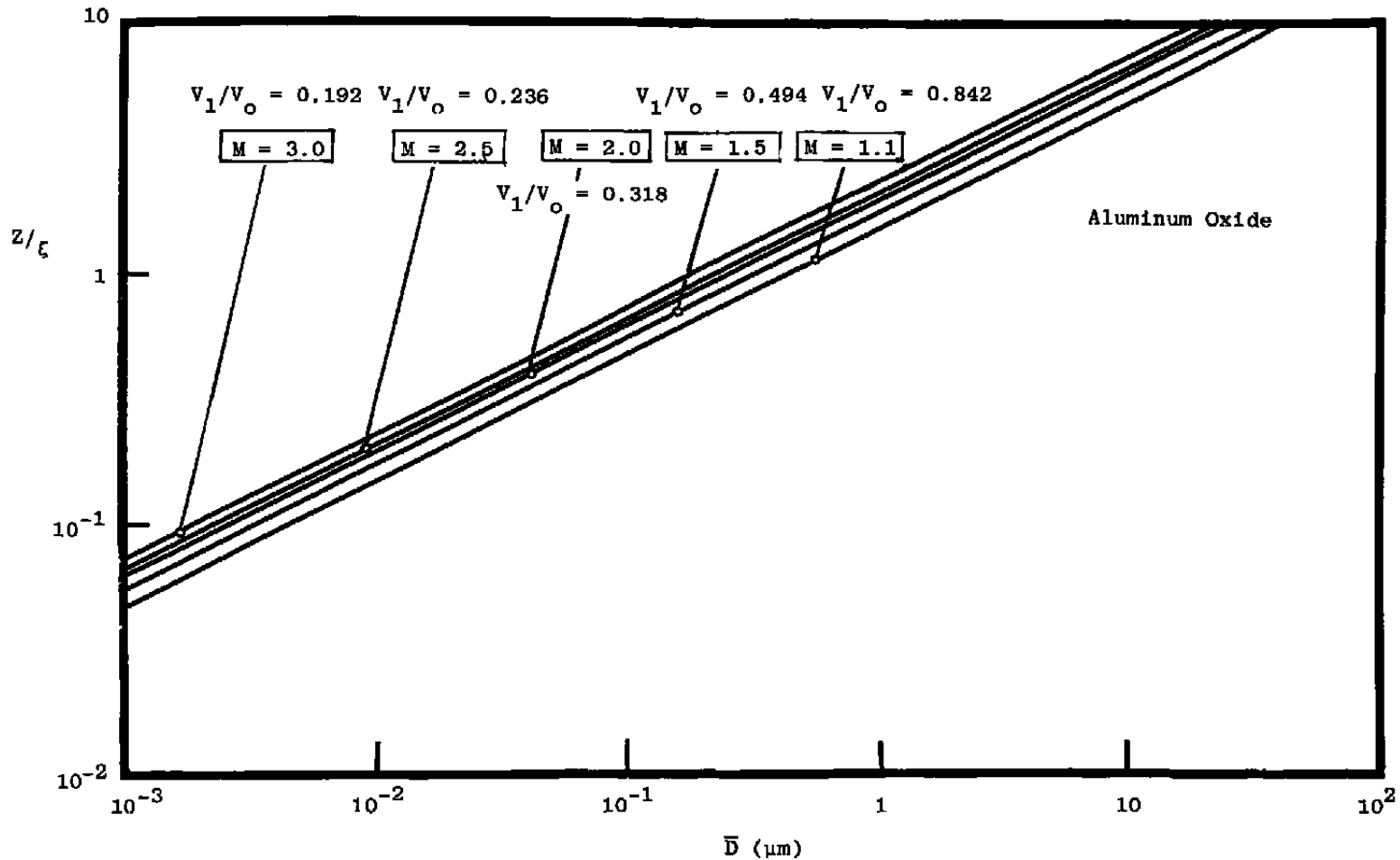


Figure 17b. Z/ξ as a Function of \bar{D} for Values of V_1 and η Used in Fig. 16. (M = Mach No.)

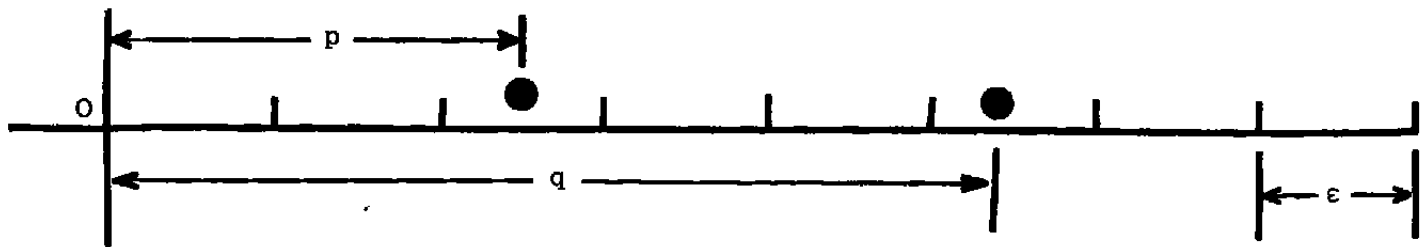


Figure 18. Visualization of p , q , and ϵ .

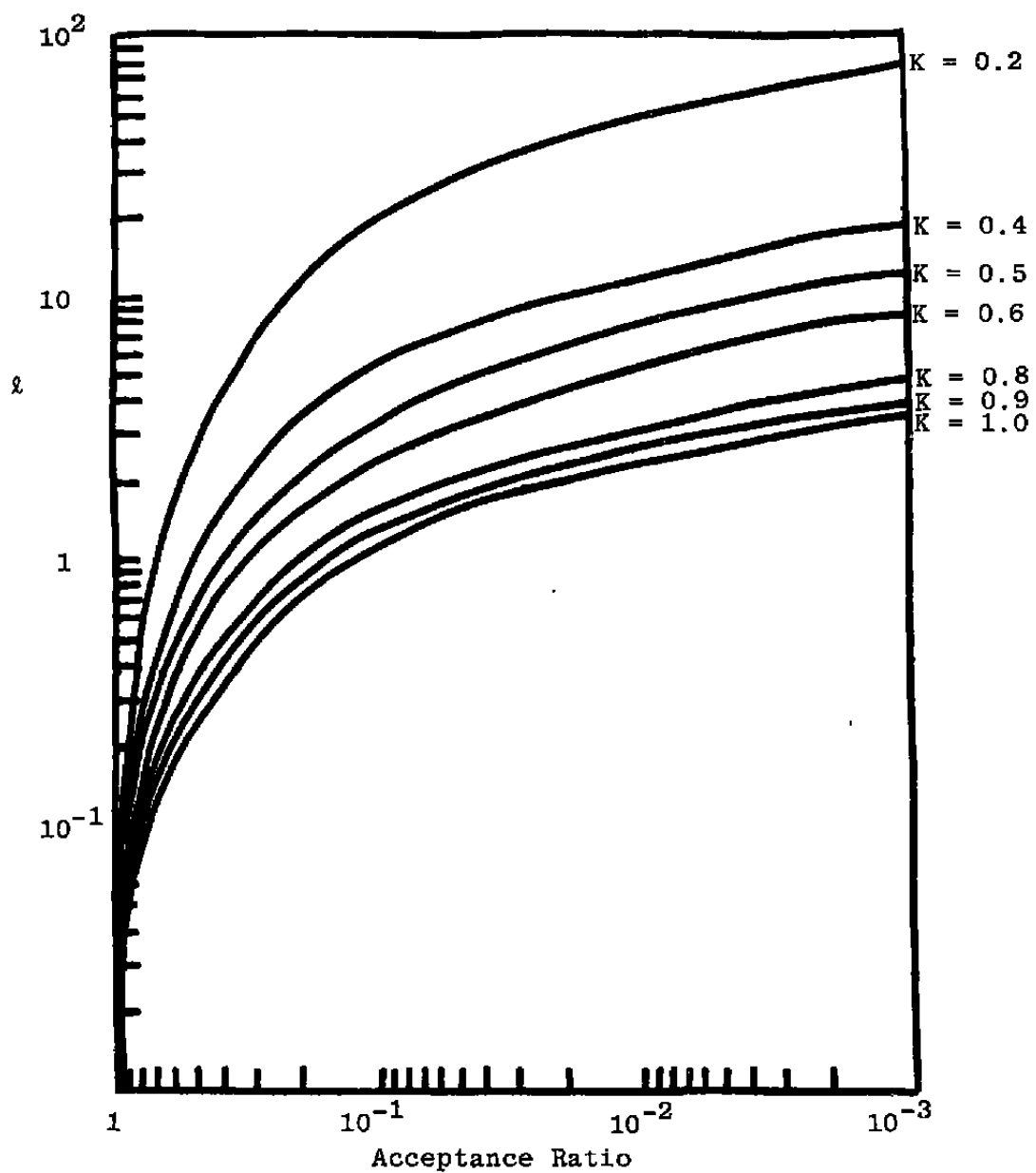


Figure 19. λ as a Function of λ With K as a Parameter.

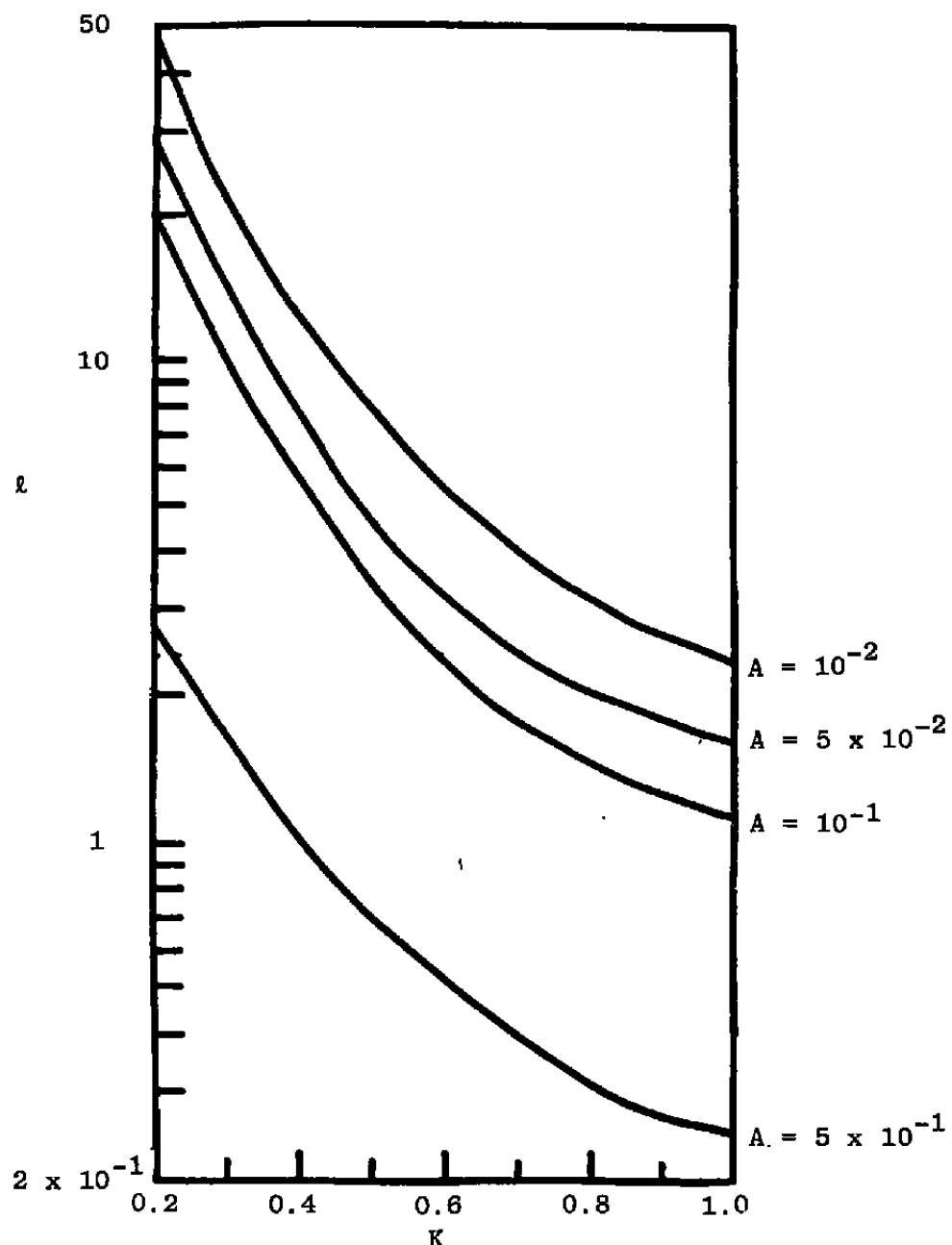


Figure 20. γ as a Function of K With A as a Parameter.

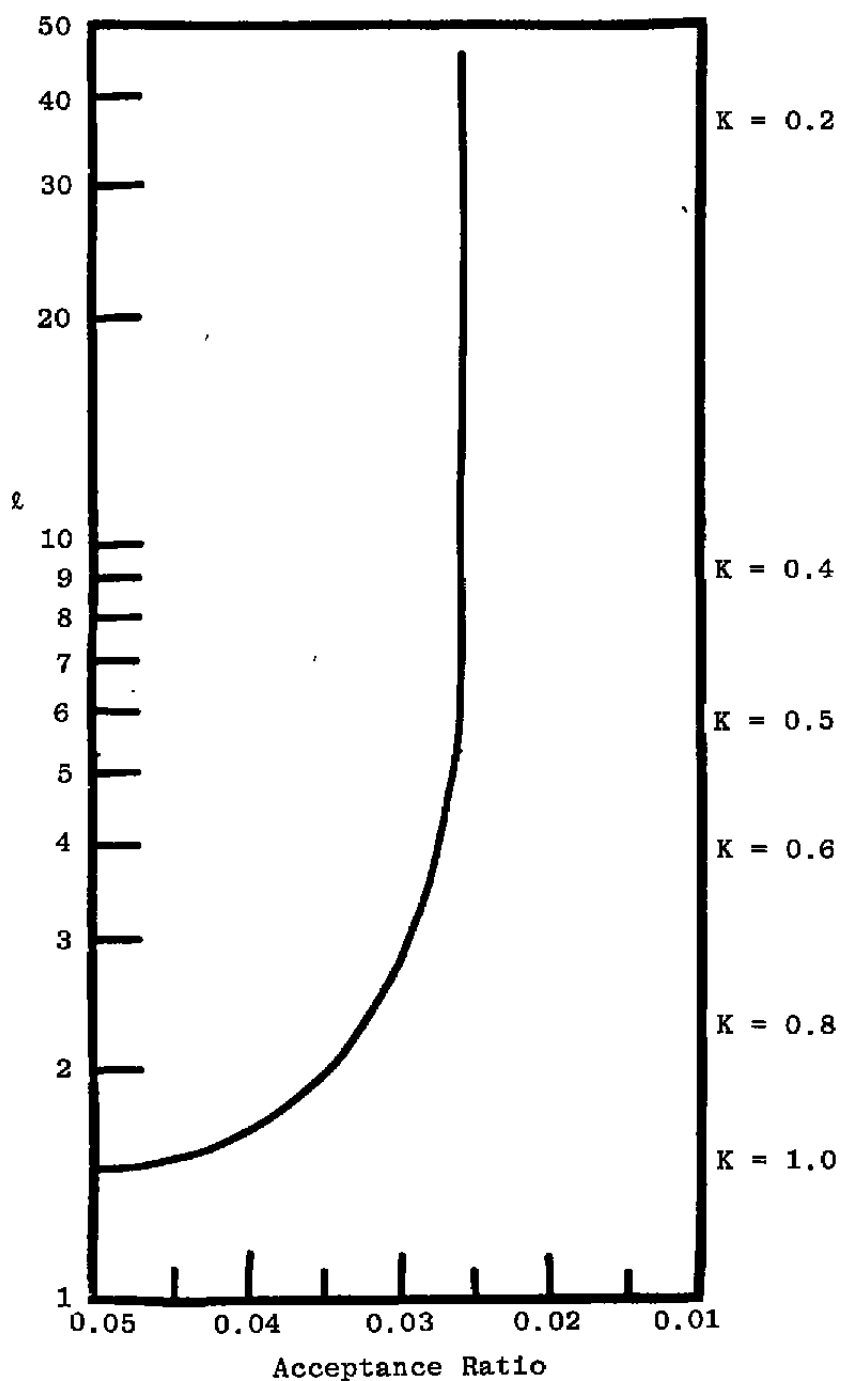


Figure 21. Optimum A for Maximum Data Rate.

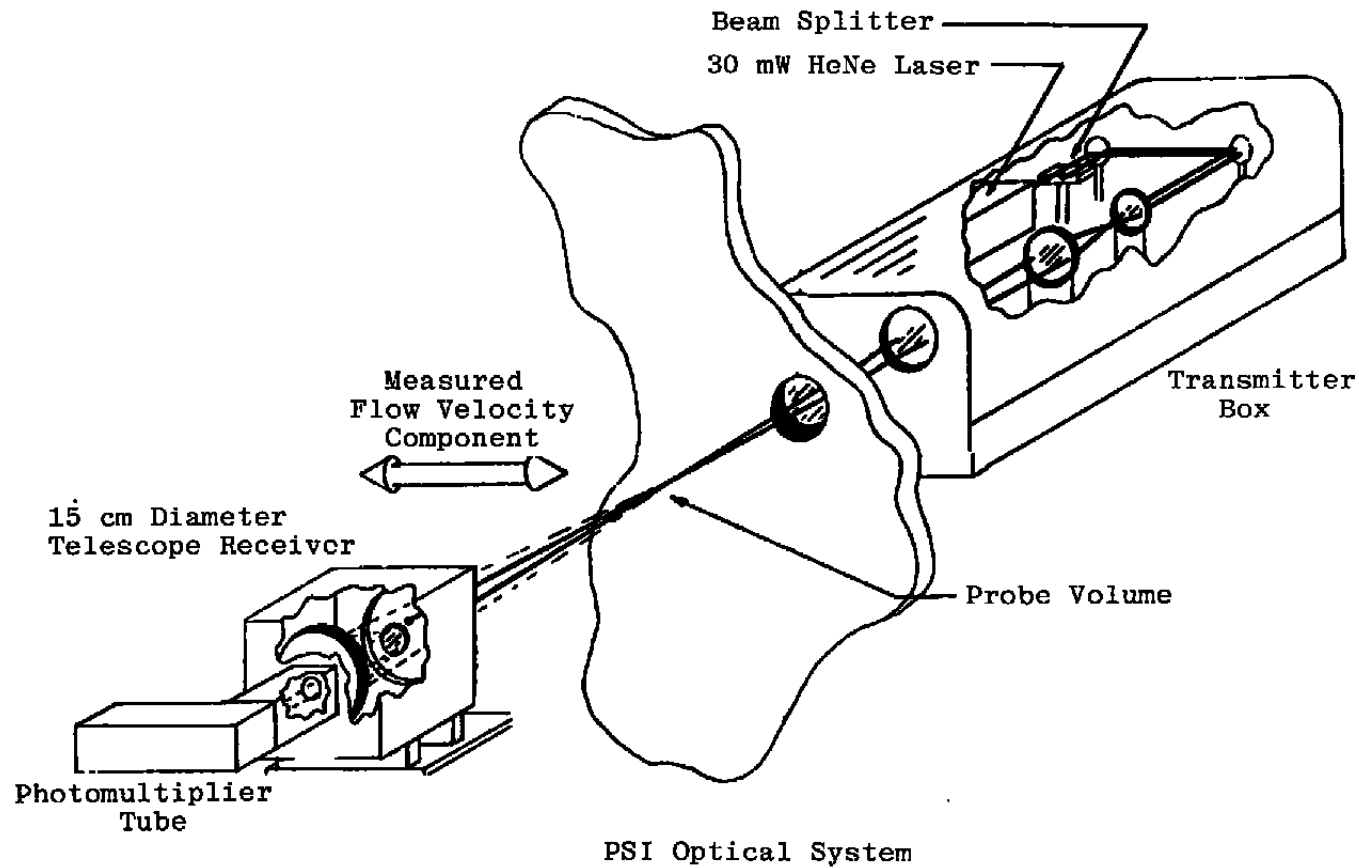
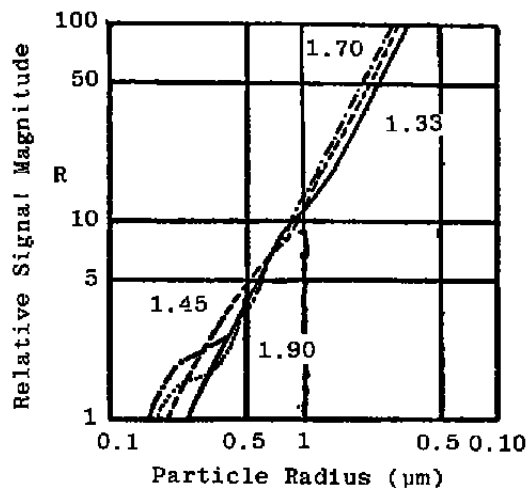
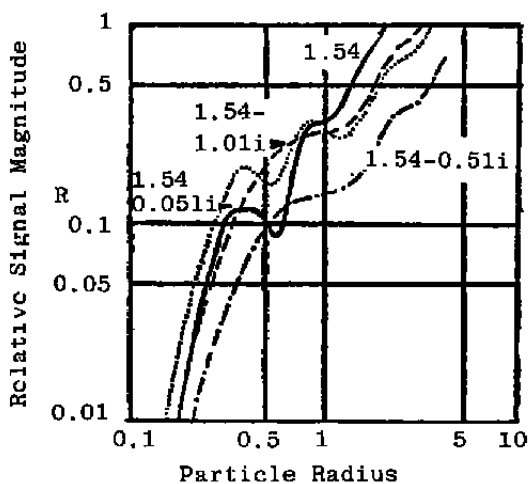


Figure 22. PSI System Used for Data in Table 1.



Particles With Real Indices of Refraction
(1.33 - 1.90) Refraction (Not Absorbing)



Particles With Complex Indices of
Refraction (0.051i, 1.54 - 1.01i)
(Absorbing).

Figure 23. Index-of-Refraction vs. Amplitude

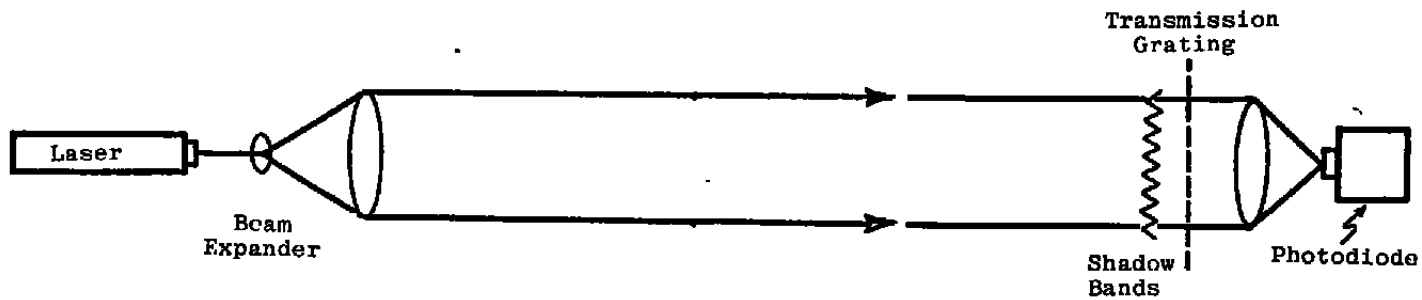


Figure 24. Schlieren Correlation System.

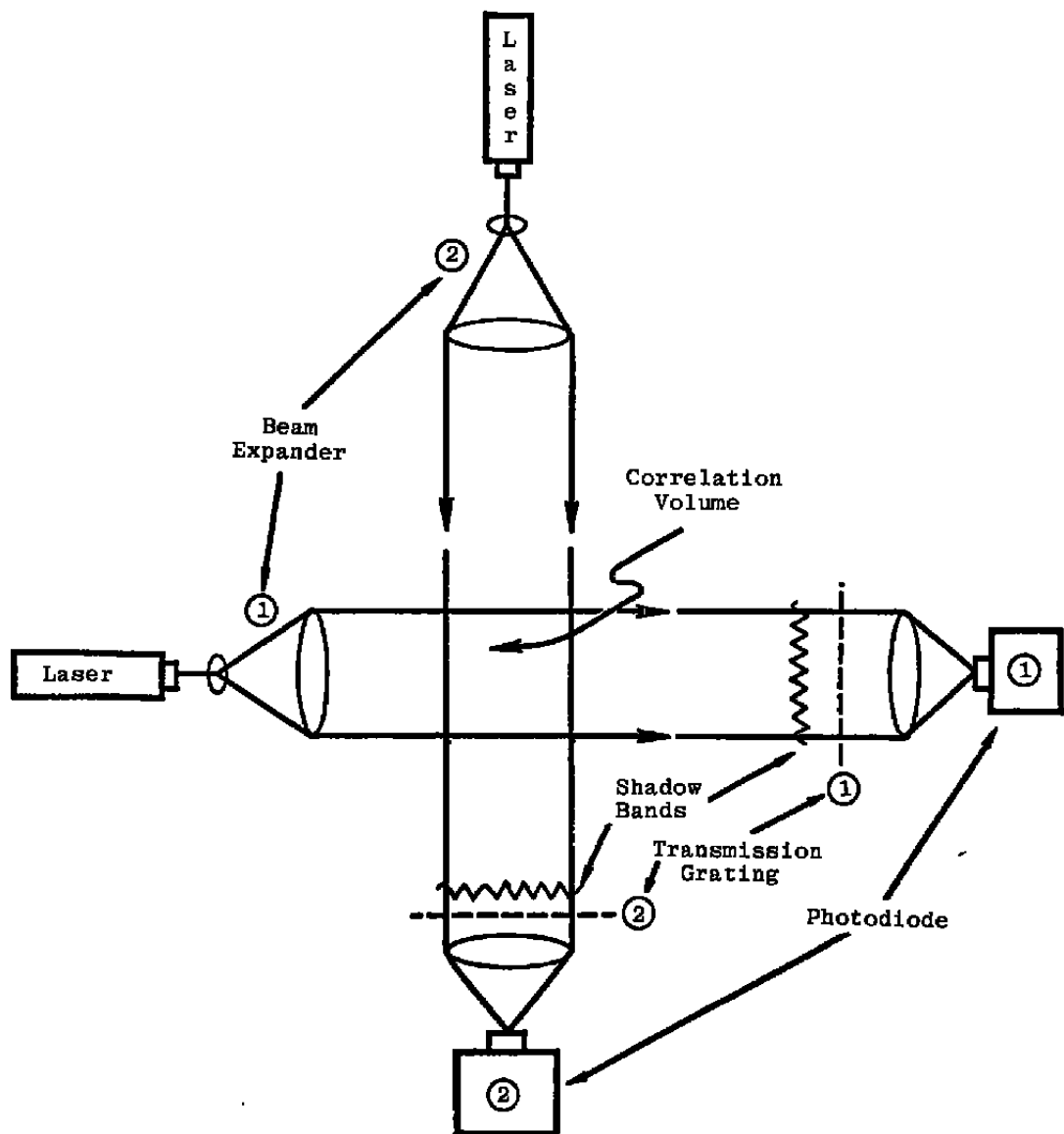


Figure 25. Crossed Beam Schlieren Correlation System.

PART II ULTRAVIOLET (UV) FORWARD MIE SCATTERING**INTRODUCTION**

The advantage of extending the Mie scattering applications into the UV is that the scattered radiation is not washed out by the plume background radiation which originates from the same and nearby plume volume elements. In addition, it allows a larger Mie size and the detection of smaller particles, i.e., delays the approach of the scattered radiation pattern to the ambiguous Rayliegh pattern as particle size decreases.

As noted in the relevant proposal and in the contract statement of work to be accomplished, three major questions need to be answered in order to accomplish a viable technique. The first is

- "(1) Does size information exist in the UV radiation being scattered by an individual particle, and what is the form of it (scattering pattern)?"

The second and third questions refer to conditions in the rocket plume and are somewhat interrelated. The second question concerns modifications of the scattering patterns by the rocket plume turbulence, and the third, techniques to utilize the size information available in the scattered UV radiation assuming such size information is present and sufficiently unambiguous. The proposal and statement of work assumed observation from outside the plume. After additional thought we would not like to rule out use of a probe provided information is obtained from plume regions unaffected by the presence of the probe.

If unacceptably ambiguous size information exists in the scattered radiation from individual plume particles, it prevents the use of the method in circumstances where the ambiguity might be present. This is true regardless of the turbulence effects or the state of technology required to observe the scattered radiation in various rocket plumes and rocket plume regions. Such results will be of continuing value to the user since they will be independent of the current state of technology.

As indicated in the statement of work, the investigation outlined by the major questions mentioned above could only be partially addressed in the time interval of this effort. In light of the above reasoning, emphasis was placed on question (1), particularly on item (b) of the last paragraph of Section 4.2.1 of the statement of work.

A survey of others in the field confirmed our belief that the Mie scattering subroutines of J. V. Dave were the best for calculation of the scattered radiation pattern from individual particles. A listing of these subroutines, DAMIE and DBMIE, was obtained (Dave, 1968). The subroutine DAMIE was used here because we deal with sufficiently small Mie size parameters, x , ($x < 100$ and $n_2x < 80$, where the index of refraction is $n = n_1 + in_2$), and an order of magnitude less storage is required, the storage requirements being considerable.

However, an adaptation of the DAMIE subroutine was achieved which ran on the UTSI DEC 11T55 and gave the same results as the various numerical and analytic test cases used for comparison. A program was developed incorporating this subroutine to allow interactive calculation of the scattered radiation patterns suitable for plotting. The other elements of the scattering matrix for the Stokes parameters and other parameters of interest are also calculated.

A plotting program was developed to take these calculated results and plot them on an automatically drawn, scaled and labeled radial grid using the UTSI Cal Comp plotter. Some time had to be spent on the development of this program and its component subroutines as apparently these were the first radial plots ever produced by computer here at UTSI. Some results are shown as Figures 1 through 22.

INTRODUCTION TO FIGURES

Plotted in Figures 1 through 22 are the scattered intensity functions which are the scattered intensities (more properly the scattered irradiances) (with units of power per unit area) observed in the far field divided by the appropriate irradiance incident on the particle and multiplied by the product $k^2 r^2$ where k is the wavenumber (2π divided by the wavelength) of the incident radiation and r is the distance of the point of observation from the particle doing the scattering. [These scattered intensity functions are the functions i_2 and i_1 of the van de Hulst (1958) and Kerker (1969).]

In the figures the direction of propagation of the incident plane wave radiation and of forward scattering is indicated by the arrow at the right. The particle doing the scattering may be thought of as being at the center of the radial grid and the intensity scattered at a given angle from the forward direction may be read off the radial plot at this same angle (the scattering angle). In any observation of the scattering from a particle, the scattering plane is the plane parallel to the prop-

agation direction of the incident radiation which contains both the scattering particle and the point of observation (the plane of the grid in the figures). The radiation scattered to the left and right of the forward direction at the same scattering angle in the scattering plane is identical regardless of the polarization of the incident radiation.

The scattered intensity function arising from linearly polarized, incident radiation polarized in, or parallel to, the scattering plane (grid plane) is plotted on the upper half of the radial grid, above the heavy line, as indicated by the parallel symbol, \parallel . [This is i_2 of van de Hulst (1957) and Kerker (1969).] This scattered radiation is also parallel polarized.

As a plot of the scattered intensity function for this polarization in the lower half of the radial grid would be redundant, it has been replaced by the scattered intensity function arising from linearly polarized, incident radiation polarized at right angles to, or perpendicular to, the scattering plane (grid plane), and this is indicated by the perpendicular symbol, \perp . [This is i_1 of van de Hulst and Kerker.] This scattered radiation is also perpendicularly polarized.

[The polarization and intensity of scattered radiation arising from incident radiation of some polarization other than linear parallel or linear perpendicular can be found by using other elements of the scattering matrix in addition to those indicated here. These are used to find the additional phase difference, δ , caused by the scattering between the parallel and perpendicularly polarized scattered field amplitudes. The normalized scattered field amplitudes are equal to the

square root of the scattered intensity functions plotted here. With the phase difference δ and these normalized scattered field amplitudes, complete knowledge of the scattering by any incident polarization is obtained. Determination of δ related characteristics generally increases the experimental complexity, however, without, as experience indicates, obtaining proportionate gains in information. For this reason δ has not been included in the information plotted by the programs developed. This can be done in a coherent way in the future, however, without the expenditure of too much additional time if completeness is desired.]

The two scattered intensity functions are plotted on an automatically labeled radial grid with radial grid lines located every 15^0 azimuth. Note that the grid is linear in keeping with potential experimental use. A sample of the line used on each curve plotted is given in the lower right hand corner of each graph along with the Mie size parameter, x , and index of refraction, n , of the spherical particle from which the scattering takes place for that curve. The Mie size parameter, x , is the circumference of the spherical particle in units of the wavelength λ (w in Figures 21 and 22). That is, with a as the radius of the sphere,

$$x = 2\pi a/\lambda \equiv 2\pi a/w$$

The parameters x and n completely determine the scattering patterns.

The scaling of the dashed and dotted lines used in some curves of the figures is necessarily by degrees of azimuth angle rather than by linear length. The longer dashed curve contains dashes of 4 degrees in length, spaces of 2. The shorter dashed curve contains dashes of 1 degree and spaces of 1 degree. The spacing between the dots of the dotted curve is also 1 degree.

DESCRIPTION OF FIGURES

Figure 1 is an essentially Rayleigh scattering case presented to orient the reader. Note the lack of 90° scattering in the parallel polarized case (upper half of grid) and the almost uniform scattering of the perpendicularly polarized radiation. This is the universal shape of the scattering pattern for small particles of x and nx much less than 1. For such particles the shape of the scattering pattern contains no size information. For a wavelength of 0.3 micrometers (300 nanometers) in the UV, $x = 1$ occurs at a spherical particle radius of .048 micrometers (diameter of .095 micrometers). We see in Figure 1 slightly more forward scattering than backward because x at .2 is still somewhat close to 1.

Figure 2 begins a series of the scattering patterns for increasing x at arbitrarily selected index of refraction $n = 1.5$. The pattern for $x = .2$ is the little blip immediately above the slashed zero labeling the

center of the radial grid. (It is slightly displaced downward with respect to the grid due to mis-registration of the plotter). For Rayleigh scatterers the amount of radiation scattered is proportional to $\lambda^2 x^6$. For fixed wavelength it is proportional to a^6 or x^6 . As x increases through $x = 1$, the rate of increase of scattering with x decreases, but there is still a strong tendency to larger scattering with larger x (more later). Note that, as x is inversely proportional to the wavelength of the scattered radiation, UV radiation implies a larger x than for scattering of visible or infrared radiation by the same particle. With 0.3 micrometer radiation compared to 0.6 micrometer radiation, for example, x is increased by a factor of 2 in the UV case and $\lambda^2 x^6$ by 8. This increasing scattered radiation with decreasing wavelength occurs with decreasing plume background radiation sufficiently far into the UV.

In Figure 3 the trends with increasing x are continued with examples at $x = 0.6$ and 0.8 . Note the radial scale change from that of Figure 2. Note also that the forward scattering lobe begins to be more pronounced.

In Figure 4 the successively larger curves are those for $x = 1.00$, 1.25 , 1.50 , and 1.75 . The small blip above the slashed zero labeling the origin is the curve for $x = 1$. Through this parameter range the backward scattering essentially disappears relative to the forward. Note the scale change from Figure 3.

In Figure 5 note the scale has increased, but not by nearly so much as from Figure 3 to Figure 4. The forward lobe continues to grow and to narrow (compare Figure 4). Note also the forward lobe is now

...

essentially the same for both parallel (||) and perpendicular (\perp) polarizations unlike those at smaller x values.

Figure 5 is a first of a series of eight (Figures 5-12) which shows successive scattering patterns arising from increases in x of 0.5, plotted two patterns to the figure. The scale of each grid increases but more and more slowly from figure to figure. In these the forward lobe, which contains by far the majority of the scattered radiation, continues to grow and narrow. There is an exception to this in the patterns shown in Figure 9 where from $x = 6$ to $x = 6.5$ the lobe decreases in size, and in the patterns of $x = 6.5$ in Figure 9 and $x = 7$ in Figure 10 where again the lobe decreases in size with increasing x . This is presaged by the relatively small increase in the lobe from $x = 5$ to $x = 5.5$ as shown in Figure 8. From Figure 10 through 12 the lobe resumes to its growth with x and continues to grow.

[This lobe recession corresponds to the sharp decrease of the scattering efficiency with x just beyond the first maximum. This decrease somewhat overpowers the increase of the particle's cross-sectional area with a^2 to cause the cross-section for scattering which is the product of the scattering efficiency and cross-sectional area, and which is proportional to the total power scattered) to slow its growth with x , oscillate some and then climb again as x increases (fixed λ)].

[The oscillations of the forward part of the forward scattering may be more pronounced than those of the scattering cross section or the total power scattered, as happens here. This is because the for-

ward part of the forward scattering is depressed by the $\sin \theta$ factor in integrating to obtain the total power scattered, where θ is the scattering angle].

The decrease of the scattering efficiency behind its first maximum, which corresponds to frontal lobe recession, steepens as n increases. (See Figures 4.12 and 4.13 of the reference by Kerker). Since n increases as the wavelength shifts to the UV in many materials, frontal lobe recession may be more pronounced in the UV.

It should be noted that the shape of the frontal lobe of Figures 5 through 12 apparently continues to narrow with increasing x even when the lobe is receding. (See the discussion below).

A scaled plot version of the program was designed but not implemented in the time available for this effort. This version will allow easy comparison of such features as forward lobe shapes.

The final scattering pattern of the series of increasing x with $n = 1.5$ is the solid curve of Figure 13 for $x = 10$ ($x = 10$ corresponds to a 0.95 micrometer diameter spherical particle at 0.3 micrometers wavelength). Plotted on Figure 13 are patterns for fixed Mie size parameter, $x = 10$, (i.e., fixed particle size at fixed wavelength) and fixed real part of the index of refraction, $n_1 = 1.5$, with increasing imaginary part, n_2 . [The curve of $n = 1.5 + i 0.001$ falls on top of that of $n = 1.5 + i 0$.] Increasing n_2 implies going from a material which is highly transmitting to one which is not. Note that the forward lobe size is strongly affected, but its shape is not nearly so. (See the discussion below).

The program output plots may be scaled up as seen in Figure 14, where the first curve of Figure 13 is plotted but scaled up 100 times. The nodes and lobes thus revealed, though low in intensity compared to the forward lobe, may also serve as indicators of size.

The beginning of a series of these with increasing x is shown in Figures 15 through 18. Note that these are scaled up plots of the curves on Figures 4 and 5. In Figure 15, which is the curve of Figure 4 scaled up 100 times, one sees the node in the parallel polarization pattern at small x moving to the rear and becoming shallower as x increases. The view is somewhat cut off, particularly for the perpendicular polarization, and in Figure 16 these curves are scaled down 10 times (up 10 times from Figure 4).

In Figure 16 the successively larger forward lobes with increasing x can be traced backward to locate the backward lobes where the curve styles used become ambiguous. We see the backscatter grow ($x = 1 \rightarrow x = 1.25$) and then shrink. At $x = 1.5$ a node has begun to form at the back of the perpendicular polarization scattering pattern and by $x = 1.75$ it has become well formed and moved forward some. We can expect this node to continue to move forward with increasing x (see Figure 4.68 of Kerker, 1968). In Figure 17 we have advanced to $x = 2$ and 2.5 at a scale 100 times that of the plot of the same patterns in Figure 5. Note that the scale differs from that of Figure 16 by only 20% so it can be seen that the backward scattering has increased tremendously. The node in the parallel polarization pattern has not moved backward much at $x = 2$,

but is much shallower (see $x = 1.75$ in Figure 15). The node in the perpendicular polarization has sharpened considerably and continued to move forward. As the curve for $x = 2.5$ is essentially off this figure these curves have been replotted on Figure 18 scaled down 10 times (scaled up 10 times from Figure 5). Here to our disappointment we see the sharp node of $x = 2$ has become much shallower (it is located now at 90°). (Other features are the backward node in the parallel polarization pattern remaining shallow and new, shallow nodes forming at about 90° in the parallel and 135° in the perpendicular).

Leaving this sequence we turn to the data for $x = 10$ of Figure 13 and look at the effect of the imaginary part of the index of refraction, n_2 , on these inner nodes and lobes in Figures 19 and 20. In Figure 19 we see $n_2 = 0.0$ and 0.001 and note these curves practically fall one on top of the other. With larger n_2 in Figure 20, the backward and sideward lobes are severely altered, considerably shrunk at $n_2 = 0.1$ and run together at $n_2 = 1.0$. The lobes to either side of the forward lobe, though still present, are reduced in size and are shifted toward the forward direction about 10° .

The program developed accepts either x , the Mie size parameter, or a and λ (the latter is w on the plots), the particle radius and wave length. This may be an aid in particular cases, especially in some presentations (the results hold for all similar x so long as n remains the same). A sample is shown in Figures 21 and 22 for a radius of 2.5 micrometers and a wavelength of 314 nanometers for the same n_1 (1.5) and the same range of n_2 as in the $x = 10$ figures (Figures 13, 14, 19 and 20). Here, in Figures 21 and 22 x is very close to 5.

In Figure 21 the forward lobe is again seen to be essentially the same for $n_2 = 0.0$ or 0.001 . For $n_2 = 0.1$ it shrinks dramatically and for $n_2 = 1.0$ it shrinks even more. In Figure 22 the scale is increased 100 times and the backward and sideward lobe structure is also seen to be greatly affected at the higher n_2 values.

DISCUSSION

A tool has been generated to allow analysis of the scattering patterns from spherical particles for the size information present and for ambiguities in that information. This needs to be applied to particles of indices of refraction typical of materials found in rocket plumes. Emphasis in analysis should be, first, on the forward lobe shape which, as the forward lobe arises from diffraction to a large extent, should be somewhat independent of particle material and, hopefully, of oscillations with increasing x . This has been noted before (Hodkinson, 1966; Kerker, 1969), and is the means used in some commercial instruments. Secondly, emphasis should be placed on the propagating nodes, particularly those formed at low x values. (For references to earlier work see Section 7.4.1 of Kerker, 1976). These nodes have the disadvantage of involving lower scattered radiation levels than the forward lobe, and while they may be amenable to backward observation, they may be too much affected by the uncertainty of the index of refraction of the particle being measured to be useful in that direction.

In addition to observing the above, the program ought to be modified to accommodate approximation techniques which use Mie scattering theory with varying particle radius and index of refraction with

angle to obtain the scattering pattern of spheroids (Latimer et al., 1978). Thus, the effect of non-spherocity, particularly on the forward lobe, could be examined to see if ambiguity arises, at least where the Rayleigh-Gans-Debye approximation holds.

REFERENCES FOR
ULTRAVIOLET MIE SCATTERING

Dave, J. V., "Subroutines for Computing the Parameters of the Electromagnetic Radiation Scattered by a Sphere," IBM Palo Alto Scientific Center Report No. 320-3237, Palo Alto Scientific Center, IBM Corporation, P. O. Box 10500, Palo Alto, California 94303 (May 1968).

Hodkinson, J. R., Applied Optics 5, 839 (1966).

Kerker, M., The Scattering of Light and Other Electromagnetic Radiation, (Academic Press, New York, 1969).

Latimer, P., A. Brunsting, B. E. Pyle and C. Moore, Applied Optics 17, 3152 (1978).

van de Hulst, H. C., Light Scattering by Small Particles, (John Wiley & Sons, New York, 1957).

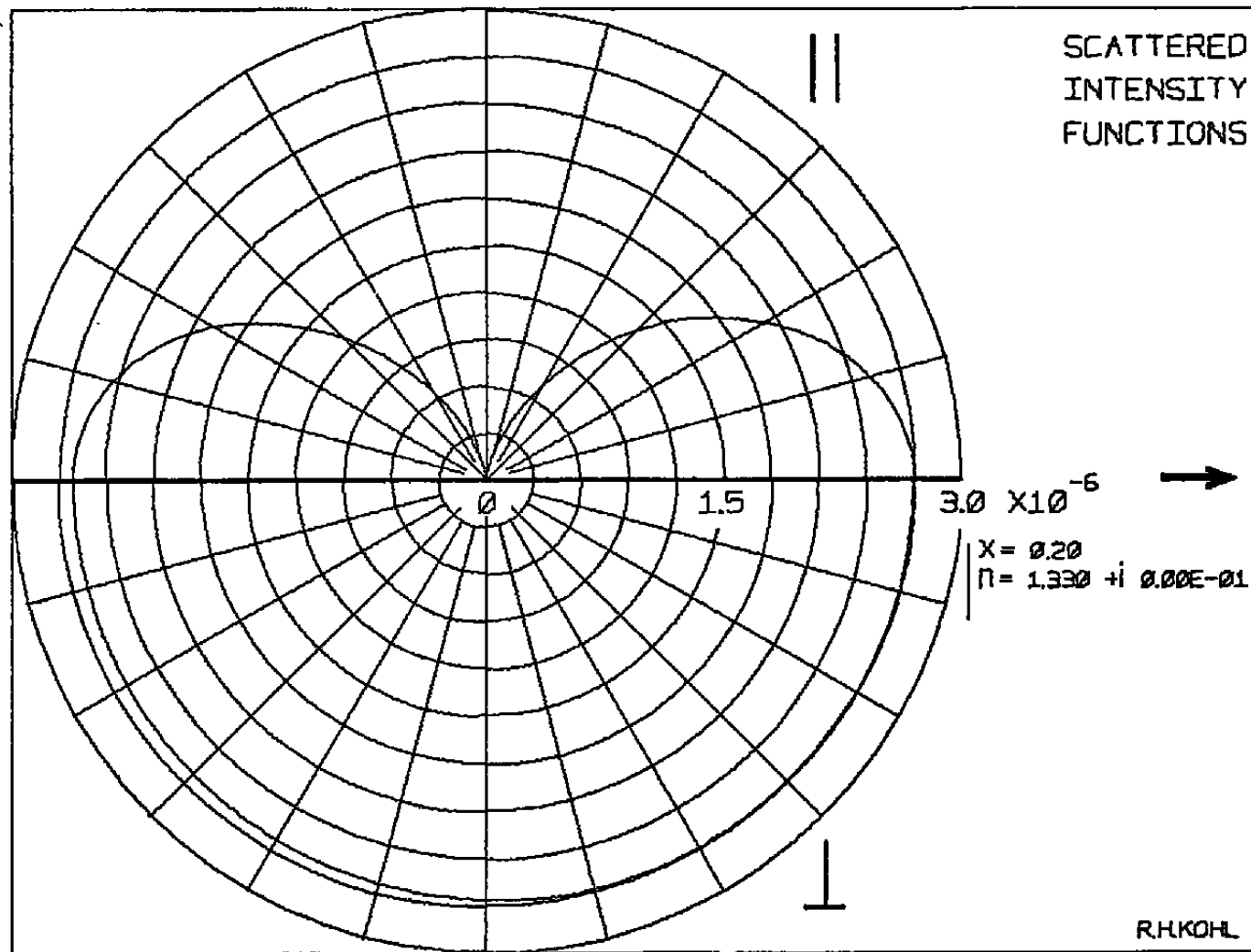


FIGURE 1

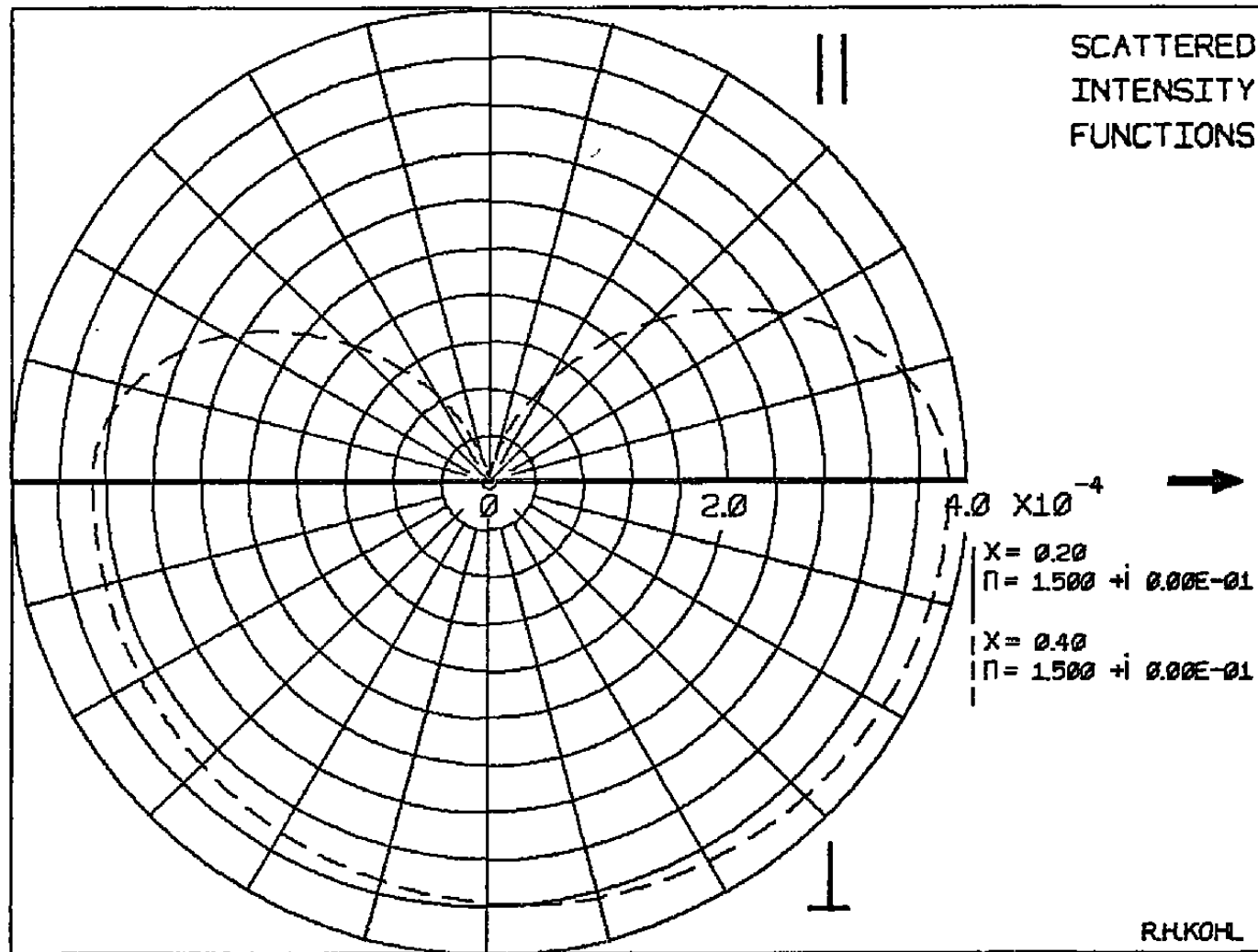


FIGURE 2

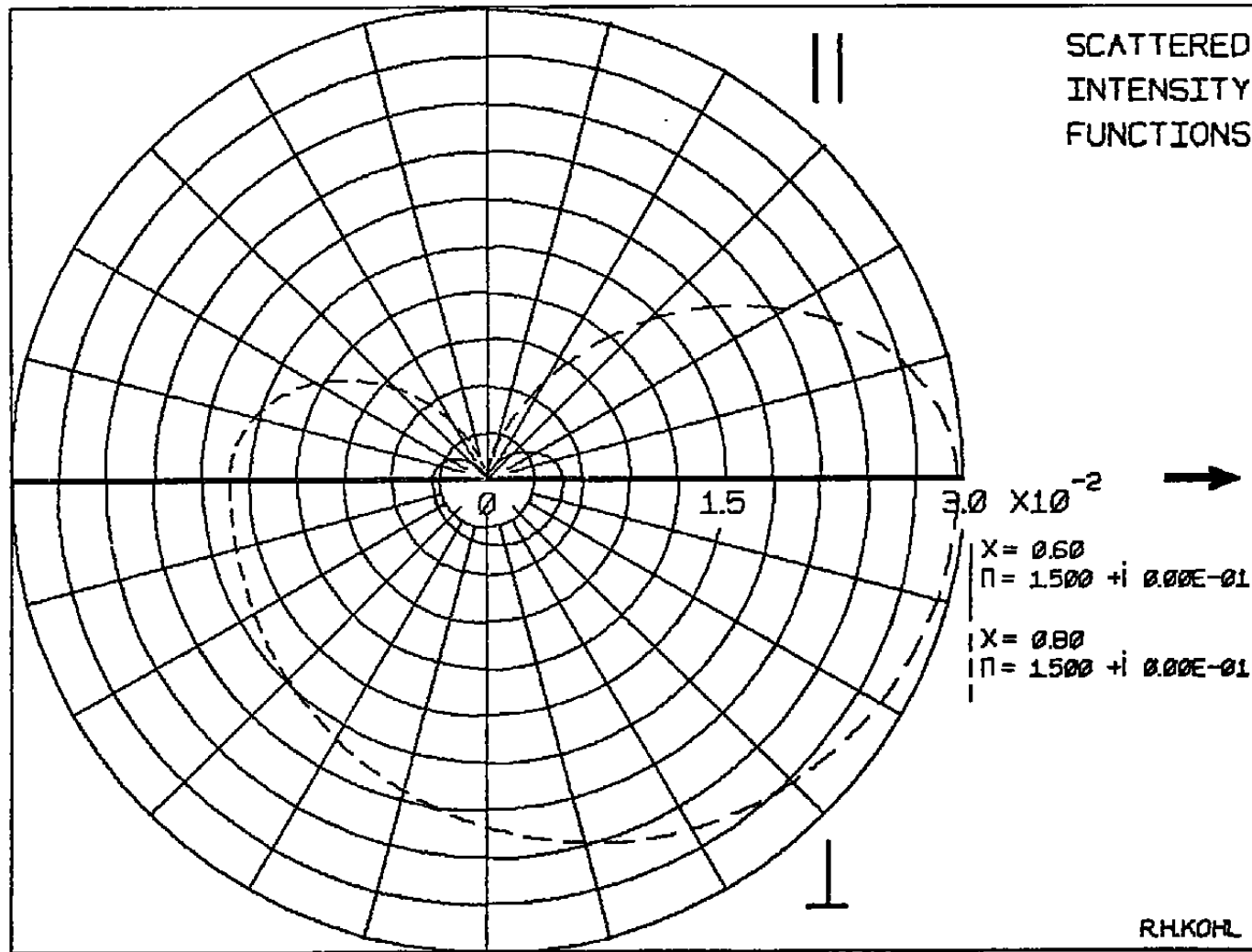
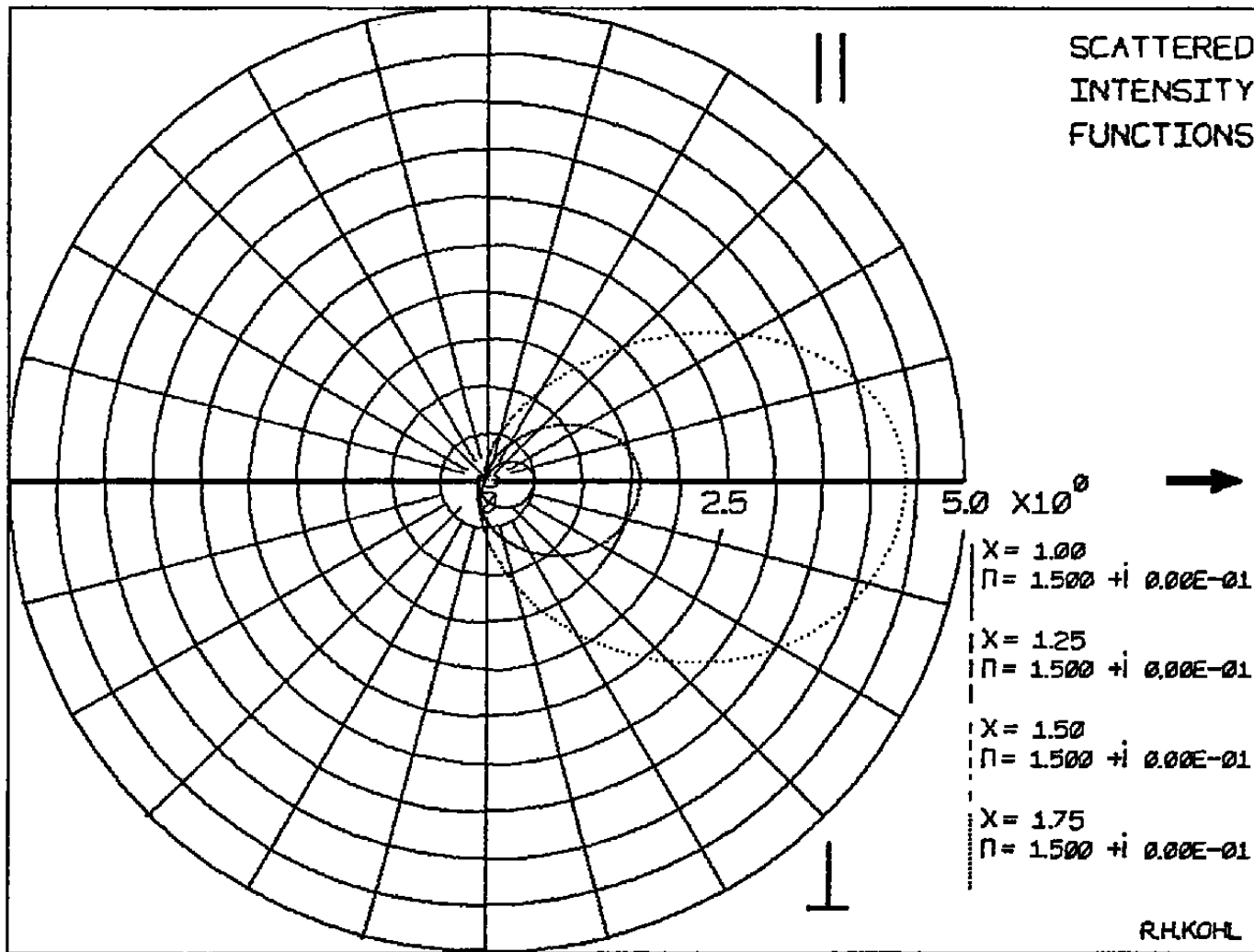


FIGURE 3



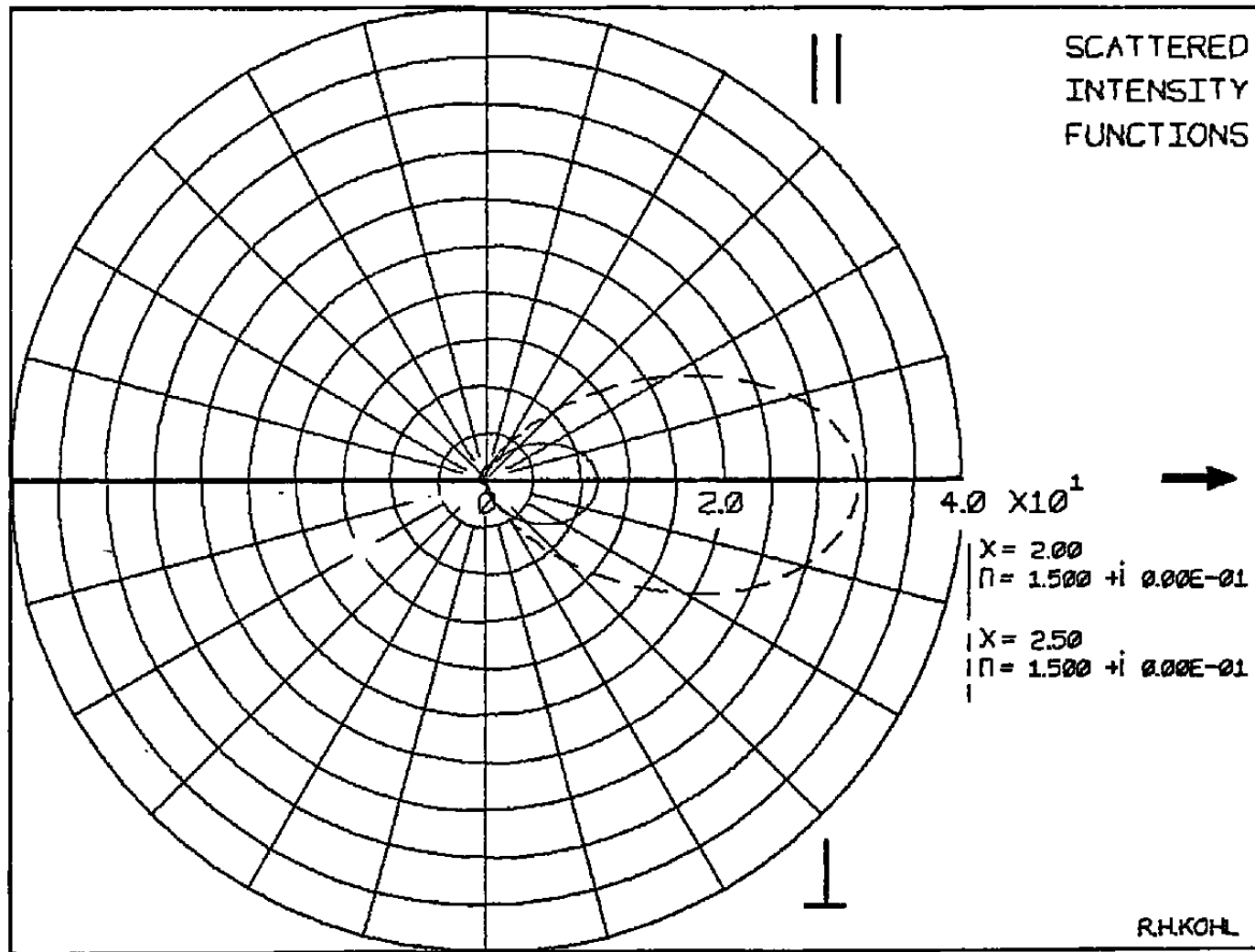


FIGURE 5

140

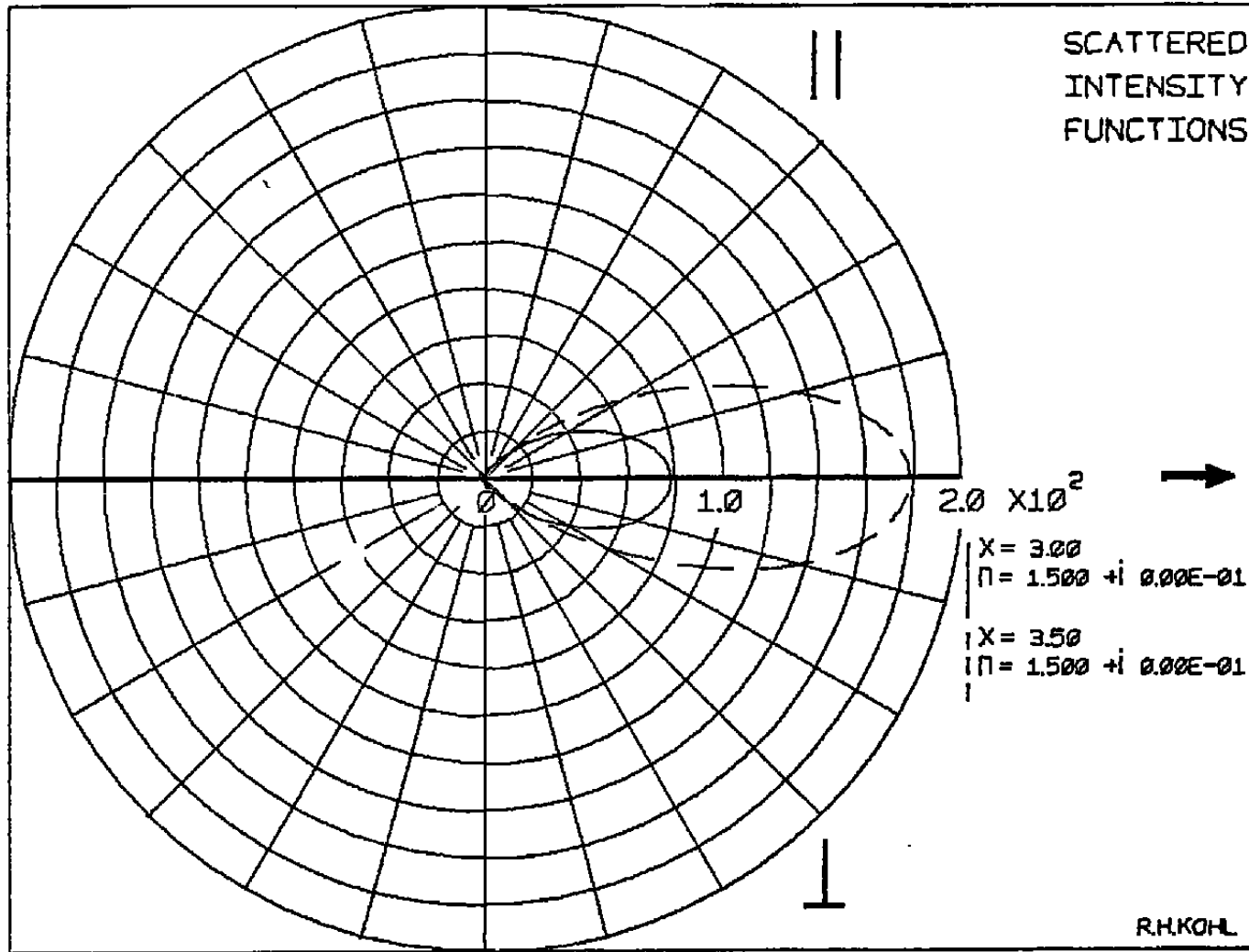


FIGURE 6

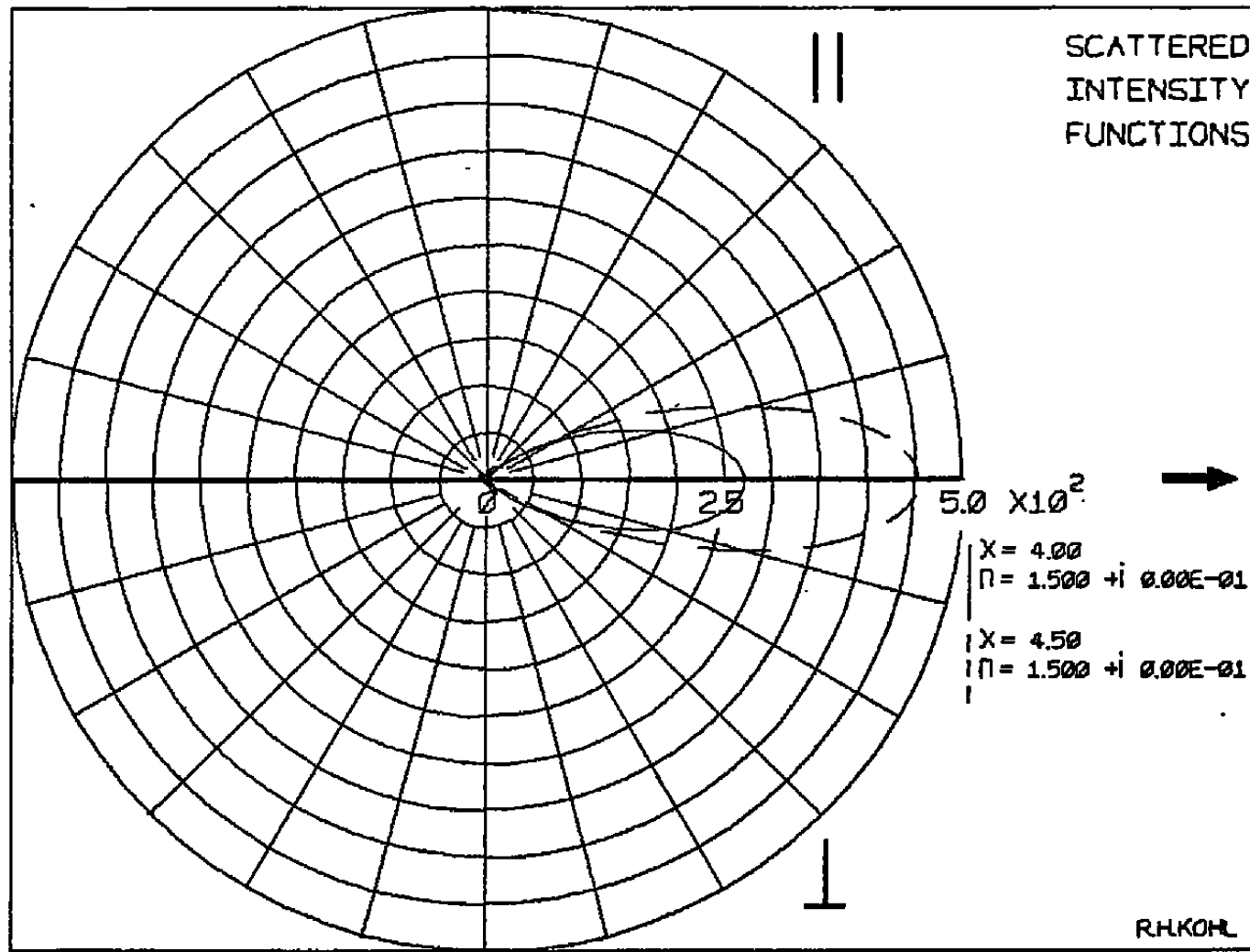


FIGURE 7

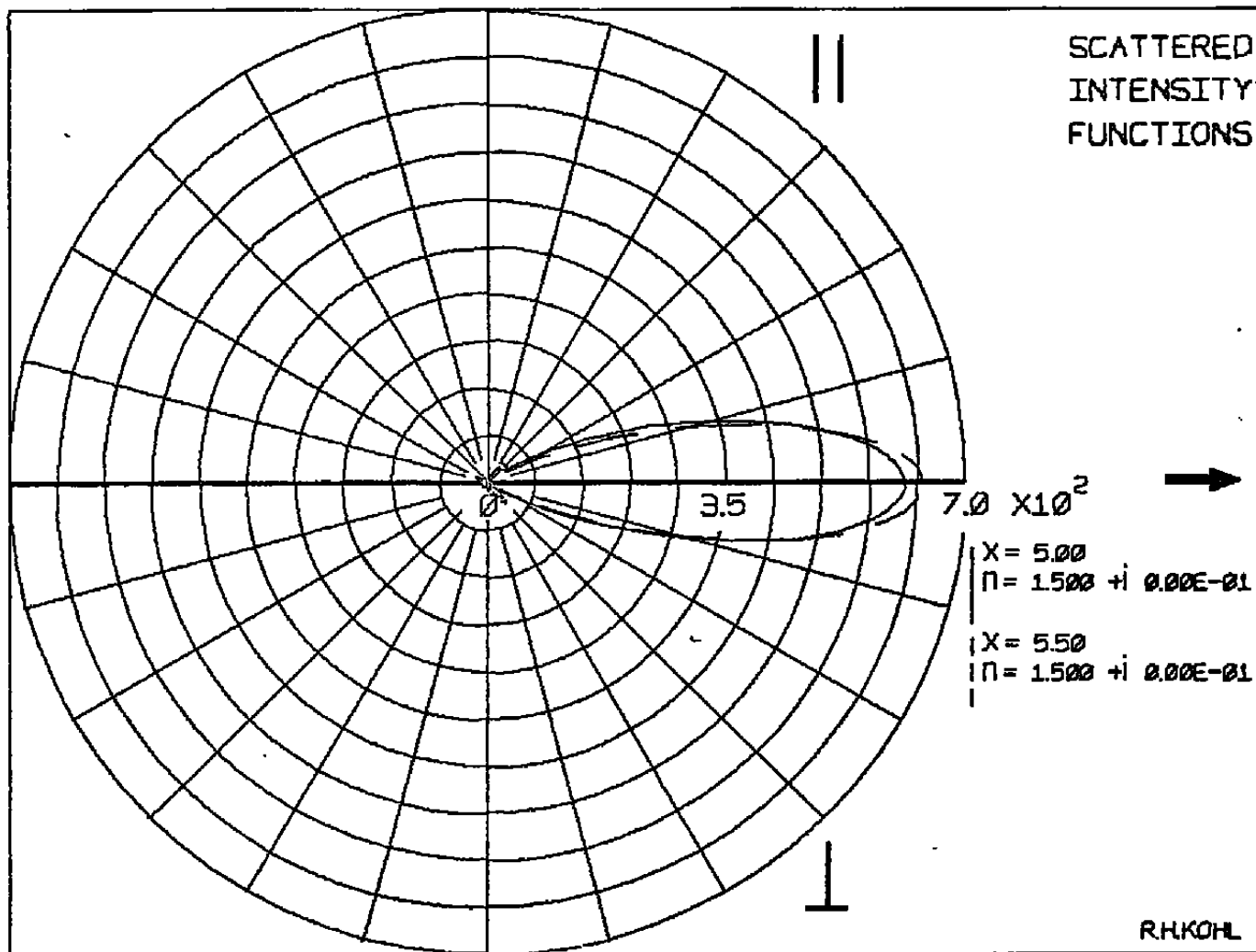


FIGURE 8

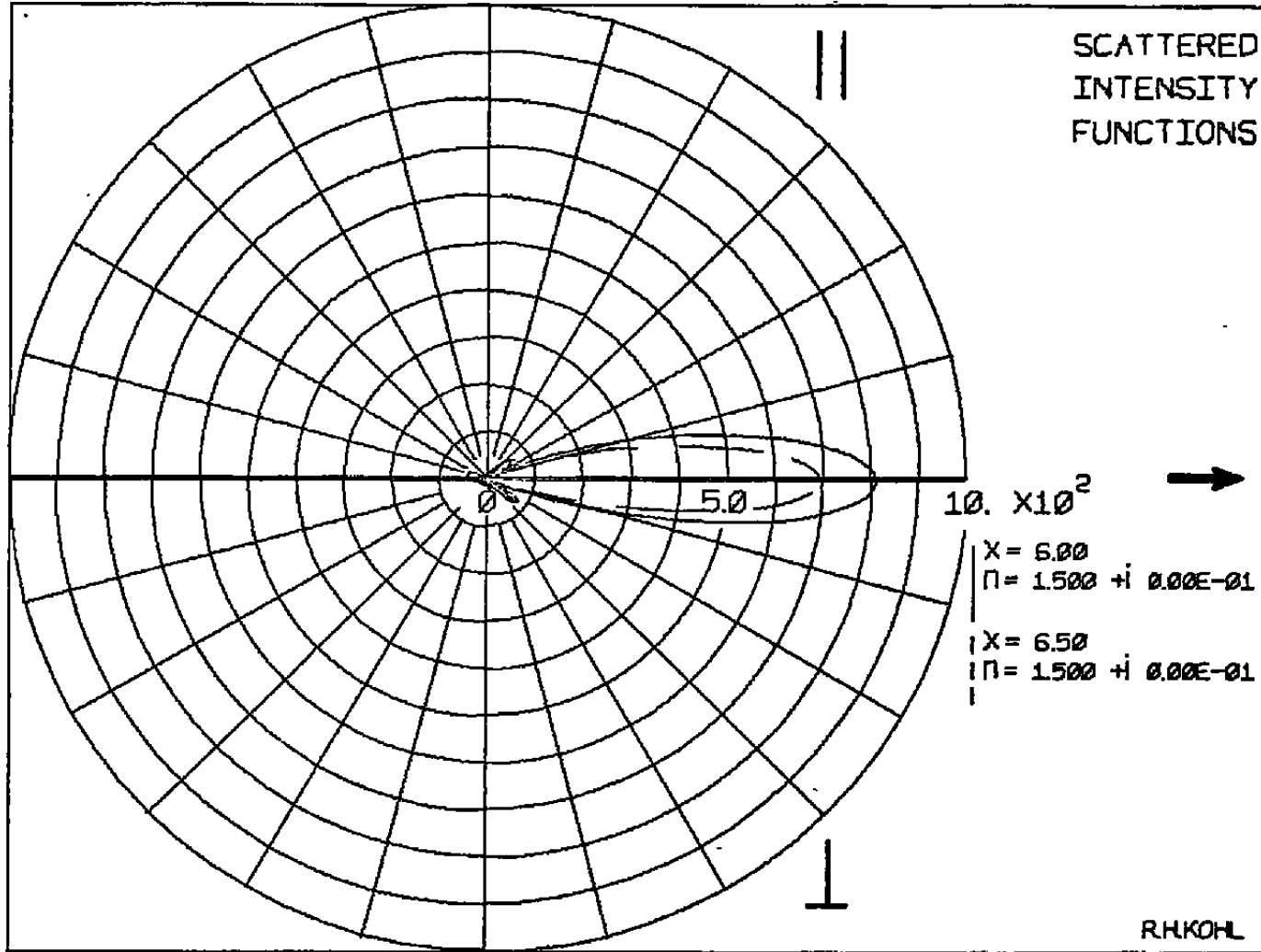


FIGURE 9

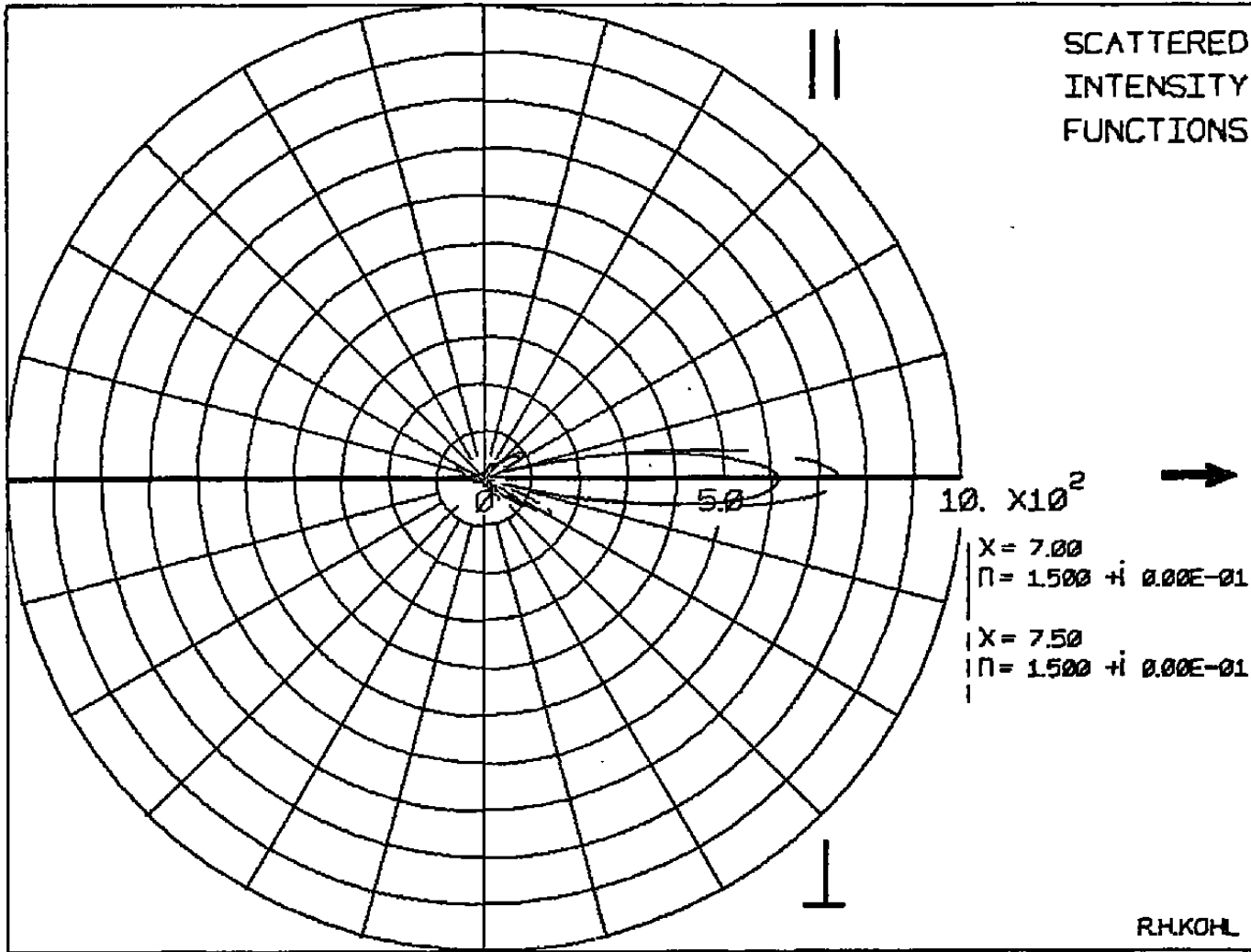
SCATTERED
INTENSITY
FUNCTIONS

FIGURE 10

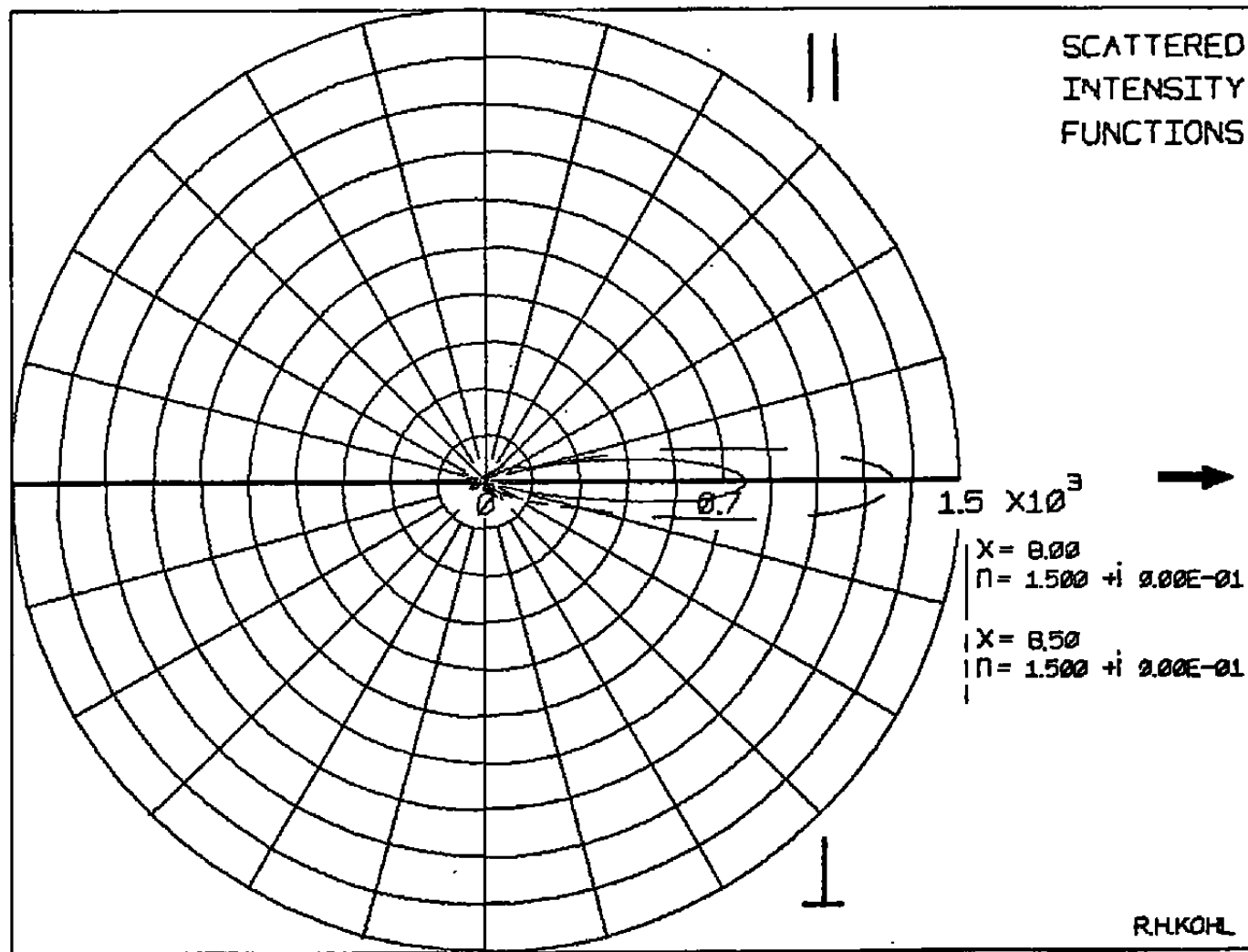


FIGURE 11

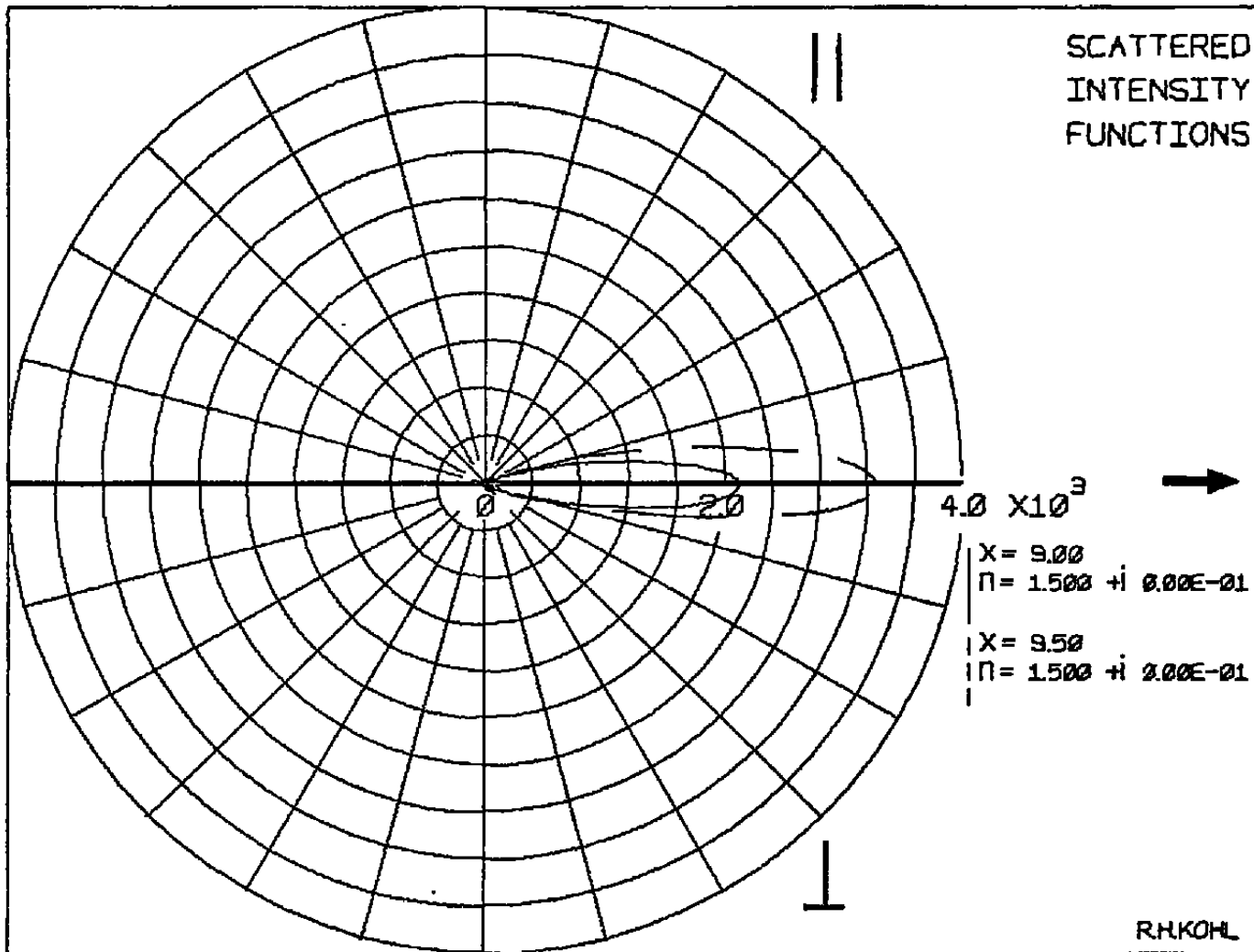


FIGURE 12

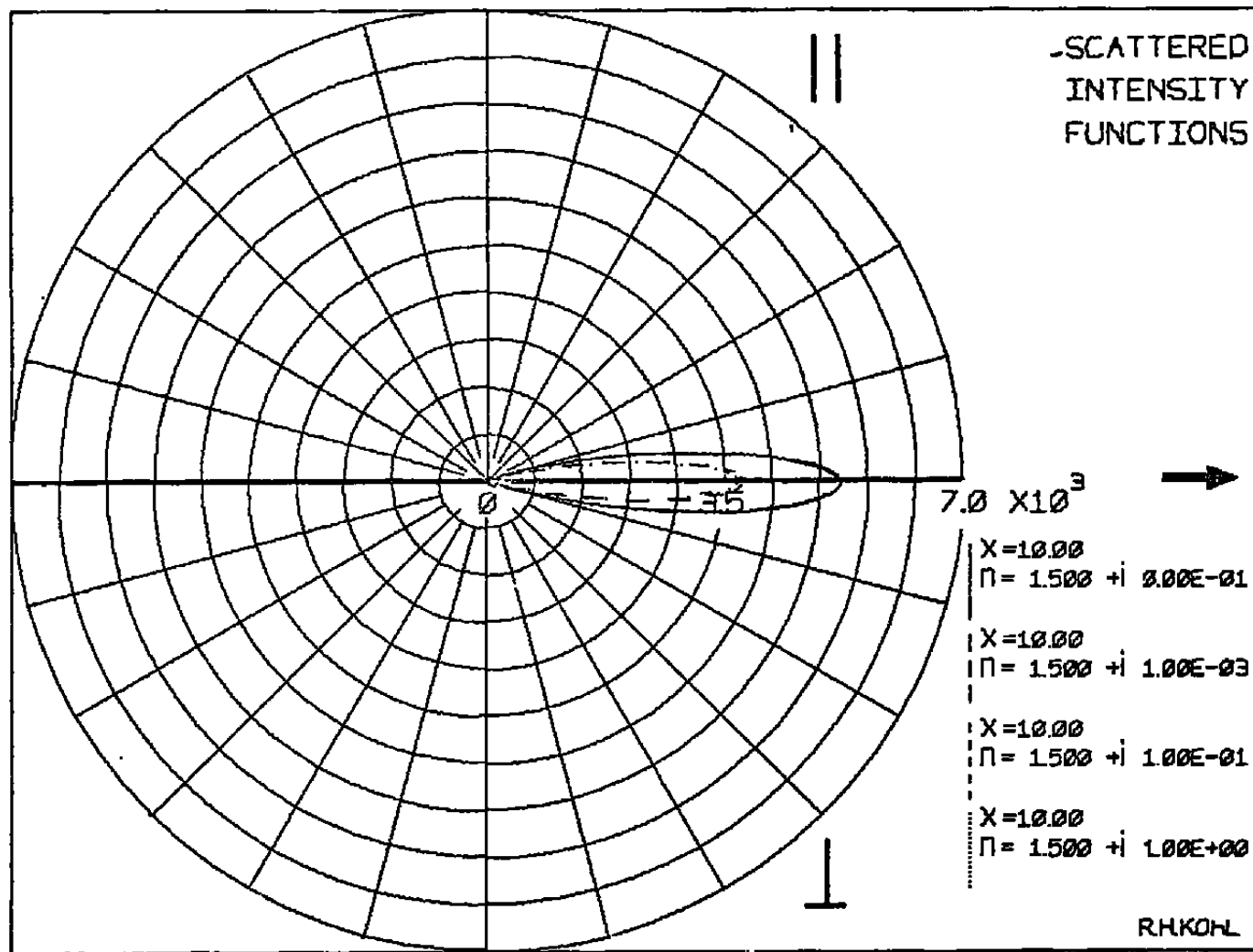


FIGURE 13

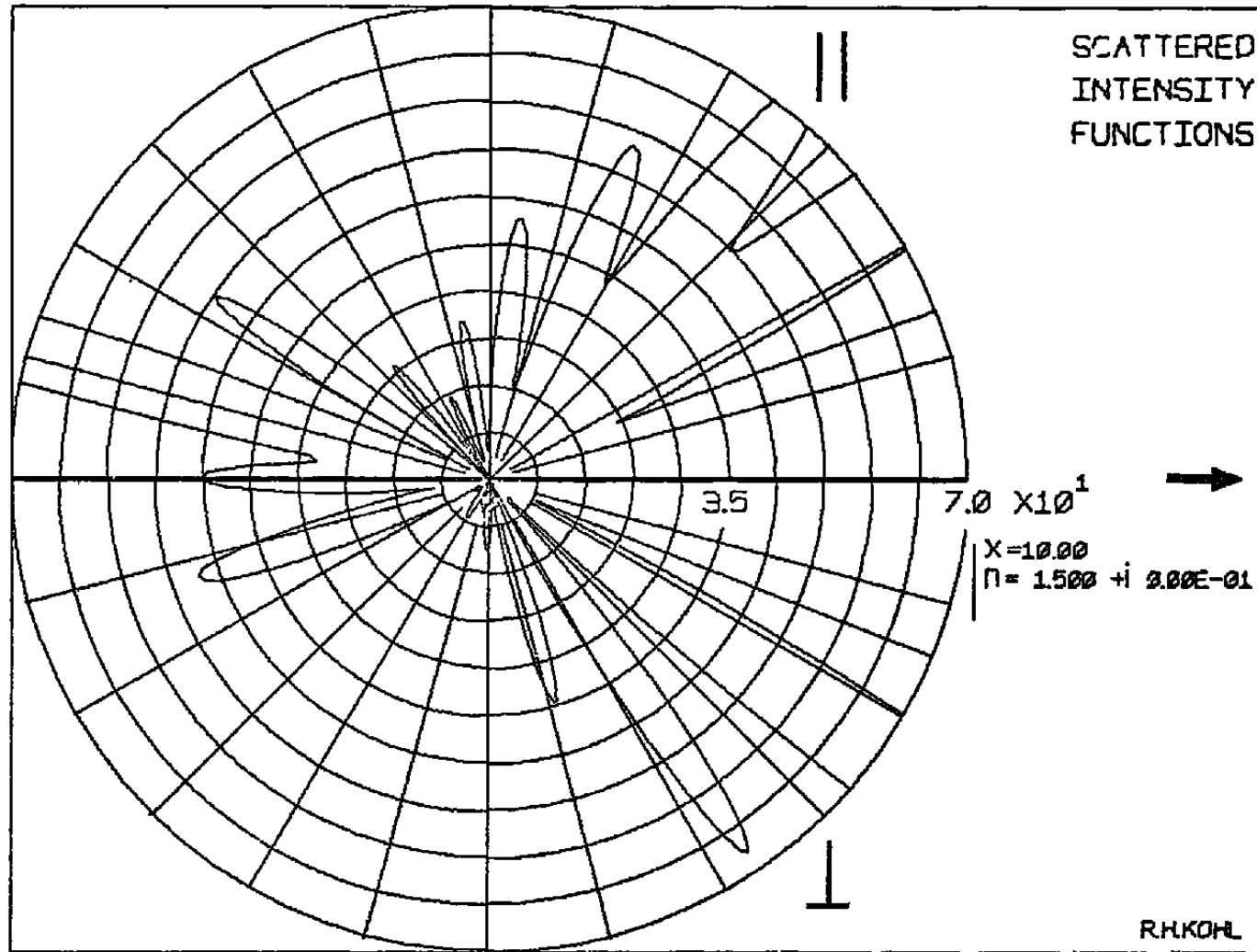


FIGURE 14

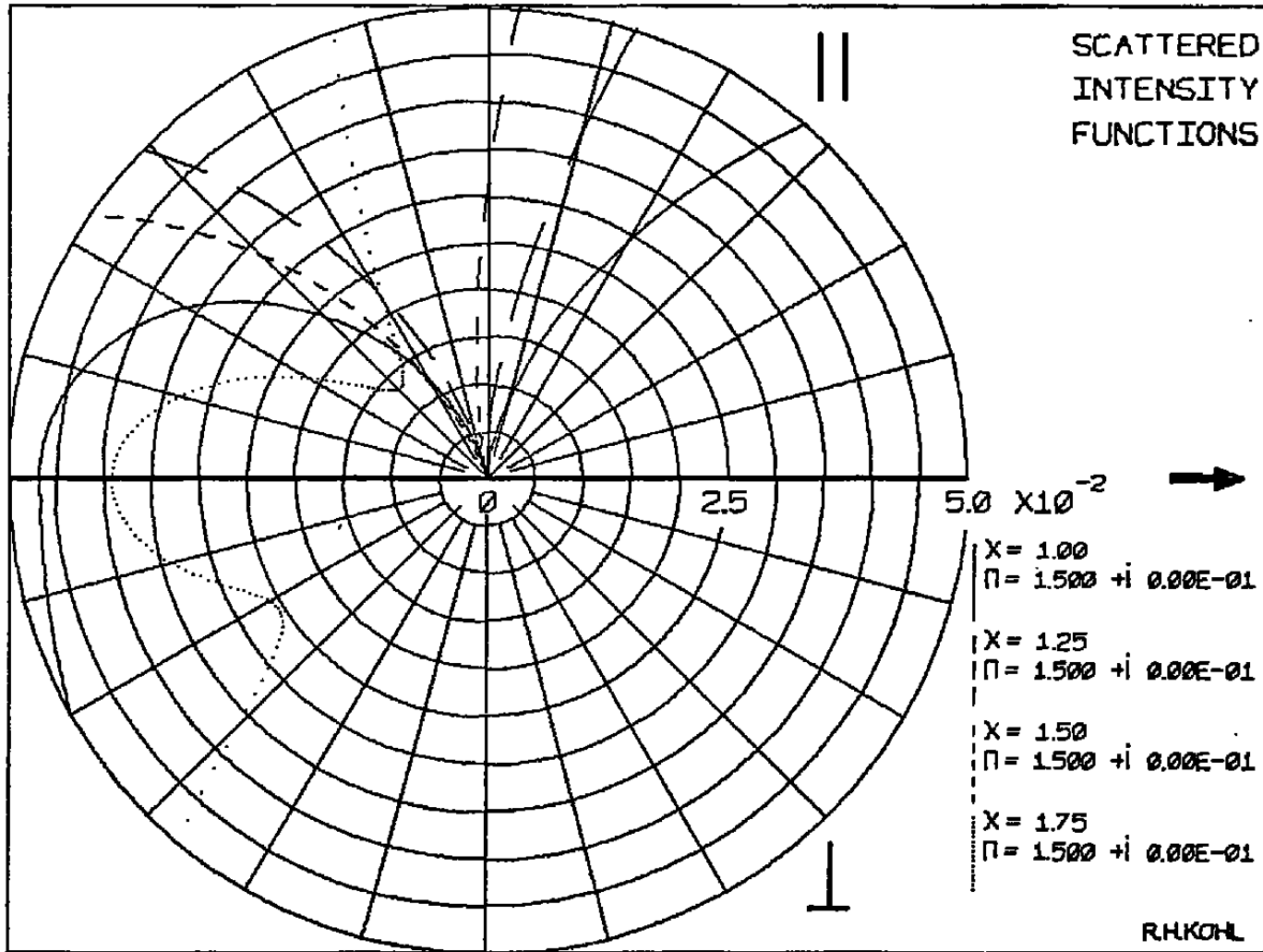


FIGURE 15

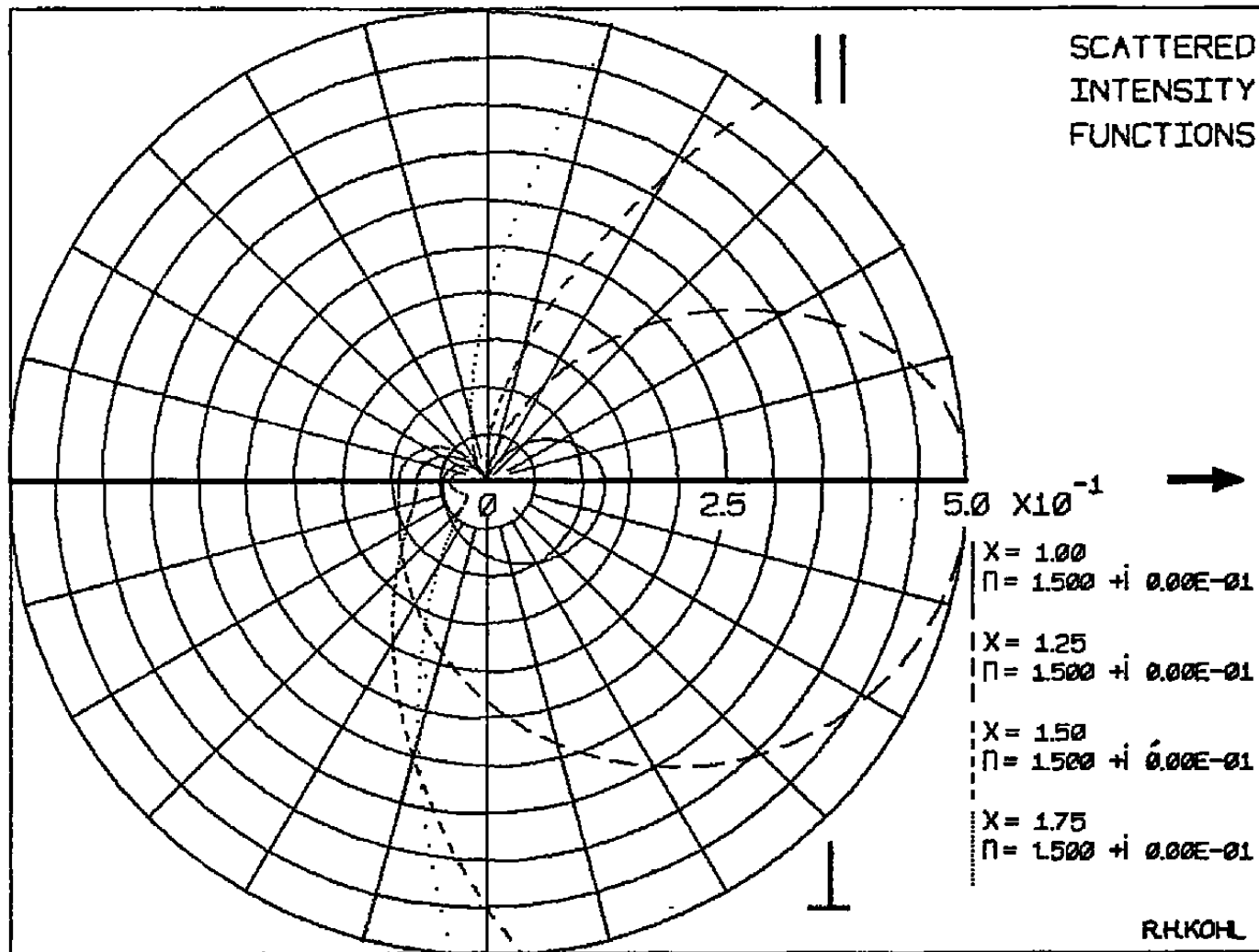


FIGURE 16

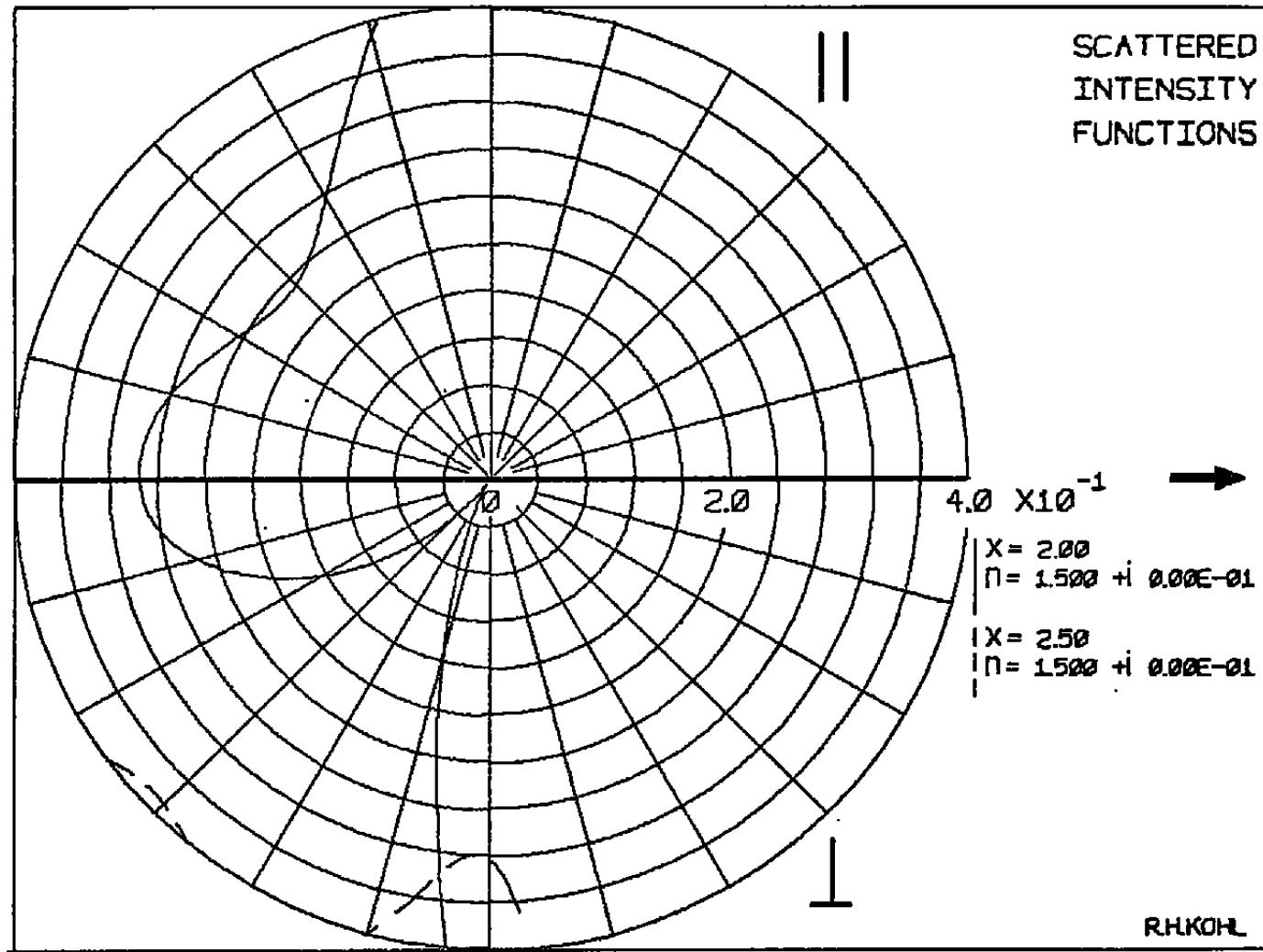


FIGURE 17

152

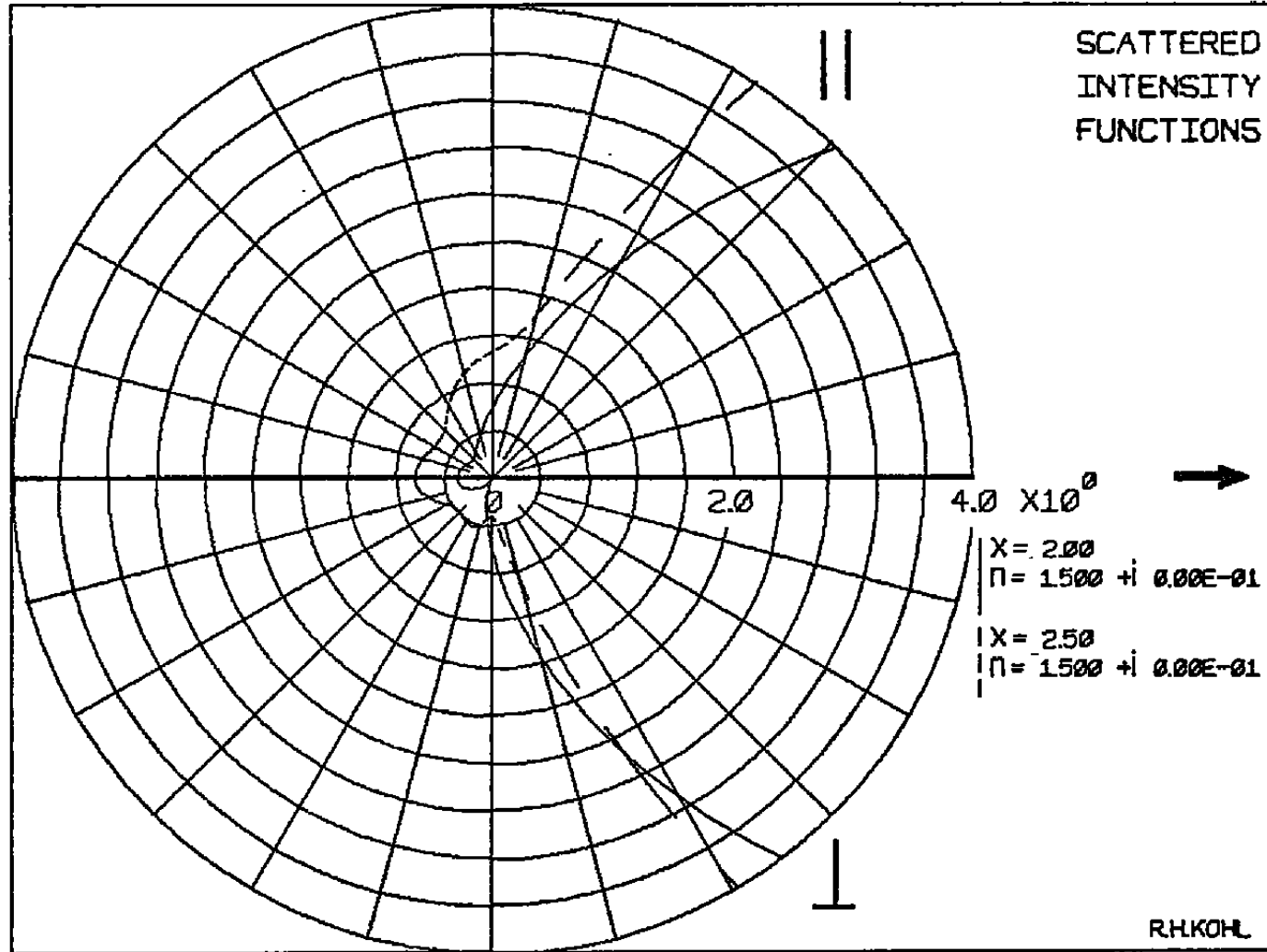


FIGURE 18

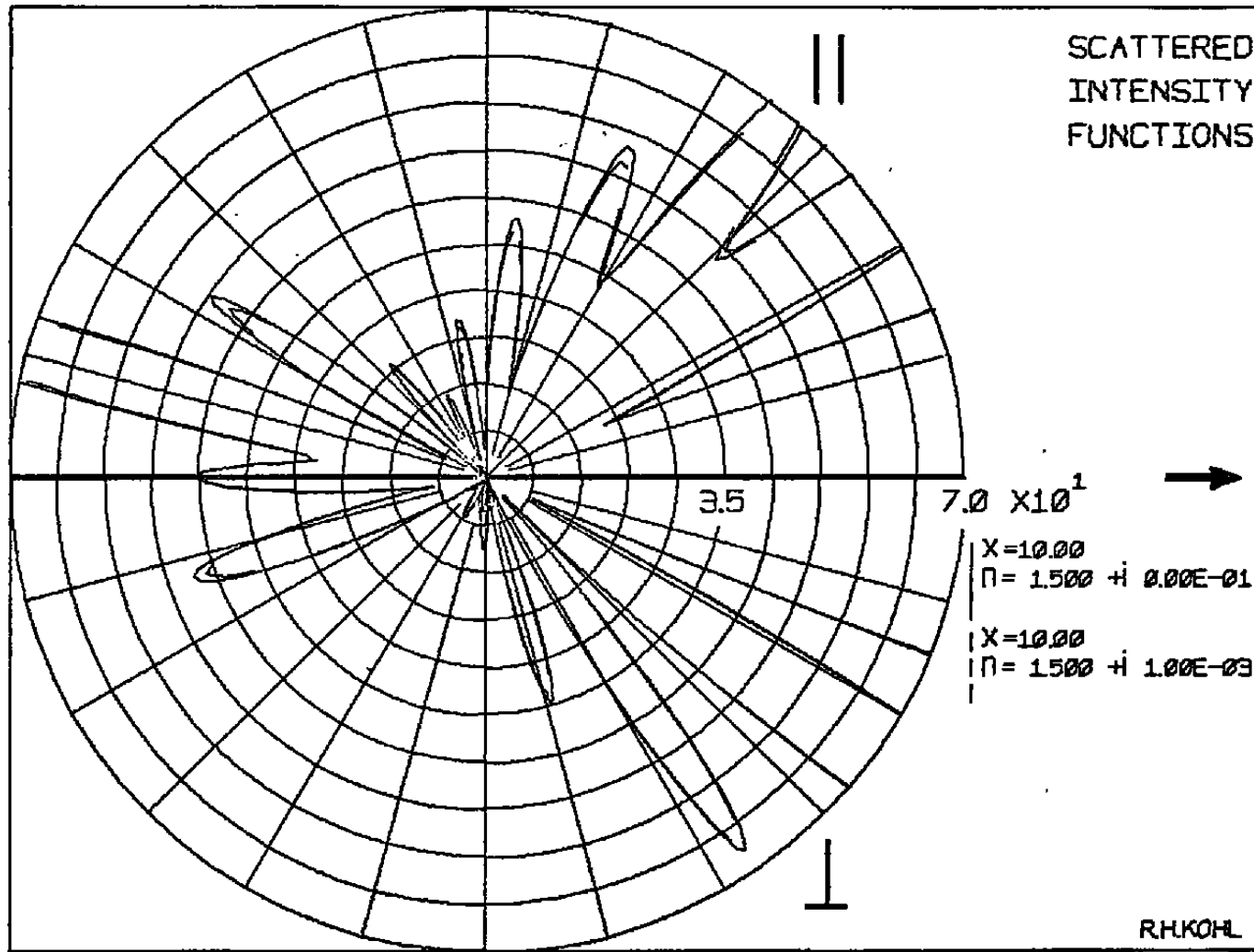


FIGURE 19

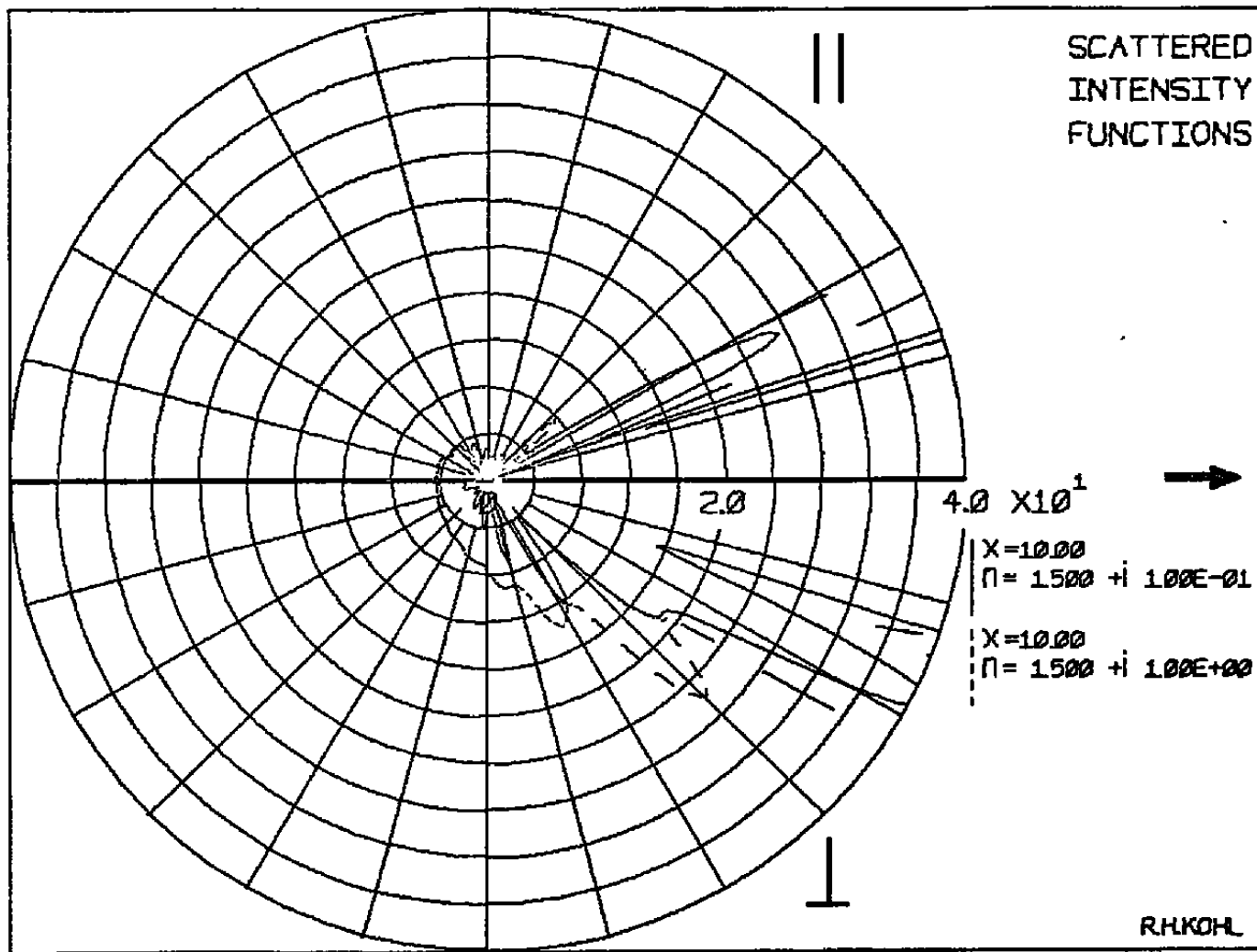


FIGURE 20

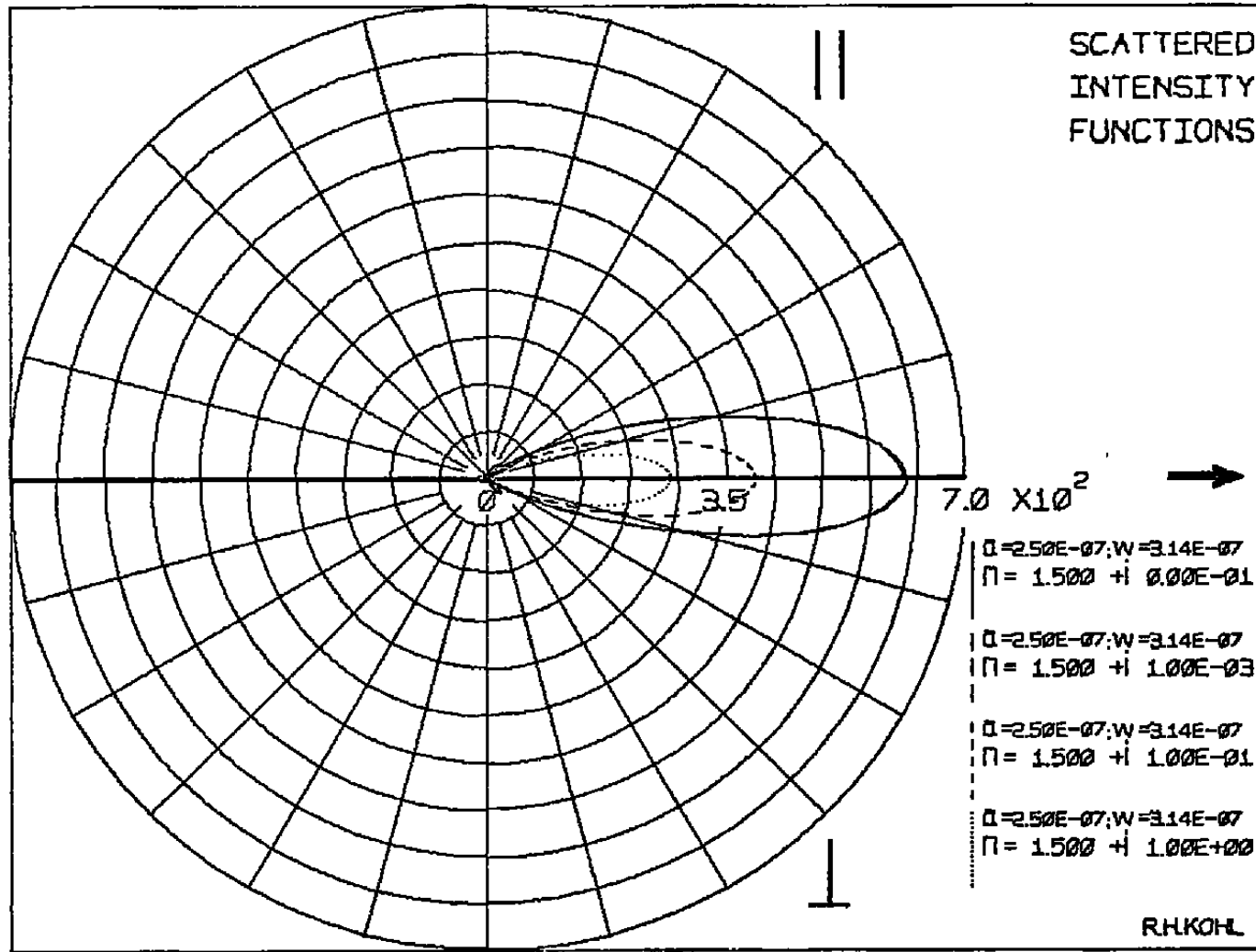


FIGURE 21

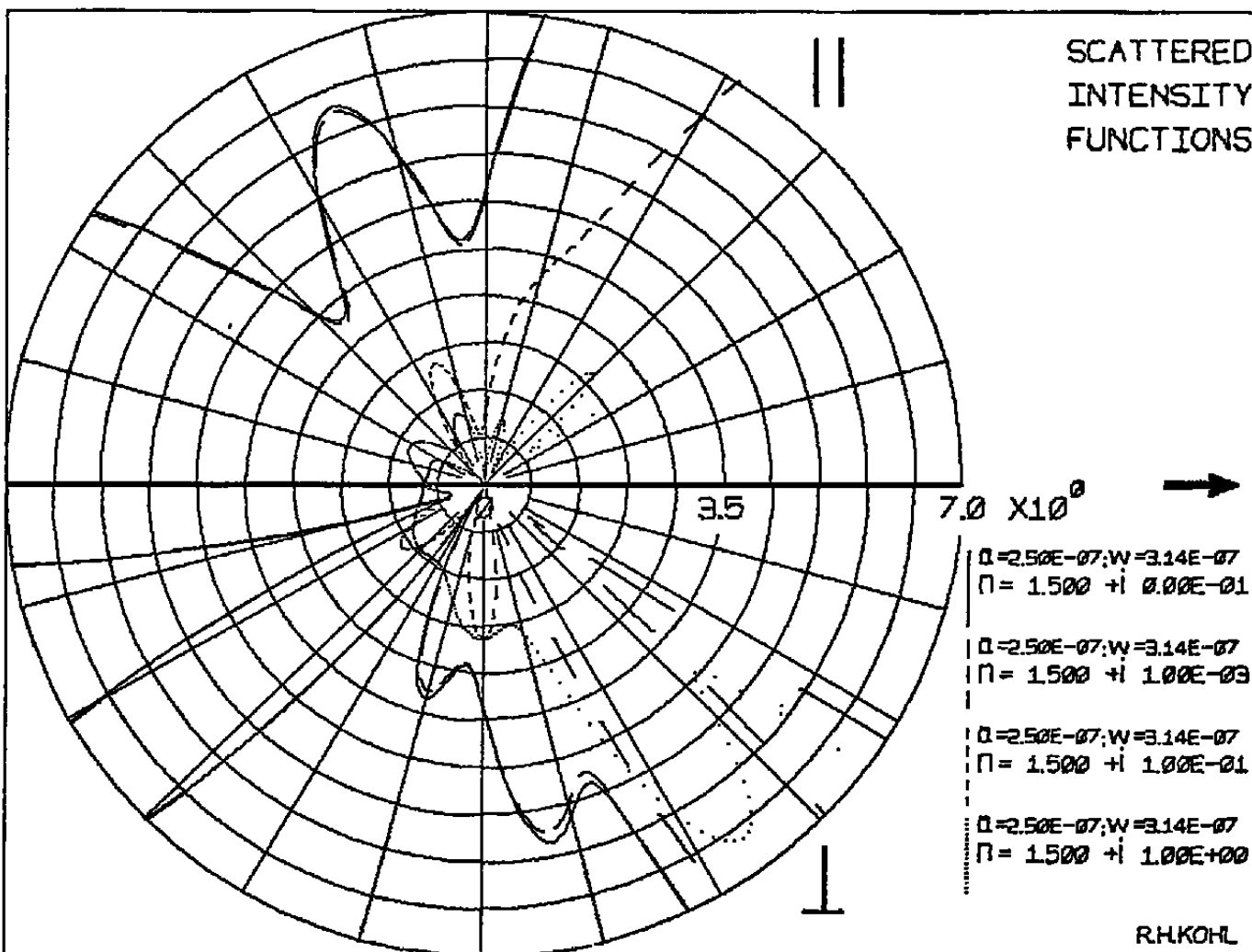


FIGURE 22